UNIVERSITY OF OKLAHOMA

GRADUATE COLLEGE

NANOSCALE STUDIES OF THERMAL TRANSPORT: R-MATRIX THEORY AND THERMAL TRANSPORT IN STRAINED GRAPHENE NANORIBBONS.

A DISSERTATION

SUBMITTED TO THE GRADUATE FACULTY

in partial fullfillment of the requirements for the

Degree of

DOCTOR OF PHILOSOPHY

By

K.G.S.H.GUNAWARDANA

Norman, Oklahoma

2011

NANOSCALE STUDIES OF THERMAL TRANSPORT: R-MATRIX THEORY AND THERMAL TRANSPORT IN STRAINED GRAPHENE NANORIBBONS.

A DISSERTATION APPROVED FOR THE HOMER L. DODGE DEPARTMENT OF PHYSICS AND ASTRONOMY

By

Kieran Mullen, Chair

Dimitrios Papavassiliou

Gregory A. Parker

Michael B. Santos

Alberto Striolo

To my loving parents.

Acknowledgements

First and foremost, I am grateful to my advisor Prof. Kieran Mullen. This thesis would not have been possible without his farsighted guidance and encouragement.

I would like to thank my thesis committee: Prof. Gregory Parker, Prof. Dimitrios Papavassiliou, Prof. Michael B. Santos, and Prof. Alberto Striolo for their insightful comments and encouragement. I owe my deepest gratitude to Prof. Yong P. Chen at Purdue University for giving me an opportunity to work in his research group. I would like to thank Prof. Xiulin Ruan at Purdue University for his useful comments and guidance on my research. I would also like to thank Jiuning Hu for his continuous support. It is also a pleasure to thank all my friends who supported me in various ways.

Most importantly, I thank my parents, Anula Siriwardana and K.G. Gunawardana for their courageous effort in directing me towards acadamics since my childhood. It is unforgettable the loving support that I always got from my wife, Kalani. Finally, I remember my loving son, Kavith, and daughter, Sathmi.

Table of Contents

List of Figures

Abstract

The rapid development of nanotechnology has enabled the fabrication of structures much smaller than the mean free path of electrons and phonons. In modern electronics, miniaturization is desired to increase the transistor density and the clock speed. Electronic transport on the nanoscale has been studied for over three decades and fascinating quantum effects have been observed. Phonon transport on this scale is of significant interest because of the increased power dissipation in nanoelectronics, which undermines the correct functionality of devices and limits their lifetime. Apart from the effort to minimize heat generation, an efficient heat management scheme is necessary.

Historically, thermal transport in bulk materials was described by the Fourier's law, in which the thermal conductivity is an intrinsic property of the material. Later a more descriptive model, the Boltzmann approach for thermal transport, was developed and could explain the thermal conductivity down to a 100 nm length scale at high temperatures. At low temperatures and in structures smaller than roughly 100 nm, thermal transport is described by the fully quantum mechanical Landauer-Butticker formalism. In this context, accurate calculation of phonon transmission probabilities is very important.

In this dissertation, I develop a continuum model to calculate phonon transmission probabilities between media, which have high contrast in the elastic properties. In this work, we include an interface transition layer between the two media and look for interface properties that improve thermal transport.

Secondly, I develop a new theoretical tool based on the R-Matrix theory to calculate phonon transmission probabilities on the atomic scale. R-matrix theory is a well developed theoretical approach commonly used in nuclear and atomic physics to solve scattering problems. Recently, this approach has been successfully developed to calculate electronic scattering in mesoscopic quantum devices. The key novelty of R-matrix theory for phonons is that the only required information about the scattering region is its normal modes, which are evaluated only once for a system. This approach is computationally efficient and produces the same results as the modern technique based on the non-equilibrium Green's function (NEGF) approach. I present a detailed theoretical explanation of this approach and results applying to graphene nanoribbons. This theoretical development is presented focusing on two terminals devices while the extension to the devices with multiple leads is straightforward.

Finally, I use molecular dynamics to study the thermal transport properties of strained graphene nanoribbons. I find that the thermal conductivity of zigzag graphene nanoribbons shows a weak dependence on moderate tensile strains, while that of armchair graphene nanoribbons decreases significantly. This is a promising feature in strain-induced device applications. Furthermore, we observe significant thermal rectification (over 70%) in a rectangular armchair graphene nanoribbon by applying a transverse force asymmetrically. The heat flux is larger from the less stressed region to the more stressed region. These findings can potentially enable real-time tuning of the thermal rectification by a mechanical force in nanostructures.

Chapter 1

Nanoscale Thermal Transport

In most electronic and optoelectronic devices, large amounts of energy is dissipated as heat. This is a waste and undermines the correct functionality of devices and limits their life time. Apart from the effort to minimize heat generation, an efficient heat management scheme is necessary. The incorporation of thermal interface materials (TIM), materials filling the gap between the device and the heat sink, is one major solution and the use of high thermal conductivity materials such as carbon nanotubes and graphene for TIM is one promising approach [1]. The fundamental problem on the nanoscale is poor thermal conductivity. At this scale thermal conductivity is completely dominated by boundary surface scattering, impurity scattering and the interface scattering [2, 3, 4, 5, 6]. This problem has gained huge attention in recent years for both thermal management and energy harvesting applications. The remarkable tunability of both electronic and thermal transport on the nanoscale is promising for nanoscale thermoelectric applications [7, 8, 9]. Moreover, nanoscale thermal device operation is an another important application. Thermal devices, such as thermal rectifiers [10], thermal transistors [11] and thermal memories [12] are a new class of devices, whose operation is driven by the temperature gradients. These devices will have useful applications not only in thermal circuits [13] but also in nanoscale thermal management and thermo-electric applications. Furthermore, highly thermal conducting nano particles can be disperse in polymer to improve the thermal conductivity

of polymers which also have vast range of applications [14, 15, 16]. In this context, understanding the thermal transport in length scales that is smaller than the mean free path of phonons (λ_F) in the bulk is of significant interest [17].

1.1 Thermal transport in bulk

Thermal conductivity(κ) is a measure of the ability to transfer thermal energy by conduction, the main mechanism of thermal transport in solids. This property of materials has been studied for a long time. French physicist Jean Baptiste Joseph Fourier first gave a mathematical formula to describe thermal transport which is now well known as Fourier's law [18]. Fourier's law states that the thermal flux($J(x)$) is proportional to the temperature gradient.

$$J(x) = \frac{\dot{Q}}{A} = -\kappa \frac{dT}{dx}, \tag{1.1}$$

where A is the cross-sectional area, $\dot{Q}$ is the thermal current, $\frac{dT}{dx}$ is the temperature gradient at "x" direction. The minus sign impose that the energy transfer is always from the warmer side to the colder side of a material. This has been successfully used in describing thermal transport on the macroscopic scale for almost two centuries. The thermal conductivity (κ) is considered to depend only on the material and is measured in units of W/mK. The κ of dielectric materials are mainly through the lattice, while that of metals are dominated by electrons. Poor thermal conductivity materials are known as thermal insulators. For example, the κ of polypropylene is about 0.25 W/mK [19]. Materials with excellent thermal conductivity are called

thermal conductors. Copper has a κ of 400 W/mK and that of diamond is in the range of $900 - 2320$ W/mK [20]. The recently discovered carbon based materials, carbon nanotubes (CNT) and graphene have extraordinarily high thermal conductivity. The κ of a single wall CNT is about 3500 W/mK [21, 22] and that of graphene is in the range of $4800 - 5300$ W/mK [23, 24].

The thermal conductivity due to the lattice is often described by phonons. Phonons are the collective oscillating displacement waves in the lattice. There are two types of phonons in crystals: acoustic phonons and optical phonons. In acoustic phonons adjacent atoms vibrate in phase and the oscillation frequency reaches zero as the wavelength goes to infinity. These phonons make a larger contribution to the lattice thermal conductivity since they have a larger group velocity. In optical phonons adjacent atoms vibrate out of phase and they have smaller group velocity. To describe the low temperature thermal behavior of lattice, the quantization of the phonon energies is very important. In the quantum perspective, the quantized energy(E_n) of a harmonic oscillator of angular frequency ω is given by,

$$E_n = \hbar\omega \left(\frac{1}{2} + n\right), \tag{1.2}$$

where n is an integer and $\hbar$ is the Planck constant. The energy quantization and Debye assumptions (i.e. linear phonon dispersion for acoustic phonons and a frequency cut off) could accurately predict the temperature dependence of the lattice heat capacity (C) of solids at low temperatures.

In a simple kinetic theory approach, where the solid is considered as a gas of

phonons, thermal conductivity can be expressed as,

$$\kappa = \frac{1}{3} C v_{ph} \lambda_l, \tag{1.3}$$

where v_{ph} is the phonon velocity and the λ_l is the mean free path of the phonons [25]. Phonons undergo continuous collisions with the crystal boundaries, lattice imperfections, impurities, and other phonons and electrons. These collisions limit the thermal conductivity. The mean free path is the average distance between two collision points. The different collision processes listed above would have different mean free paths and each would behave its own on the phonon frequency. The relative dominance of each scattering term is a characteristic property of a material and the temperature [26]. However, such a description of the phonon mean free paths is absent in the simple kinetic theory approach.

1.1.1 Boltzmann approach

A more detailed description of the thermal conductivity is in the semi-classical Boltzmann approach. Phonons are bosons. They follow the Bose-Einstein distribution:

$$\eta^o(k) = \frac{1}{\exp[\frac{\hbar\omega(k)}{k_B T}] - 1} \tag{1.4}$$

where, $\eta^o(k)$ is the equilibrium phonon distribution, ω is the angular frequency, k is the wave vector and k_B is the Boltzmann constant [27]. The phonon distribution ($\eta(k)$) is changed due to the continuous collisions stated above. The time evolution of the steady state phonon distribution ($\eta(k)$) can be expressed by the Boltzmann

equation[28].

$$\frac{\partial \eta(k)}{\partial t} \mid_{scatt.} = \vec{v}(k) \cdot \vec{\nabla} T \frac{\partial \eta(k)}{\partial T} \mid_{diffu.} \tag{1.5}$$

where, $\vec{v}(k)$ is the phonon group velocity, $\vec{r}$ is the coordinate and t is time.

In the relaxation time approximation the scattering rate is approximated by a constant relaxation time τ describing the exponential decay into the equilibrium distribution $\eta^o(k)$ as removing the temperature gradient)in the absence of a temperature gradient [26, 28]. In this approximation,

$$\frac{\partial \eta(k)}{\partial t} \mid_{scatt.} = \frac{(\eta(k) - \eta^o(k))}{\tau(k)} \tag{1.6}$$

and then the Boltzmann equation becomes,

$$\frac{(\eta(k) - \eta^o(k))}{\tau} = v(\vec{k}) \cdot \vec{\nabla} T \frac{\partial \eta(k)}{\partial T} \mid_{diffu.} \tag{1.7}$$

where $\tau(k)$ is the phonon relaxation time. Then the heat flux $\vec{J_Q}$ and the thermal conductivity κ_{ph} can be expressed as,

$$\vec{J_Q} = \sum_k \eta(k) \hbar \omega(k) v(k) \tag{1.8}$$

$$\kappa_{ph} = -\frac{\vec{J_Q}}{\nabla T} = \frac{1}{3} \sum_k \hbar \omega(k) v^2(k) \tau(k) \frac{\partial \eta(k)}{\partial T} \tag{1.9}$$

By replacing the summation with intergration and using the Debye assumptions, (a linear dispersion relationship $\omega = vk$ and a frequency cut off ω_D (Debye frequency)), the thermal conductivity κ_{ph} becomes [26]

$$\kappa_{ph} = \frac{k_B}{2\pi^2 v} \left(\frac{k_B}{\hbar} \right)^3 T^3 \int_0^{x_D} \tau(x) \frac{x^4 e^x}{(e^x - 1)^2} dx \tag{1.10}$$

where $x = \frac{\hbar\omega}{k_B T}$ and $x_D = \frac{\hbar\omega_D}{k_B T}$.

Here $\tau(k)$ should be the phonon relaxation time for resistive processes. The major resistive scattering processes in insulators are boundary surface scattering (B), 3-phonon Umklapp scattering (U) and impurity point defect scattering (P).

Phonon scattering by boundary surfaces is dominant in nanostructures at low temperatures. Diffusive scattering from rough surfaces limits the phonon mean free path. For perfect diffusive scattering the scattering rate can be given by $1/\tau_B = \vec{v}/L_c$ where L_C is called the Casimir length (Width of the sample). In contrast, polished surfaces show specular reflections in which the phonon mean free path is greater than the Casmir length. The specular phonon mean free path increases with decreasing temperature [29].

Phonon-phonon scattering has two forms: momentum conserving normal-processes and momentum nonconserving "Umklapp" processes [25]. Only the Umklapp processes directly contribute to the thermal resistance. In Umklapp scattering the phonon momentum is greatly suppressed by subtracting off a reciprocal lattice vector ($\vec{G}$), so it is categorized as a resistive process. At low temperatures Umklapp processes are negligible. As the temperature increases the average phonon energy increases, significantly increasing Umklapp scattering. At higher temperatures the Umklapp scattering rate is proportional to the temperature ($1/\tau_U \propto T$) and at lower temperatures it falls off as $\exp[-\theta_D/T]$ where θ_D is the Debye temperature [30].

The other important phonon scattering mechanism is impurity point defect scattering. In impure materials this is very important. When the dominant phonon

wavelength is larger than the size of the defect, impurity point defect scattering is a form of Rayleigh scattering. The scattering rate is $1/\tau_P = A\omega^4$, where A is the point defect concentration [4].

According to the Matthiessen's rule the total phonon relaxation rate τ^{-1} can be calculated as the sum of the individual rates [26, 4].

$$\frac{1}{\tau} = \frac{1}{\tau_B} + \frac{1}{\tau_U} + \frac{1}{\tau_P} \tag{1.11}$$

1.2 Thermal transport in nanostructures

In nanostructures, when the dominant phonon wavelength becomes less than the sample dimensions (at relatively high temperatures), phonon transport can be described by the three dimensional semiclassical Boltzmann approach described in the previous section. The Boltzmann approach has been used to study the thermal transport of GaAs nano wires of lateral dimensions greater than 100 nm [4]. However, study of thermal conductivity of silicon nano-wires of widths smaller than 100 nm has revealed that at low temperatures the variation of the thermal conductivity with temperature (T) deviates significantly from the Boltzmann approach, which gives a variation proportional to T^3 . In nano wires about 22 nm in width, a linear temperature dependence of the thermal conductivity has been observed [2]. This is a signature of the transport due to confined phonon modes, as I will show below.

1.2.1 Quantum thermal transport

The quantum regime is reached when the particle wavelength is larger than or of the order of the sample dimension. Electron transport in this regime has being studied for three decades [31, 32, 33, 34]. Electrons can be confined in two dimensional or one dimensional systems using potential barriers. In the case of phonons, engineering such a controllable trap is impractical. One feasible method is sandwiching the system between materials with a relatively high elastic constants, but choosing such a high contrast in elasticity is limited. Hence the best solution is to use freestanding or suspended nanostructures. When the dominant phonon wavelength is larger than or of the order of the two lateral dimensions of a dielectric nanowire, phonon transport is effectively one dimensional because motion in the lateral directions are suppressed due to quantum confinement. The energy of massless phonons (E) in a one dimensional channel can be expressed as,

$$E^2 = \hbar^2 v_s^2 \left(\vec{k_Z}^2 + \left(\frac{n\pi}{w}\right)^2 + \left(\frac{m\pi}{d}\right)^2 \right) \tag{1.12}$$

where,w and d are lateral dimensions, n and m are subband indices associated with w and d, $\vec{k_z}$ is the wave vector along the propagating direction, v_s is the velocity of sound and $\hbar$ is the Planck constant.

The existence of one dimensional phonon waveguide modes has been experimentally observed by J. Seyler et al. [35]. They used $Au_{0.60}Pd_{0.40}$ nano-wires grown on silicon substrates using e-beam lithography and room temperature thermal evaporation. The width (w) of the three sets of nano-wires were 90 nm, 50 nm and 30 nm and

the thickness (d) was approximately 20 nm. The change in the equilibrium resistance $(R - R_o)/R_o$ with the applied DC electric field was noted. Here R_o is the minimum resistance obtained by varying the temperature. All three sets of wires showed a minimum resistance at $T = 8K$. Applying an electric field heated the electrons and hence both the electron and phonon distributions deviated from equilibrium. Some distinct peaks of $\Delta R/R_o$ were observed with the electric field. These peaks were periodic with the electric field. The position of the peaks was independent of the temperature and the peaks broadened with increasing temperature.

The origin of these peaks can be explained using the phonon subband energies provided by the equation 1.12. Increasing the electric field increases the average electron energy. As the energy of the electrons approaches that of a phonon subband, the electrons can relax by dumping energy into the phonon subband, hence resistance peaks can be observed.

1.2.2 Electron transport

Transport in quantum regime can be well described using the Landauer formalism. In the end of 1950's Rolf Landauer developed this theory to describe the quantum limit of the electron transport [36].

According to the Landauer's approach, the net electrical current (I), of a one dimensional electron channel between two phonon reservoirs in the linear response regime can be written as follows,

$$I = \frac{2e}{h} \int_{E_L}^{E_R} \left(f^o(E, E_L^F) - f^o(E, E_R^F) \right) \zeta(E) dE \tag{1.13}$$

where $f^o(E, E_F)$ is the Fermi-Dirac distribution function given by equation(10), E_F^L and E_F^R are the Fermi energy of left and right reservoirs, and $\zeta(E)$ is the transmission probability of electron through the scattering center. Transport without scattering is called ballistic transport. This happens when the device length is smaller or equal to the electron mean free path. For ballistic transport of electrons we can set $\zeta(E) = 1$. At temperatures close to absolute zero, where the Fermi-Dirac function can be approximated by the step function and for small bias, the above equation can be simplified to give the electrical conductance G as

$$G = \frac{2e^2}{h} \zeta(E^F) \tag{1.14}$$

The factor $2e^2/h$ is well known as the quantum of electrical conductance. This was first observed by B.J. Van Wees et al. and D.A. Wharam et al. simultaneously in 1988 [33, 37].

1.2.3 Heat transport

Similarly, we can implement the same procedure for the energy current of phonons [38]. According to the Landauer formula the heat current between two phonon reservoirs at temperatures T_{Hot} and T_{Cold}, through a one dimensional phonon channel can be expressed as,

$$\dot{Q}_c = \sum_{\alpha} \int_{\omega_{min}}^{\omega_{max}} \frac{d\omega}{2\pi} \hbar \omega_\alpha(k) \left(\eta_{hot} - \eta_{cold} \right) \Gamma_\alpha(\omega), \tag{1.15}$$

where k is the phonon wave vector, k_B is the Boltzmann constant, $\omega_\alpha(k)$ and $v_\alpha(k)$ are phonon frequency and the velocity of the mode α, $\Gamma_\alpha(\omega)$ is the transmission probability of a phonon between the heat baths and $\hbar$ is Planck's constant. The functions η_{hot} and η_{cold} are the Bose-Einstein distribution function of heat baths at temperatures T_{hot} and T_{cold}.

At very low temperatures the contribution of higher energy phonons to the thermal conductivity is negligible. It is reasonable to assume that only the massless phonons ($\omega = vk$) dominate the transport, so we can set the lower limit of the above integration as 0. Taking the limit $\Delta T \to 0(\Delta T = T_{hot} - T_{cold})$ the thermal conductivity (κ_{ph}) of one dimensional channel between two reservoirs can be obtained. Here the ballistic limit of phonons is assumed ($\Gamma(\omega) \approx 1$). (A description of ballistic transport of phonons is given below)

$$\kappa_{ph} = \frac{k_B^2 \pi^2}{3h} T N_\alpha \tag{1.16}$$

where T is the temperature and N_α the number of polarization modes contributing to the conductance.

We can set $N_\alpha = 1$ for a one dimensional channel. The lowest possible thermal conductance in a one dimensional channel , $\frac{k_B^2 \pi^2}{3h} T$, is called the quantum of thermal conductance. This is independent of the material properties and the geometry. Further, unlike the quantum of electronic conductance this is proportional to the absolute temperature.

The unit transmission of phonons can be observed for nanostructures. Most nanostructures consist of defects, edge disorder, impurities and interfaces. These imperfec-

tions cause the transmission probabilities to deviate from unity. In this context, the exact calculation of phonon transmission probabilities between thermal reservoirs is the fundamental problem. There are many theoretical approaches to calculate phonon transmission probabilities such as continuum elasticity models, Green's function approaches and transfer matrix methods. A continuum model is efficient and well suited to study the long wave length behavior, which is sufficient to predict the thermal conductivity at low temperatures. In chapter 2 of this thesis, we develop a continuum model to incorporate the interface coupling between two dissimilar materials.

However, the continuum approach is not sufficient to predict the thermal conductivity at moderately high temperatures since the short wave length phonons and the optical modes are not represented accurately. Thus, it is essential to calculate the transmission probabilities including all the details of the atomic constituents of the system to get an accurate description of the full phonon spectrum. In this regard, the Non-equilibrium Green's function (NEGF) approach is one of the more widely used approaches.

The main focus of this thesis is to develop an alternative and computationally efficient approach in calculating the phonon transmission probabilities in the atomic scale. We adapt R-matrix theory to calculate phonon transmission across a device of molecular to mesoscopic scale. By this technique, we can study the mode to mode transmission of phonons, which provides a more descriptive picture of the scattering mechanisms. The key novelty of R-matrix theory for phonon is that the only required information about the scattering region is its normal modes, which are evaluated only

once for a system. Normal modes are the collective oscillations of the lattice, which are orthonormal and form a complete basis in a finite region. These are calculated by diagonalising the dynamical matrix in the harmonic approximation of the interaction potential. The harmonic approximation is well suited to study thermal transport in mesoscopic scale systems and low temperature transport, which is not accessible by classical molecular dynamic simulations. In the harmonic approximation, phonon-phonon interactions are not included. In general such scattering is present at any non-zero temperature, but at low temperatures they do not make a significant contribution to the thermal conductivity. In nanostructures the most dominant scatters are the boundary, interface and impurities. Such scattering processes can be well studied in the harmonic approximation. R-matrix theory is an efficient and simple way in calculating the phonon transmission through a nanoscale system. Chapters 3 and 4 are devoted to the basic theoretical development of this technique. Moreover, we give a discussion of the results comparing to the NEGF approach. In chapter 5, we apply R-matrix theory to graphene nanoribbons.

1.3 Molecular dynamics simulations

Molecular dynamics(MD) simulation is an another essential numerical method in nanoscale thermal transport. The ability to include the anharmonic interactions and the easy of implementation are the advantages of this technique. Moreover as the development of the computer power, MD simulations can be readily extend to study the physics of large scale complex systems, in which the analytical tools can not be

reached. Biological systems and nanocomposites are example for this.

The heart of the classical MD simulations is the Newton's second law. When an atom (i) is exerted a net force "F_i", the rate of changing the momentum (P_i) of that atom, can be expressed as,

$$\frac{d\vec{P}_i}{dt} = \vec{F}_i. \tag{1.17}$$

Above equation is solved numerically for velocity ($\dot{r}_i(t)$) and the coordinate $r_i(t)$ of each atom in the system. The time integration is done in discrete time steps δt, carefully chosen according to the order of accuracy in the integration algorithm and the simulation cost. That is too large time steps will results in inaccurate results while too small time steps would significantly increase the computational time. There are many algorithms developed for this purpose (For example, Verlet algorithm, velocity Verlet algorithm, leap frog algorithm, Runge-Kutta method and Predictor-corrector algorithm). The numerical integration is carried out until the system reaches equilibrium or the non-equilibrium steady state. Following the ergodic theory, the relevant physical quantities are calculated by taking the time average.

In studying the thermal conductivity, establishing a non-equilibrium steady state is important. This is achieved by maintaining the temperature of the atoms in selected regions (heat baths). At the steady state a constant heat flux is flowing through the system and the thermal conductivity can be calculated according to the Fourier's law (eq. 1.1).

In chapter 6 of this dissertation, we use non-equilibrium molecular dynamics simulations to study the thermal transport in strain graphene nanoribbons.

1.4 Conclusion

In this chapter, we discussed the important theoretical approaches used in nanoscale thermal transport. In bulk materials, thermal conductivity can be described by Fourier's law. In this scale thermal conductivity is size independent and depends only on the material's intrinsic properties. On length scales of 100 nm $\sim$ 1 μm, the Boltzmann approach can well describe the thermal transport. On this scale thermal conductivity strongly depends of the size of the system and the nature of the boundaries (edge roughness). When we go even smaller ($<$ 100 nm), where modern electronics is concerned, the Boltzmann approach loses its validity. In this scale the Landauer-Buttiker formalism can be used to describe the thermal conductivity. In this context, calculating the phonon transmission probability between thermal reservoirs is the fundamental problem. Moreover, molecular dynamics simulations are also important in nanoscale thermal transport.

Chapter 2

Thermal Transport in the Continuum Limit

Most of the content presented here appear in Proceedings of 41st ISTC - Wichita, KS, Oct 19-22, 2009, SAMPE Journal.

2.1 Introduction

In this chapter, I study the inter-facial thermal transport between two acoustically mismatched materials. The mismatch of the acoustic impedance ($E\rho$, where E is the elastic constant and the ρ is the mass density) poses a significant Kapitza resistance at the interface. The Kapitza thermal resistance is the resistance to the heat transport across the boundary of two dissimilar materials [39, 40]. The effect becomes very significant when the two materials have a huge difference in elasticity so that there is only a weak coupling of phonon modes at the interface [41, 42]. We consider an interface that has high contrast in the elasticity such that the ratios of elasticities $E_1/E_0 = 1000$ and densities $\rho_1/\rho_0 = 2$. Such a contrast is present at the interface between carbon nanotubes (CNT) and polymers. The elastic modulus of a CNT is about 1 TPa whereas that of polymer is of the order of 1 GPa [43, 44]. Therefore the interface of CNTs and polymer pose a considerable Kapitza thermal resistance. We incorporate an interface transition layer which has the variable elasticity ($E(x)$) and density ($\rho(x)$) for which we are trying to obtain an optimal variation to maximize the inter-facial thermal transport. These interface transition layer could be analogous

to an attached hydrocarbon chain to CNTs. Such a chemical fuctionalization could improve the thermal transport of CNT-polymer composites. Clancy and Gates have reported a significant reduction of the Kapitza thermal resistance of CNT-polymer composites by grafting hydrocarbon chains to the surface of the CNT with covalent bonds [45]. Their work is based on the molecular dynamics simulations. Moreover they observed further reduction of the Kapitza thermal resistance with increasing length of the hydrocarbon chains and the grafting density. Kosevish has shown theoretically the existence of low frequency resonant vibrational modes at the interface transition layer between soft and rigid materials [46]. These resonant vibrational modes can reduce the Kapitza thermal resistance at elevated temperatures. The above approaches have difficulties in optimizing the properties of the interface transition layer or the grafted atomic chains to obtain the maximum heat flux through the interface due to the mathematical complexity and the computational cost of the molecular dynamics simulations. Our goal is to engineer the interface transition layer to maximize the heat transfer through the interface between hard and soft materials such as CNTs and polymers through a model calculation.

In section 2 below we describe the our model system used for the optimization process and in section 3 we describe the numerical and analytical approaches of optimizing the interface and the results. There, we consider the propagation of longitudinal vibrational waves in one dimensional inhomogeneous constriction. These inhomogeneities are the variation of the mass density and the elasticity from soft to hard materials.

2.2 The model

Our model consists of a one dimensional chain of atoms (a channel) strongly bonded to each other, where the force constants are equivalent to that of carbon nanotubes. This atomic chain is connected to two heat baths at temperatures T_{hot} and T_{cold} at either end. These heat baths replicate very soft media like polymers and have comparably small force constants. The ratio of force constants between the heat bath and the channel is kept at $1 : 1000$. The coupling of the heat bath to the channel is always through an atomic chain whose atomic mass and force constants are varying with position.

We adopt the Landauer-Buttiker formalism to describe the thermal flux through the channel, $\dot{Q}_c$. In this approach the ballistic transport of phonons between two phonon reservoirs is given by the Landauer formula (eq. 1.15). In our model we assume the channel is a perfect phonon conductor. This approximation is reasonable for CNTs even at higher temperatures. It has been theoretically predicted that the ballistic length of CNT can be larger than 100 nm at room temperature. However our goal is to optimize the interface hence the interaction within the channel is irrelevant.

To estimate the transmission probability we use a continuum approximation in which the model system is considered as a one dimensional rod of continuous material. This approximation has been widely used in determining the transmission probability of low frequency acoustic phonons [38, 47, 48, 49]. This approximation holds when the dominant phonon wavelength is larger than the lattice spacing [50].

We are interested in the transmission probability of phonons into the channel

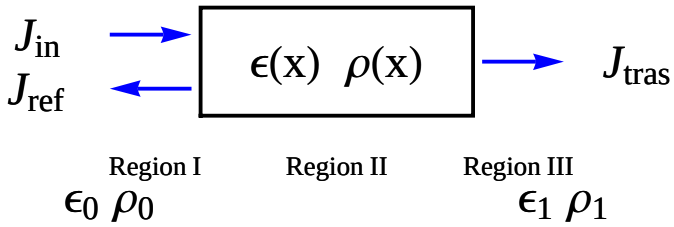

Figure 2.1: Three regions of interest: Region I is the heat bath, Region II is the inhomogenious interface and the Region III is the uniform channel.

from the heat bath. Figure 2.1 depicts the three regions of interest. Region I is the uniform heat bath, region II is the inhomogeneous interface and region III is the uniform channel.

2.3 Phonon transmission in the continuum limit

The method of deriving the transmission probability from one heat bath into the channel is described below and by extending the similar procedure we can calculate the transmission probability from one heat bath to another. The elastic modulus and the mass density of the heat baths and the channel are denoted by Y_p, D_p and Y_c, D_c. The interface region has a position dependent mass density $D(z)$ and elastic modulus $Y(z)$. Before proceeding, we switch to dimensionless quantities. The elastic modulus and the density are expressed in terms of the those channel, and the length

is scaled by the length of the interface region (L). That is $x = z/L$, $\epsilon(x) = Y(x)/Y_c$, $\rho(x) = D(x)/D_c$, $\epsilon_0 = Y_p/Y_c$ and $\rho_0 = D_p/D_c$. In this problem we enforced $\epsilon_0 = 0.001$ and $\rho_0 = 0.5$. At the channel we have $\epsilon_1 = 1$ and $\rho_1 = 1$. The atomic displacement in these three regions are given by $U_I(R)$, $U_{II}(R)$ and $U_{III}(R)$, where R refers to the atomic discrete atomic positions. In the long wavelength limit where the individual atomic displacements vary slowly through the neighbouring atoms, we can define continuous displacement fields such as $U_I(x,t)$, $U_{II}(x,t)$ and $U_{III}(x,t)$, where "x" is the continuous variable and "t" is the time. In this continuum limit, the dynamics of the displacement waves are governed by the scalar wave equation [51].

$$\frac{\partial}{\partial x}\left(\epsilon(x)\frac{\partial U(x,t)}{\partial c}\right) = \rho(x)\frac{\partial^2 U(x,t)}{\partial t^2}, \tag{2.1}$$

which can be written as follows in the uniform medium,

$$\frac{\partial^2 U(x,t)}{\partial t^2} = c^2\frac{\partial^2 U(x,t)}{\partial x^2}, \tag{2.2}$$

where the "c" is the speed of sound, $c = \sqrt{\epsilon/\rho}$. The solutions to the scalar wave equation in the uniform regions (eq. 2.2) take the usual harmonic form given by,

$$U_I(x,t) = A\exp[i(k_0x - \omega t)] + B\exp[-i(k_0x + \omega t)], \tag{2.3}$$

$$U_{III}(x,t) = C\exp[i(k_1x - \omega t)], \tag{2.4}$$

where k_0 and k_1 are wavevectors of the vibrational waves in the heat bath and the channel, given by $k_j = \omega\sqrt{\rho_j/\epsilon_j}$. In region II, we must solve the differential equation 2.1. It is impossible to find an exact solution to the equation 2.1 for arbitrary functions of $\epsilon(x)$ and $\rho(x)$.

First, we do a numerical solution to region II. For a given functions $\epsilon(x)$ and $\rho(x)$, we can find two linearly independent numerical solutions (U^a_{II} and U^b_{II}) to equation 2.1 by choosing solutions to different boundary conditions. Specially, for U^a_{II} we choose $U_{II}(0) = 0$ and $U'_{II}(0) = 1$ and for U^b_{II} we choose $U_{II}(0) = 1$ and $U'_{II}(0) = 0$. Then we can write a general solution in the region II as follows,

$$U_{II}(x,t) = C^a U^a_{II}(x,t) + C^b U^b_{II}(x,t). \tag{2.5}$$

We then impose continuity on the displacements U_I, U_{II} and U_{III} and their derivatives at the boundaries. The boundaries are at $x = 0$ and $x = 1.0$. This process yields 4 equations as follows,

$$\begin{aligned} A + B &= C^a U^a_{II}(0) + C^b U^b_{II}(0) \\ C^a U^a_{II}(1.0) + C^b U^b_{II}(1.0) &= C\exp[ik_1] \\ ik_0 A - ik_0 B &= C^a U'_{II}(0)^a + C^b U'_{II}(0)^b \\ C^a U'_{II}(1.0)^a + C^b U'_{II}(1.0)^b &= ik_1 C\exp[ik_1]. \end{aligned} \tag{2.6}$$

The above set of equations can be solved for the transmission coefficient (τ), $\tau = C/A$.

2.4 Thermal energy flux and transmission probability,

The transmission probability of a phonon can be calculated by considering the energy fluxes associated with the displacement waves. The total mechanical energy density $\xi(x,t)$ of the displacement wave $U(x,t)$ can be expressed as the sum of the kinetic and potential energy densities.

$$\xi(x,t)_j = \frac{1}{2}\rho_j \left(\frac{\partial U(x,t)}{\partial t}\right)^2 + \frac{1}{2}\epsilon_j \left(\frac{\partial U(x,t)}{\partial x}\right)^2, \tag{2.7}$$

where "j" refers to the heat bath ($j = 0$) or the channel ($j = 1$). The continuity equation,

$$\frac{\partial \xi(x,t)}{\partial t} + \nabla \cdot \vec{J}(x) = 0, \tag{2.8}$$

enables us to solve for the energy flux ($J(x)$). There is another equation we can derive from the wave equation 2.2. The general form of the solutions to the wave equation take the following form $f(x-ct)$ and $g(x+ct)$. Using the above form of solutions for $U(x,t)$, we can show the following relation.

$$\frac{\partial U}{\partial x} = \frac{-1}{c}\frac{\partial U}{\partial t}. \tag{2.9}$$

For the solutions of the form $U(x,t) = U(x)e^{i\omega t}$ and using the equations 2.7, 2.8 and 2.9, the energy flux carried by the displacement wave through the medium can be derived.

$$J_j(x) = i\omega c_j^2 \rho_j \left(U^*(x)\nabla U(x) - U(x)\nabla U^*(x)\right). \tag{2.10}$$

It can be shown that the incoming energy flux in the heat bath takes the following form,

$$J_{in} = 2\omega c_0^2 \rho_0 k_0 A A^*, \tag{2.11}$$

and the transmitted energy to the channel is

$$J_{trans} = 2\omega c_1^2 \rho_1 k_1 C C^*. \tag{2.12}$$

The transmission probability of a phonon of frequency ω from heat bath to the channel is,

$$\Gamma(\epsilon(x), \rho(x), \omega) = \frac{J_{trans}}{J_{in}} = \frac{c_1^2 \rho_1 k_1}{c_0^2 \rho_0 k_0} \tau \tau^*, \tag{2.13}$$

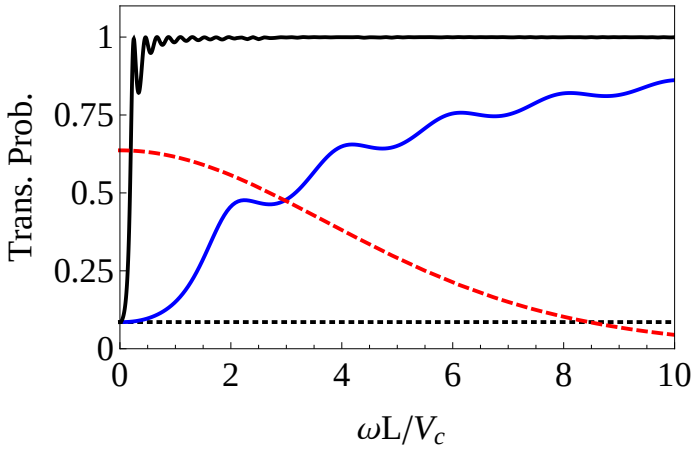

Figure 2.2: Transmission probability of phonon into the channel from the heat bath vs. scaled frequency. The black dotted line is the transmission probability for an abrupt change of elasticity and mass density neglecting the interface coupling. The thick blue line is for a linear interpolation of $\epsilon(x)$ and $\rho(x)$. The thick black line shows the transmission probability of the optimal variation of $\epsilon(x)$ and $\rho(x)$. The dashed red line is the thermal weight to the transmission probability which contributes to the Landauer energy flux at $T = 300$ K and V_c is the speed of sound in the channel.

where $*$ refers to the complex conjugate. The transmission probability Γ depends on the properties of the interface transition region. Thus, it is written as a function of $\epsilon(x)$ and $\rho(x)$.

2.5 Numerical optimization

The optimization was started from a linear interpolation of $\epsilon(x)$ and $\rho(x)$. After calculating the heat flux, the functions $\epsilon(x)$ and $\rho(x)$ were randomly varied subject to the constraints that they take on the correct values at the boundaries and that

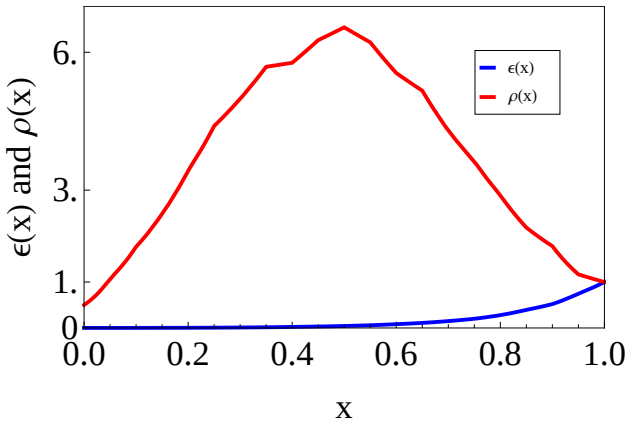

Figure 2.3: Optimal $\epsilon(x)$ and $\rho(x)$ obtained numerically, giving the maximal thermal conductivity.

they are positive. Variations that increased the heat flux were accepted. The process was iterated and the size of the variations decreased until $\epsilon(x)$ and $\rho(x)$ converged. Figure 2.2 shows the transmission probability of phonons into the channel from a heat bath against the scaled frequency. The red dashed line is the thermal weight to the transmission probability which contributed to the Landauer energy flux. This is plotted at $T = 300$ K when $\Delta T \ll T$. The black dotted line shows the transmission probability for an abrupt change of elasticity and mass density without considering the coupling at the interface and the blue line is for a linear interpolation of $\epsilon(x)$, $\epsilon(x) = (1 - \epsilon_0)x + \epsilon_0$ and $\rho(x)$, $\rho(x) = (1 - \rho_0)x + \rho_0$. The black line shows the transmission probability of the optimal variation of $\epsilon(x)$ and $\rho(x)$, which is shown in Fig. 2.3. According to the Fig. 2.2 by increasing the length of the interface (L), over which $\epsilon(x)$ and $\rho(x)$ are varied the transmission function can be squeezed towards low frequencies hence the thermal flux due to low frequencies is increased. The optimal

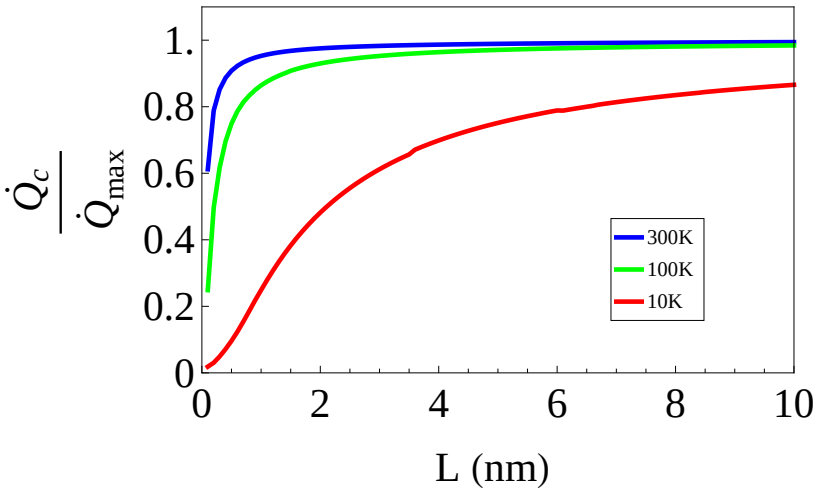

Figure 2.4: Normalized energy flux through the channel vs. length of the interface at $T = 10$ K, 100 K and 300 K. The channel has an optimized interface at either end connecting it to heat baths at different temperatures.

mass density variation peaks at approximately six times that of the channel density (ρ_1) in the middle region of the interface and the elasticity variation is slowly varying on the side of the soft heat bath and has a rapid rise near the channel. This kind of elasticity variation seems physically achievable. There can be a few atomic layers of intermediate force constants decaying rapidly at the interface of hard and soft material. At room temperature (300 K), the abrupt change of the material without considering the interface coupling gives only 10% of the maximum heat flux into the channel. With the linear interpolation of the interface transition layer, we could get about 47% of the maximum heat flux into the channel having about a 1 nm long interface region (L). For the optimal variation 97% of the maximum flux into the channel can be obtained.

It is easy to extend the above techniques to calculate the transmission probability from a soft medium, through one interface, into a stiff channel and then through a second, identical interface and out the other side. Fig. 2.4 shows the variation of energy flux through such a system as a function of the length of the interface region (L) at temperatures 10K, 100K and 300K. In this calculation the energy flux is normalized to the maximum possible energy flux of a phonon mode. As mentioned before by increasing the length of the interface (L), over which $\epsilon(x)$ and $\rho(x)$ are varied the transmission function can be squeezed towards low frequencies hence the thermal flux into the channel is increased.

2.6 Analytical approximations

At discontinuities of material properties, the ratio of the reflected(σ_r) and incident(σ_i) stress pulses of longitudinal waves can be expressed as follows [51],

$$\frac{\sigma_r}{\sigma_i} = \frac{\epsilon_1\rho_1 - \epsilon_0\rho_0}{\left(\sqrt{\epsilon_1\rho_1} + \sqrt{\epsilon_0\rho_0}\right)^2}. \tag{2.14}$$

Reflectionless transmission can be achieved whenever the numerator of the above equation is zero. That is when $\epsilon_1\rho_1 - \epsilon_0\rho_0 = 0$. By extending the same argument to a rod whose properties are varying continuously, the condition for reflectionless transmission can be expressed as $\frac{d(\epsilon(x)\rho(x))}{dx} \approx 0$. This is not always possible when there are given properties at either ends. Figure 2.5. shows the product of $\epsilon(x)$ and $\rho(x)$ against the position for the optimal case. The variation has small derivatives, in agreement with the above condition. The next question raised is whether this

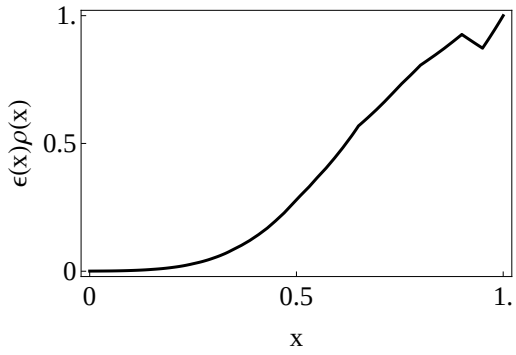

Figure 2.5: Product of $\epsilon(x)$ and $\rho(x)$ as a function of position.

optimal variation is unique. We believe that this variation is unique and a reasonable qualitative explanation can be obtained by looking at WKB approximate solution to the equation 2.1. The WKB solution to equation 2.1 can be written as follows,

$$U_{II}(x) = (\epsilon(x)\rho(x))^{-1/4} \exp\left[i\omega \int_0^x \sqrt{\frac{\rho(s)}{\epsilon(s)}} ds\right]. \tag{2.15}$$

The approximation holds when $\frac{d(\epsilon(x)\rho(x))^{-1/4}}{dy} \ll 1$, where $y = \int \epsilon(x)^{-1} dx$ and for $\omega L/c \gg 1$ [52, 53]. The transmission probability can then be calculated as described earlier. The transmission probability obtained numerically and the WKB method well matches beyond the first resonance peak (Fig.2.6).

Further understanding of the optimal variation can be obtained analyzing the low frequency ($\omega \ll 1$) behaviour of the transmission probability. The low frequency solution to the eq.2.1 can be obtained using the perturbation series method [54]. Here we assume solutions of the form,

$$U_{II}(x) = \sum_0^\infty f_n(x)\omega^{2n}. \tag{2.16}$$

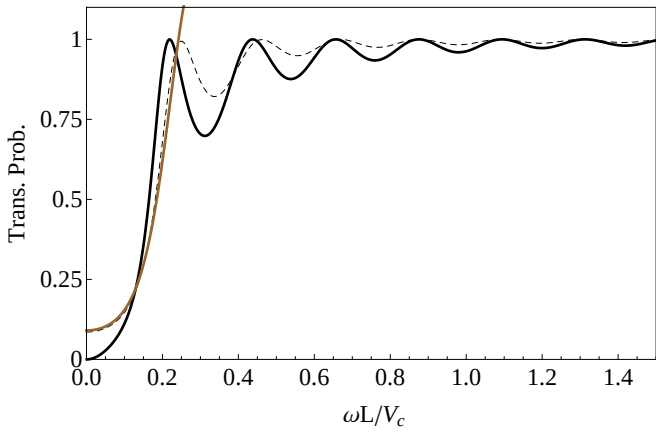

Figure 2.6: Transmission probability of phonons into the channel vs. scaled frequency for optimal $\epsilon(x)$ and $\rho(x)$. The dashed line is from the numerical method. The thick black line is from the WKB approximation and the brown line is from the perturbation series method.

Then we plugged the above solution to the equation 2.1 and obtained the expression,

$$\epsilon'(x)\sum_0 f_n'(x)\omega^{2n} + \epsilon(x)\sum_0 f_n''(x)\omega^{2n} = -\rho(x)\sum_0 f_n(x)\omega^{2(n+1)}. \tag{2.17}$$

The functions $f_n(x)$ are determined by matching ω by order and with the boundary conditions explained below. Basically we are looking for two linearly independent solutions: U_{II}^a and U_{II}^b. These two solutions are established by the boundary conditions $U_{II}^a(0) = 1$, $U_{II}^a(1) = 0$ and $U_{II}^b(0) = 0$, $U_{II}^b(1) = 1$. Since the zeroth order term of equation 2.16 gives the largest contribution, the boundary conditions are fully imposed on $f_0(x)$ and all $f_n(0)$ and $f_n(1)$ for $n \geq 1$ are set to zero. The displacement $U_{II}(x)$ was calculated up to the fourth order of ω and the transmission probability was calculated as previously by replacing the numerical solutions with the perturbation series solution. The solid brown line in the Fig.2.6 shows the transmission probability

obtained by this method.

2.7 Atomic model verification

The continuum approximation used in the above optimization is valid only in the low frequency regime, where the phonon dispersion can be given by the linear relation as $V_c = \frac{\omega}{k}$. When the wavelengths are close to the atomic spacing the continuum model fails as the discrete nature of the lattice become important. In the discrete lattice model, the phonon spectrum is finite because the wavelengths smaller than the lattice spacing does not exist. In the continuum model this higher frequency cut off is absent. Thus, it is useful to study how the optimal $\epsilon(x)$ and $\rho(x)$ shown in Fig. 2.3 behave in the discrete lattice model.

We use the R-matrix theory which is described in next chapters in details to do this comparison. We calculate the phonon transmission between soft heat baths ($\epsilon_0 = 0.001$ and $\rho_0 = 0.5$) through the rigid channel ($\epsilon_1 = 1.0$ and $\rho_1 = 1.0$). The interface between the soft heat baths and the channel is mediated by an interface coupling region whose force constant and mass variation are given by the optimal $\epsilon(x)$ and $\rho(x)$. Fig. 2.7 shows the transmission probability calculated from the R-matrix approach. There are 40 atoms in the channel. The green dashed line is without the interface coupling region. The soft atomic chain and the channel is connected by a single spring of force constant 0.1. The black solid line is for only the optimal force constant variation, which is taken as $\epsilon(x)$. The blue line is for the optimal $\epsilon(x)$ and $\rho(x)$ shown in the Fig. 2.3 when the interface consists of 10 atoms. The red

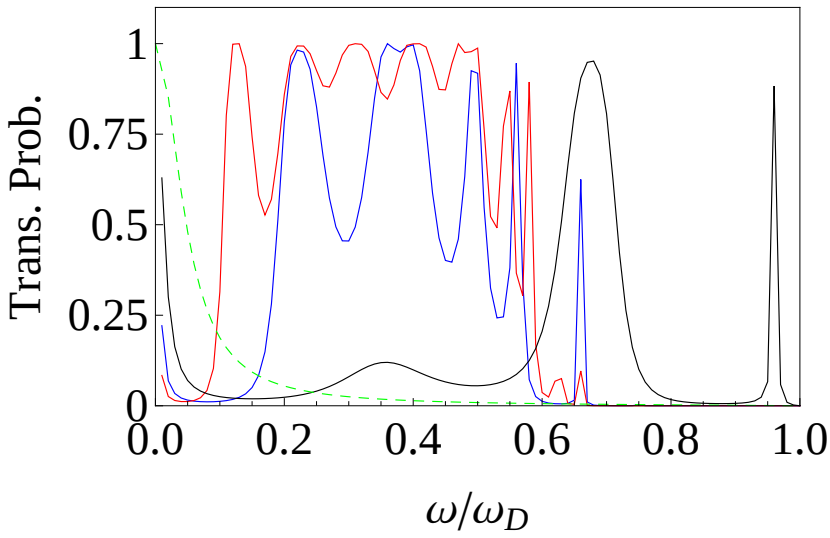

Figure 2.7: Transmission probability between two soft heat baths through a regid channel. The green dashed line is without the interface coupling region. The soft atomic chain and the channel is connected by a single spring of force constant 0.1. The black solid line is for only the optimal force constant variation, which is taken as the $\epsilon(x)$. The blue line is for the optimal $\epsilon(x)$ and $\rho(x)$ shown in the Fig. 2.3 when the interface consists of 10 atoms. The red line is for the case where the number of atoms in the interface is 20.

line is for the case where the number of atoms in the interface is 20. We observe significant improvement of the transmission probability over the 60% of the phonon spectrum of the soft material. Moreover the transmission function could move to the low frequencies as implied by the continuum approximation scaling. Thus, this optimal variation is better than having a single coupling spring connecting the hard and soft materials.

2.8 Conclusion

In this chapter, we discuss an approach to include the interface coupling in the continuum model, where we incorporate continuous functions to handle the interface. We use this approach to optimize the interface thermal transport between hard and soft materials. We include an interface variation of material to maximize the thermal transport and the optimal variation of mass density and elasticity is obtained numerically in the continuum limit. We also compare optimal variation with a discrete model. we observe remarkable improvement of the transmission probability over a 60% of the phonon spectrum in the low frequency region.

Chapter 3

R-Matrix Theory for Phonons

Some of the content presented here appear in Numerical Heat Transfer, Part B: Fundamentals 60(4), 2011.

3.1 Introduction

In this chapter, we develop a theoretical tool to calculate phonon scattering across a device of molecular to mesoscopic scale. It is possible to adapt the theories that were initially used to calculate electronic transmission probabilities to phonons. The recent use of Green's function approach is a good example for such a transition. We adopt R-matrix theory (RMT) to calculate phonon scattering in the ballistic regime.

RMT was first developed in studying resonances in nuclear reactions by Wigner and Eisenbud in 1947 [55]. The computational simplicity and the efficiency of this technique lead to its use in various disciplines of physics to study scattering problems. In 1971, RMT was applied to electron-atom scattering in atomic and molecular physics [56, 57]. Recently, RMT has been used in calculating electron scattering through quantum systems [58, 59, 60, 61]. We first review the application of RMT in electron scattering.

Electron scattering

In the framework of the Landauer-Büttiker formalism [36, 62], the conventional device model is a central scattering region connecting to two or more leads which take the carriers in and out of the scattering region. In RMT, a set of soft boundaries are defined to separate the scattering region (usually called the *interior region*) from the leads. The dynamics of electrons in this system are obtained by solving the Schrödinger equation. The key of the RMT is to solve the Schrödinger equation independently in the leads and the interior region. We then use the R-matrix($\mathcal{R}$) to solve for the scattering matrix ($\mathcal{S}$).

The leads are assumed to be perfect conductors so there is no scattering in the leads. They are also assumed to be nanowires so that the transverse motion of the electron is quantized. Thus the lead eigenfuctions can be given by plane waves traveling the length direction of the leads, $w(n_y, n_z; y, z) \exp[iq_x x]$, where the laterally quantized electron subbands can be given by $w(n_y, n_z; y, z) = \sin(n_y \pi y / w_y) \sin(n_z \pi z / w_z)$, n_y and n_z are quantum numbers on transverse direction, and y and z are orthogonal coordinates in the confined directions. These plane waves are used to expand a scattering solution in the leads.

The scattering potentials (electric and magnetic) are restricted to the interior region and the Schrödinger equation is solved to obtain a complete set of eigenvectors. However, the kinetic energy operator usually generates a non-Hermitian part due to the uncertainty on the soft boundaries between the lead and the interior region. This problem is handled by introducing a boundary surface Bloch operator ($\mathcal{L}_B$) to the

original Hamiltonian ($\mathcal{H}$). The resulting Hamiltonian is called the "Bloch Hamiltonian", $\tilde{\mathcal{H}} = \mathcal{H} + \mathcal{L}_B$, and it is Hermitian in the interior region. The eigenfunctions of the Bloch Hamiltonian are used to expand a scattering solution in the interior region. In practice, the Bloch Hamiltonian is diagonalized using a set of basis functions. Different basis sets are used such as Wigner-Eisenbud functions, variational basis functions, atomic orbitals, etc.

By matching scattering solutions in the above two regions one can solve for the scattering matrix. The distinctive feature of this approach is that we need to solve the eigenvalue problem only once for a system.

Transition to phonon

The application of this technique to phonon transport is theoretically interesting and provides an efficient calculation tool for phonon scattering in nanoscale systems. The major distinction of the phonon problem is that it deals with finite difference equations instead of the Schrödinger equation, which is a differential equation. For electrons, there are an infinite number of eigenstates of the Bloch Hamiltonian. This means that any solution involves a high energy cut-off given by the largest eigenvalue considered in the Bloch Hamiltonian. In the phonon case, there is no sense to oscillations that have a wavelength shorter than the distance between atoms in a single unit cell. Therefore, there are not more than $3N$ modes associated with the interior region, and such convergence is not an issue. The electron case also suffers convergence issues related to the choice of basis used for solutions of the Bloch Hamiltonian. Since the scattering

solution can have any amplitude and derivative on the boundary, it is important that the basis functions share the same feature. This motivates a variety of different approaches in choosing a basis. In contrast, in the phonon case we merely solve for the normal modes of the system, and there is no such ambiguity. However, we cannot find the normal modes of the interior region dynamical matrix since it is coupled to the leads. The solution is to define a "Bloch dynamical matrix" by removing the coupling to the leads in analogy to the Bloch Hamiltonian. The coupling between the interior region and the leads forms a matrix, which we also call the Bloch operator.

The free electrons in the leads always follow a quadratic dispersion such that $E = \hbar^2 q^2/2m$. However, phonons have more complex behavior. There are different polarization modes such as longitudinal, transverse, acoustic and optical, and different phonon subbands due to the lateral confinement. Each of these modes follows a different dispersion relation which needs to be taken into account. The details of the lead phonon modes are calculated by solving the dynamical matrix in a lead unit cell. This is not the issue in section 3.2, where we have only one phonon mode in the lead. The relative motions of atoms come to effect when we have diatomic leads, which is the motivation to section 3.3. Moreover, in chapter 3, this is handled in a more generalized way.

Furthermore, the electron problem has the advantage of well-defined boundaries. In the phonon case there are interactions between atoms at different locations which involves interactions such as nearest neighbors, next nearest neighbors, etc. This yields broad boundaries in contrast to the electrons.

The main focus of this dissertation is to adopt traditional RMT to calculate phonon scattering addressing the above mentioned distinctness. In section 3.2, we give a basic development of the RMT considering a uniform mono-atomic chain. Taking a step further, we expand the formalism to a diatomic chain in section 3.3. A generalized approach of the theory is presented in chapter 4.

3.2 Phonon model

The system consists of a finite central region connected to two semi-infinite leads representing the thermal reservoirs. We define two boundaries on the first atom of each leads coupled to the central region. See Fig.(3.1). The central region with boundary atoms is called the *interior region* (IR), which is the main scattering center of the problem. This region is comprised of interfaces, boundaries and impurities. Impurities can be created by changing the mass or the force constant. There are N atoms in the interior region including the two boundary atoms. The region outside the boundaries is called the *asymptotic region*. This region comprises the semi-infinite leads that are assumed to be periodic. We restrict all the non-uniform structure to the IR. The entire system is indexed by j, called the common index, where $j = 0$ on the left boundary atom and increases positively to the right. The leads are indexed by j_l, where $l = 1(2)$ is the lead 1(2). The atoms at $j_l = 0$ are the boundary atoms, which are also $j = 0$ and $j = N - 1$ in the common index. The lead index increases positively outward the interior region. The mass of the j^{th} atom is m_j and the force constant between two consecutive atoms is $k_{j,j+1}$. The mass and the force constant

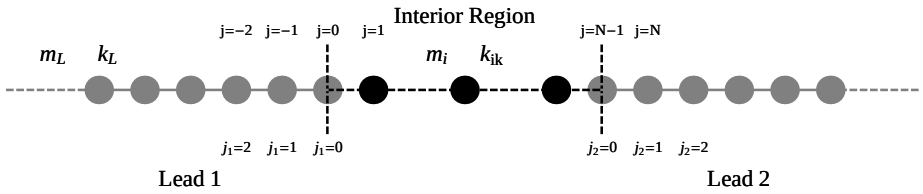

Figure 3.1: Schematic of the 1D system having two leads and an interior region. The index j is the atom index of the whole space and j_1 and j_2 are the lead index defined only on the leads symmetrically. The leads have uniform masses (m_{j_l}) and force constants (k_{j_l,j_l+1}) whereas the interior region can have different masses and force constants. The index m_j is the mass of the j^{th} atom and $k_{j,j+1}$ is the force constant between two consecutive atoms.

of leads are also denoted by the lead index as m_{j_l} and k_{j_l,j_l+1}.

Our goal is to estimate the thermal conductance of the system. We keep both leads in thermal equilibrium at different temperatures: T_1 and T_2. At steady state there is a constant thermal flux flowing through the system. Since our leads are periodic there are well defined phonons distributed according to the Bose-Einstien distribution function, $\eta_{1,2}(\omega) = \{\exp(\hbar\omega/k_B T_{1,2}) - 1\}^{-1}$. Each of these phonons contribute to the thermal flux ballistically such that a phonon of energy $\hbar\omega$ in lead 1

will be transmitted in to lead 2 with its full energy with a probability of transmission $\Gamma(\omega)$, which is determined by the atomic constituents in the IR. The heat current from lead 1 to 2 ($Q_{1,2}$) can be given by the Landauer Formula (Eq.3.1)[36, 38].

$$Q_{1,2} = \int_{\omega_{min}}^{\omega_{max}} \frac{d\omega}{2\pi} \hbar\omega \left(\eta_L(\omega) - \eta_R(\omega)\right) \Gamma(\omega), \tag{3.1}$$

In the linear response regime, where $\Delta T \ll T$, $\Delta T = |T_1 - T_2|$ and $T = (T_1 + T_2)/2$, the thermal conductance (σ) of the system can be expressed as follows,

$$\sigma = \frac{k_B^2 T}{h} \int_{x_{min}}^{x_{max}} dx \frac{\Gamma(x) x^2 e^x}{(e^x - 1)^2}, \tag{3.2}$$

where $x = \frac{\hbar\omega}{k_B T}$, $\hbar$ is the reduced Planck constant and k_B is the Boltzmann constant.

3.2.1 R-matrix theory formalism.

The dynamics of the system described in the previous section follows an infinite set of coupled equations. Equation (3.3) and (3.4) describe the leads and the interior region respectively in the harmonic approximation and they are labeled by a common index. In above equations, interactions are limited to the nearest neighbors and only the longitudinal vibrations are considered. This is not a requirement, and one can readily extend the theory to three-dimensions(3D) and consider long range interactions. This is addressed in chapter 4 through a generalized formalism.

$$m_j \omega^2 u_j = -k_{j-1,j} u_{j-1} + \left(k_{j-1j} + k_{jj+1}\right) u_j - k_{jj+1} u_{j+1} \quad \text{for} \quad N - 1 \ll j \ll 0 \tag{3.3}$$

$$
\begin{aligned}
m_0\omega^2 u_0 &= \underline{-k_{-10}u_{-1}} + (k_{-10}+k_{01})\,u_0 - k_{01}u_1 && \text{for} \quad j=0 \\
m_j\omega^2 u_j &= -k_{j-1,j}u_{j-1} + (k_{j-1j}+k_{jj+1})\,u_j - k_{jj+1}u_{j+1} && \text{for} \quad N-1 \gg j \gg 0 \\
m_{N-1}\omega^2 u_{N-1} &= -k_{N-2N-1}u_{N-2} + (k_{N-2N-1}+k_{N-1N1})\,u_{N-1}\underline{-k_{N-1N}u_N} && \text{for} \quad j=N-1
\end{aligned}
\tag{3.4}
$$

The above set of equations can also be written as the matrix form,

$$
\left(\omega^2\mathcal{M} - \mathcal{K}\right)\mathbf{u} = 0, \tag{3.5}
$$

where $\mathcal{M}$ and $\mathcal{K}$ are the diagonal matrix of masses and the dynamical matrix defined the whole system. Therefore, $\mathcal{M}$ and $\mathcal{K}$ are infinite dimensional matrices and $\mathbf{u}$, is also an infinite dimensional vector whose entries are the displacement of each atom. We rewrite the above equation(3.5) in mass normalized form as follows,

$$
\left(\omega^2\mathcal{I} - \tilde{\mathcal{K}}\right)\mathbf{u} = 0, \tag{3.6}
$$

where $\mathcal{I}$ is the identity matrix, $\tilde{\mathcal{K}} = \mathcal{M}^{-\frac{1}{2}}\mathcal{K}\mathcal{M}^{-\frac{1}{2}}$ is the mass normalized dynamical matrix. This guarantees that if we choose any finite region of the system, the matrix $\tilde{\mathcal{K}}$ is always Hermitian. Following steps analogous to the electronic case, we can develop IR and lead solutions individually in a mathematically consistent manner so that they can be matched at the boundaries to calculate the scattering amplitudes of a given phonon of energy $\hbar\omega$. Below we describe the derivation of IR and leads solutions and then the scattering amplitude of phonons.

3.2.2 Interior region solution

We can not solve the system of equations for the IR since it is coupled to the leads. In equation (3.4), the underlined terms are the additional terms lying outside the

interior region. These can be written in a matrix form called the "Bloch Operator" ($\mathcal{L}_{\mathcal{B}}$). The matrix element of the Bloch operator ($\mathcal{L}_{\mathcal{B}}(\alpha,\beta)$) can be expressed as,

$$\mathcal{L}_{\mathcal{B}}(\alpha,\beta) = -\left(\tilde{k}_{0,-1}\delta_{\alpha,0}\delta_{\beta,-1} + \tilde{k}_{N-1,N}\delta_{\alpha,N-1}\delta_{\beta,N}\right), \tag{3.7}$$

where $\tilde{k}_{0,-1} = k_{0,-1}/\sqrt{m_0 m_{-1}}$, $\tilde{k}_{N-1N} = k_{N-1N}/\sqrt{m_{N-1}m_N}$. The term $\mathcal{L}_{\mathcal{B}}\mathbf{u}$ gives the coupling terms in equation (3.4).

$$\mathcal{L}_{\mathcal{B}}\mathbf{u} = -\begin{pmatrix} \tilde{k}_{0-1}u_{-1} & 1 \\ 0 & 2 \\ \vdots & \vdots \\ 0 & \vdots \\ \tilde{k}_{N-1N}u_N & N \end{pmatrix} \tag{3.8}$$

Now $\mathcal{L}_{\mathcal{B}}\mathbf{u}$ can be subtracted from equation (3.6) yielding,

$$\left(\omega^2\mathcal{I} + \tilde{\mathcal{K}} - \mathcal{L}_{\mathcal{B}}\right)\mathbf{u} = -\mathcal{L}_{\mathcal{B}}\mathbf{u}. \tag{3.9}$$

Therefore, we can block out the IR from $\left(\tilde{\mathcal{K}} - \mathcal{L}_{\mathcal{B}}\right)$, since there is no coupling to the rest. We call the matrix $\left(\tilde{\mathcal{K}} - \mathcal{L}_{\mathcal{B}}\right)$ the "Bloch dynamical matrix" in analogy with the "Bloch Hamiltonian" in the electronic problem. Alternatively, we can choose that $\left(\tilde{\mathcal{K}} - \mathcal{L}_{\mathcal{B}}\right)$ be only defined in the IR so that equation (3.9) still holds in the IR. Since the matrix $\left(\tilde{\mathcal{K}} - \mathcal{L}_{\mathcal{B}}\right)$ is Hermitian, we can find eigenvalues (λ_n^2) and eigenvectors ($\mathbf{v}^n$) as follows.

$$\left(\tilde{\mathcal{K}} - \mathcal{L}_{\mathcal{B}}\right)\mathbf{v}^{(n)} = \lambda_n^2\mathbf{v}^{(n)}. \tag{3.10}$$

The eigenvectors $\mathbf{v}^{(n)}$'s are orthonormal and also form a complete set. Hence, a general solution in the IR can be written as,

$$\mathbf{u}_{IR} = \sum_n A_n \mathbf{v}^{(n)}. \tag{3.11}$$

Plugging this into the left hand side of the equation(3.9) yields,

$$\sum_n \left(\lambda_n^2 - \omega^2\right) A_n \mathbf{v}^{(n)} = \mathcal{L}_{\mathcal{B}} \mathbf{u}. \tag{3.12}$$

By taking the inner product with $\mathbf{v}^{n,\dagger}$ ($\dagger$ is the transpose conjugate),

$$A_n = -\frac{\mathbf{v}^{(n)\dagger} \mathcal{L}_{\mathcal{B}} \mathbf{u}}{\lambda_n^2 - \omega^2}. \tag{3.13}$$

By plugging A_n into eq. 3.11, the IR solution can be expressed as,

$$\mathbf{u}_{IR} = -\sum_n \mathbf{v}^{(n)} \frac{\mathbf{v}^{(n)\dagger} \mathcal{L}_{\mathcal{B}} \mathbf{u}}{\lambda_n^2 - \omega^2}. \tag{3.14}$$

3.2.3 Leads solution

Since the choice of the leads is always periodic we can establish plane wave solutions in the leads. This can be expressed as $e^{\pm i q_l j_l a}$, where q_l is the wave vector of lead "l". We assume the leads are uniform so that the phonon dispersion of the lead can be given by $\omega = 2\sqrt{k_L/m_L}\sin(q_l a/2)$. A plane wave of unit amplitude coming towards the interior region in lead l_0 can scatter off into the lead l. The corresponding scattering amplitude is written as $\mathcal{S}_{ll_0}$. The scattering solution in lead l for waves coming from lead l_0 can be written as follows.

$$u_{ll_0}(j_l) = \delta_{ll_0} e^{-i q_l j_l a} + \mathcal{S}_{ll_0} e^{i q_l j_l a} \tag{3.15}$$

The scattering amplitudes $\mathcal{S}_{ll_0}$ form a 2×2 scattering matrix ($\mathcal{S}$) whose diagonal elements refer to the reflection coefficient ($\mathbf{r}$) and the off diagonals are the transmission coefficients ($\mathbf{t}$).

$$\mathcal{S} = \begin{pmatrix} \mathbf{r} & \mathbf{t} \\ \mathbf{t}^\dagger & \mathbf{r} \end{pmatrix} \tag{3.16}$$

The transmission probability $\Gamma(\omega) = \mathbf{t}\mathbf{t}^\dagger$.

3.2.4 Solving for the scattering matrix

The scattering solution in lead l should match the IR solution at the boundary where $j = 0$ and $j = N - 1$ ($j_1 = j_2 = 0$ in the lead index). This yields,

$$\delta_{ll_0} + \mathcal{S}_{ll_0} = -\sum_n (\mathbf{v}^{(n)})_l \frac{\mathbf{v}^{(n)\dagger} \mathcal{L}_\mathcal{B} \mathbf{u}}{\lambda_n^2 - \omega^2}, \tag{3.17}$$

where $(\mathbf{v}^{(n)})_l$ is the value at the boundary l of the eigenvector $\mathbf{v}^n$. At this point we can calculate the expression $\mathbf{v}^{(n)\dagger} \mathcal{L}_\mathcal{B} \mathbf{u}$ in equation (3.17). Since $\mathcal{L}_\mathcal{B}$ always acts on the atoms in the lead, which are coupled to the IR, the elements in the vector $\mathbf{u}$ can be given by the scattering solution of the leads (eq.3.15). Consequently, the expression can be written as the sum of two terms,

$$\mathbf{v}^{(n)} \mathcal{L}_\mathcal{B} \mathbf{u} = -\sum_{l'} (\mathbf{v}^{(n)\dagger})_{l'} \frac{k_{01}^{(l')}}{m_{j_{l'}=0}} \left(\delta_{l'l_0} e^{-iq_{l'}a} + \mathcal{S}_{l'l_0} e^{iq_{l'}a} \right), \tag{3.18}$$

where $k_{01}^{(1)}$(the superscript denotes the lead), in lead index, is equal to k_{0-1} in common index. Similarly, $k_{01}^{(2)} = k_{N-1,N}$. Plugging this into equation (3.17), we obtain the R-matrix equation,

$$\delta_{ll_0} + \mathcal{S}_{ll_0} = \sum_{l'} \mathcal{R}_{ll'} \frac{k_{01}^{(l')}}{m_{j_{l'}=0}} \left(\delta_{l'l_0} e^{-iq_{l'}a} + \mathcal{S}_{l'l_0} e^{iq_{l'}a} \right), \tag{3.19}$$

In which the R-Matrix($\mathcal{R}$) is defined as,

$$\mathcal{R}_{ll'} = \sum_n \frac{(\mathbf{v}^{(n)\dagger})_l (\mathbf{v}^{(n)})_{l'}}{\lambda_n^2 - \omega^2}. \tag{3.20}$$

It must be noted that the R-matrix depends only on the boundary value of the IR eigenvectors and the eigenvalues. The R-matrix equation produces a set of linear equations that can be solved for the scattering matrix $\mathcal{S}$. By rearranging the terms in eq.3.19, we can write,

$$\sum_{l'} \left(\delta_{ll'} \mathcal{S}_{l'l_0} - \mathcal{R}_{ll'} \frac{k_{01}^{(l')}}{m_{j_{l'}=0}} \mathcal{S}_{l'l_0} e^{iq_{l'}a} \right) = \sum_{l'} \left(\mathcal{R}_{ll'} \frac{k_{01}^{(l')}}{m_{j_{l'}=0}} \delta_{l'l_0} e^{-iq_{l'}a} - \delta_{ll'}\delta_{l'l_0} \right). \tag{3.21}$$

This can be write in matrix form as,

$$\mathcal{S}\left(\mathcal{I} - \mathcal{T}\right) = -\left(\mathcal{I} - \mathcal{T}^*\right), \tag{3.22}$$

where, $\mathcal{T}_{ll'} = \mathcal{R}_{ll'} \frac{k_{01}^{(l')}}{m_0} e^{iq_l a}$ and $\mathcal{I}$ is a unit matrix. The scattering matrix, $\mathcal{S}$ can be calculated by the equation,

$$\mathcal{S} = -\left(\mathcal{I} - \mathcal{T}\right)^{-1} \cdot \left(\mathcal{I} - \mathcal{T}^*\right), \tag{3.23}$$

3.2.5 Application and results

In previous sections, we developed a mechanism to calculate phonon transmission on the atomic level based on the RMT. It is important to show the functionality of this formalism. First, we use RMT to investigate the effect of mass impurities on the thermal transport in one-dimension (1D). We consider a 1D chain of atoms of masses $m_j = m_{j_l} = 1.0$ and $k_{j,j+1} = 1.0$ for all j. Then we define two boundaries keeping 25 atoms in the IR. The results are independent of the location of these boundaries as

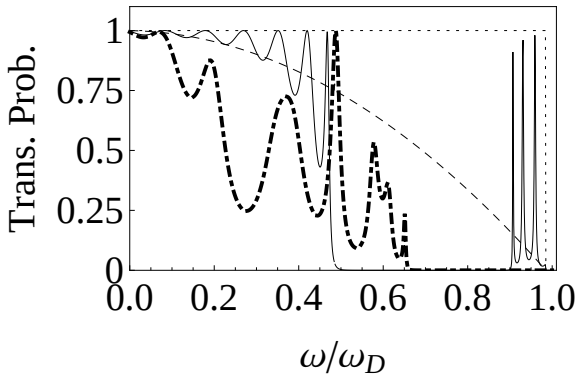

Figure 3.2: Transmission probability (Γ) as a function of dimensionless frequency (ω/ω_D). The dotted line is for the uniform chain. Dashed line is for the inclusion of single impurity of $m^1_{Im} = 2.0$ and periodic diatomic structure of 7 unit cells with masses m^1_{Im} and $m^2_{Im} = 0.6$ is given by the solid line. The thick dotted dashed line is for the random distribution of 14 atoms with masses m^1_{Im} and m^2_{Im}.

long as they are in the periodic region. A mass impurity is made by changing the mass of an atom in the middle of the IR to $m^{(1)}_{Im} = 2.0$. The dashed line in Fig.(3.2) shows the transmission probability calculated in the presence of a single mass impurity. The dotted line is for the uniform chain. Then we incorporate another mass of $m^{(2)}_{Im} = 0.6$ with $m^{(1)}_{Im}$ forming a periodic diatomic structure in the middle of the IR. The number of unit cells included is seven. The corresponding transmission is plotted by the solid line in fig.(3.2). We can see the forbidden region having zero transmission. Next the above two masses are randomly distributed replacing 14 atoms in the interior region. In this case the transmission is depicted by the dotted dashed line. Now we calculate the thermal conductance as a function of temperature. The dimensionless thermal

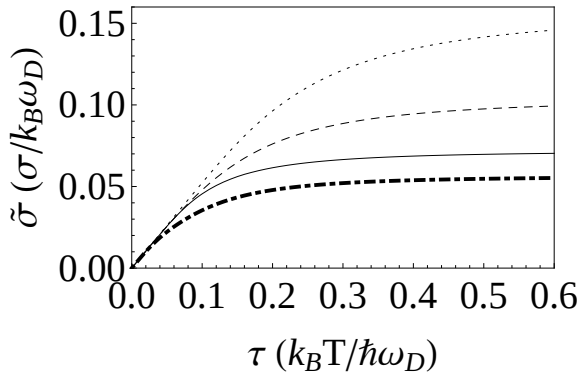

Figure 3.3: Dimensionless thermal conductance ($\tilde{\sigma}$) as a function of dimensionless temperature ($\tilde{\sigma}$). The dotted line is for the uniform chain. Dashed line is for the inclusion of single impurity of $m^1_{Im} = 2.0$ and periodic diatomic structure of 7 unit cells with masses m^1_{Im} and $m^2_{Im} = 0.6$ is given by the solid line. The thick dotted dashed line is for the random distribution of 14 atoms with masses m^1_{Im} and m^2_{Im}.

conductance ($\tilde{\sigma} = \sigma/(k_B\omega_D)$) is defined as,

$$\tilde{\sigma} = \frac{1}{2\pi}\int_0^1 d\tilde{\omega}\frac{\Gamma(\tilde{\omega})\tilde{\omega}^2 e^{\tilde{\omega}/\tilde{\tau}}}{\tilde{\tau}^2\left(e^{\tilde{\omega}/\tilde{\tau}}-1\right)^2}, \tag{3.24}$$

where $\tilde{\tau} = (k_BT/\hbar\omega_D)$, Debye or cut off frequency $\omega_D = 2\sqrt{k_L/m_L}$ which is equal to 2.0 in this problem, $\tilde{\omega} = \omega/\omega_D$. The corresponding dimensionless thermal conductance for the cases described earlier is plotted in Fig.(3.3). The random distribution of masses shows the lowest thermal conductance. The random distribution of masses might creates localized states suppressing the phonon transport whereas the periodic structures are preferred for traveling waves.

Next, we demonstrate how the interface coupling influences the phonon transmission. There are 12 atoms in the IR. The 2 atoms at the boundaries are of the same

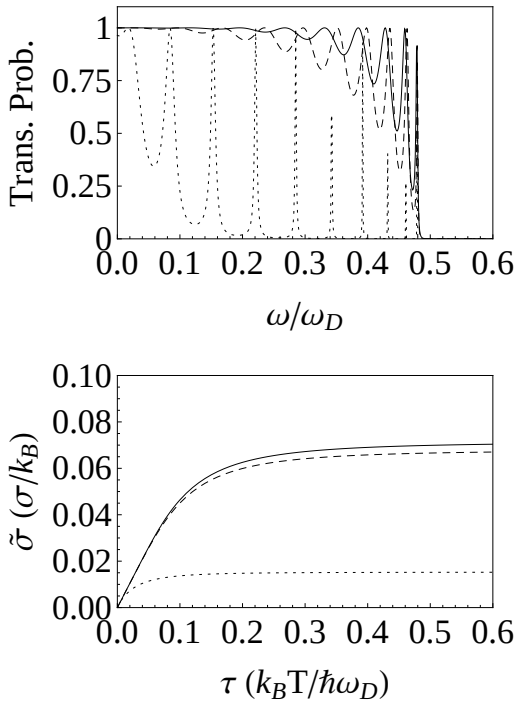

Figure 3.4: (a) Transmission probability (Γ) as a function of dimensionless frequency (ω/ω_D). The dotted line is for $k_{IC} = 0.1$, Dashed line is for $k_{IC} = 0.5$ and the solid line represent the $k_{IC} = 0.75$.(b) Dimensionless thermal conductance as a function of dimensionless temperature.

type of the leads in which the mass and the force constants are same as the previous case. The mass and the force constants of the 10 atoms in the interior region are $m_j = 2.0$ for $1 \leq j \leq 10$ and $k_{j,j+1} = 0.5$ for $1 \leq j \leq 10$. The interface coupling is k_{IC}. Figure 3.4a shows the transmission for 3 different values of $k_{IC} = 0.1, 0.5, 0.75$ and fig.3.4b shows the corresponding thermal conductance as a function of temperature. When the interface coupling increased from 0.1 to $k_{IC} = 0.5$ a huge increase in thermal conductance is observed, while further increments of k_{IC} yield only poor enhancement of the thermal conductance. Therefore, to maximize the interface ther-

mal transport having the lowest coupling strength of the system for the interface is sufficient.

3.3 R-matrix theory for a diatomic chain

In the previous section (3.2), the basic development of RMT to phonon scattering is discussed with one dimensional uniform mono-atomic chains. Now we are going to extend the formalism to a more complicated system. We extend the formalism to a diatomic chain, where two phonon branches, called optical and acoustic, contribute to the thermal transport. The important difference in this case is in the relative vibration of the consecutive atoms with different masses.

3.3.1 Theoretical extension

Figure 3.5 shows the 1D system, where the lead has two atoms in the basis. The masses of the two atoms in the basis are denoted by m and M. The mass m is at the even values of j_l starting from $j_l = 0$ and mass M is at the odd values of j_l. Further these two atoms have different polarization amplitudes denoted by ϵ_p^b, where p is the phonon branch(either Optical (O) or Acoustic(A)) and b refers to the atom type (mass m or M).

The matrix element of the bloch operator can be written as,

$$\mathcal{L}_{\mathcal{B}}(\alpha,\beta) = -\left(\tilde{k}_{0-1}\delta_{\alpha,0}\delta_{\beta,-1} + \tilde{k}_{N-1N}\delta_{\alpha,N-1}\delta_{\beta,N}\right), \tag{3.25}$$

where $\tilde{k}_{0,-1} = \tilde{k}_{N-1,N} = k/\sqrt{mM}$. The IR solution can be expressed as previously by eq.4.19. The major change is in the leads solutions. Since the leads are periodic

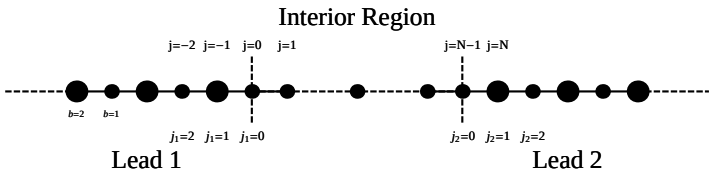

Figure 3.5: Model 1D system having diatomic leads. j is the atomic index of the IR and j_j $(l = 1, 2)$ is the lead index. The mass of the atoms at even values of j_l(including zero) is m and that of at the odd values of j_l is M.

lattices we can establish plane wave solutions. We consider an atom with $j_l = 2N_l$, where N_l is the atomic index. By the Newton's law we can write,

$$\begin{aligned} m\ddot{X}^m_{j_l} &= k\left(X^M_{j_{l+1}} - X^m_{j_l}\right) + k\left(X^M_{j_{l-1}} - X^m_{j_l}\right) \\ M\ddot{X}^M_{j_{l+1}} &= k\left(X^m_{j_{l+2}} - X^M_{j_{l+1}}\right) + k\left(X^m_{j_l} - X^M_{j_{l+1}}\right) \end{aligned} \tag{3.26}$$

It can be defined $K_1 = k/m$ and $K_2 = k/M$ for the convenience and the eq.3.26 can be written as,

$$\begin{aligned} \ddot{X^m_{j_l}} &= -K_1\left(2X^m_{j_l} - X^M_{j_{l-1}} - X^M_{j_{l-1}}\right) \\ \ddot{X^M_{j_{l+1}}} &= -K_2\left(2X^M_{j_{l+1}} - X^m_{j_l} - X^m_{j_{l+2}}\right) \end{aligned} \tag{3.27}$$

We are seeking for normal modes solutions of the form,

$$\begin{aligned} X^m_{j_l} &= A\exp[i(qaj_l - \omega t)] \\ X^M_{j_l+1} &= B\exp[i(qa(j_l+1) - \omega t)], \end{aligned} \tag{3.28}$$

where A and B are the polarization amplitudes of atoms m and M respectively. By

plugging eq.3.28 into eq.3.27 yields two linear equations of A, B and ω^2.

$$\begin{aligned} \omega^2 A &= K_1 \left(2A - Be^{-iqa} - Be^{iqa}\right) \\ \omega^2 B &= K_2 \left(2B - Ae^{-iqa} - Ae^{iqa}\right) \end{aligned} \tag{3.29}$$

The above equations can be written in the matrix form,

$$\begin{pmatrix} \omega^2 - 2K_1 & 2K_1 \cos(qa) \\ 2K_2 \cos(qa) & \omega^2 - 2K_2 \end{pmatrix} \begin{pmatrix} A \\ B \end{pmatrix} = 0. \tag{3.30}$$

This has nontrivial solution when the determinant of the coefficient matrix is zero. Then we can find the phonon dispersion $\omega^2(q)$ and the coefficients A and B which are also a function of wave vector (q).

Since the interior region eigenvectors are in the mass normalized form, it is necessary to write the leads solutions also in the mass normalized form. The mass normalized lead solution can be expressed as,

$$\begin{aligned} x^m_{j_l} &= \tfrac{\epsilon^m_p}{\sqrt{m}} \exp[i(qaj_l - \omega t)] \\ x^M_{j_l+1} &= \tfrac{\epsilon^M_p}{\sqrt{M}} \exp[i(qa(j_l+1) - \omega t)], \end{aligned} \tag{3.31}$$

where $\epsilon^m_p = mA$ and $\epsilon^M_p = MB$.

The scattering solution in the leads can be expressed as,

$$u_{ll_0}(j_l) = \delta_{ll_0} \frac{\epsilon^b_p}{\sqrt{m_b}} e^{-iqj_l a} + \mathcal{S}_{ll_0} \frac{\epsilon^b_p}{\sqrt{m_b}} e^{iqj_l a}. \tag{3.32}$$

The index b is introduced for the convenience in which $b = 1$ (m_1) is atom of mass m and $b = 2(m_2)$ is atom of mass M. The IR solution from eq.4.19 is,

$$\mathbf{u}_{IR} = -\sum_n \sum_{l'} \frac{(\mathbf{v}^n)\left(\mathbf{v}^{n\dagger}\right)_{l'}}{\lambda_n^2 - \omega^2} \frac{k}{\sqrt{mM}} \left(\delta_{l'l_0} \frac{\epsilon^2_p}{\sqrt{M}} e^{-iqa} + \mathcal{S}_{l'l_0} \frac{\epsilon^2_p}{\sqrt{M}} e^{iqa}\right). \tag{3.33}$$

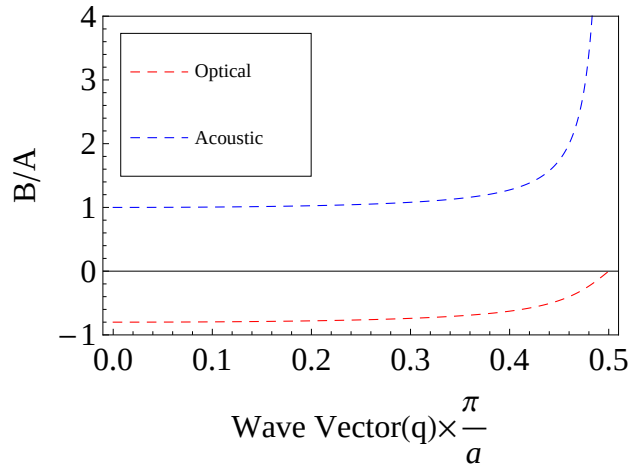

Figure 3.6: Ratio of the relative polarization amplitudes(B/A). The red line refers to the optical branch and the blue line refers to the acoustic branch. This was calculated when the $m = 1.0$, $M = 1.25$ and $k = 1.0$.

By matching the IR solution and the leads solution at the boundary l'' yields,

$$\left(\delta_{l''l_0}\frac{\epsilon_p^1}{\sqrt{m}} + \mathcal{S}_{l''l_0}\frac{\epsilon_p^1}{\sqrt{m}}\right) = -\sum_{l'}\mathcal{R}_{l''l'}\frac{k}{\sqrt{mM}}\left(\delta_{l'l_0}\frac{\epsilon_p^2}{\sqrt{M}}e^{-iqa} + \mathcal{S}_{l'l_0}\frac{\epsilon_p^2}{\sqrt{M}}e^{iqa}\right). \tag{3.34}$$

Eq.3.34 generates 4 equations to solve for 4 unknowns in the 2×2 scattering matrix $\mathcal{S}$. Further, this can be reduced to the matrix form and the scattering matrix can be expressed as previous,

$$\mathcal{S} = -\left(\mathbf{I} - \tilde{\mathcal{T}}\right)^{-1} \cdot \left(\mathbf{I} - \tilde{\mathcal{T}}^*\right) \tag{3.35}$$

where, $\tilde{\mathcal{T}}_{l''l'} = \mathcal{R}_{l''l'}\frac{k}{m}\frac{B}{A}e^{iqa}$.

3.3.2 Results for a diatomic chain

For example consider a linear atomic chain of $m = 1.0$, $M = 1.25$ and $k = 1.0$. Fig.3.6 shows the ratio of polarization amplitudes (B/A) as a function of wave vector(q),

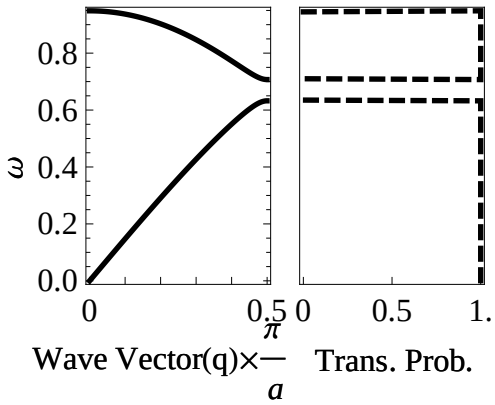

Figure 3.7: (Left) Phonon dispersion of the diatomic chain of $m = 1.0$, $M = 1.25$ and $k = 1.0$. (Right) Transmission probability from R-Matrix theory for diatomic chain of $m = 1.0$, $M = 1.25$ and $k = 1.0$.

which goes to $+1$ and $-m/M$ for acoustic and optical branches respectively in the long wave length limit($qa \to 0$). Figure 3.7 shows the phonon dispersion and the calculated transmission probability. We get unit transmission for all of the available frequencies of this diatomic chain. Now we replace the leads of the uniform 1D chain with the above diatomic lead. This is a situation that can occur in an experiment where the leads are mixed with some impurity atoms. This gives a lower transmission of phonons than the uniform structure. The frequencies are normalized by the cut-off frequency(ω_D) of the uniform 1D chain of $m = 1.0$ and $k = 1.0$. The dimensionless thermal conductance is plotted against the dimensionless temperature in fig.3.9. Consequently, the diatomic leads give the lower thermal conductivity than the uniform.

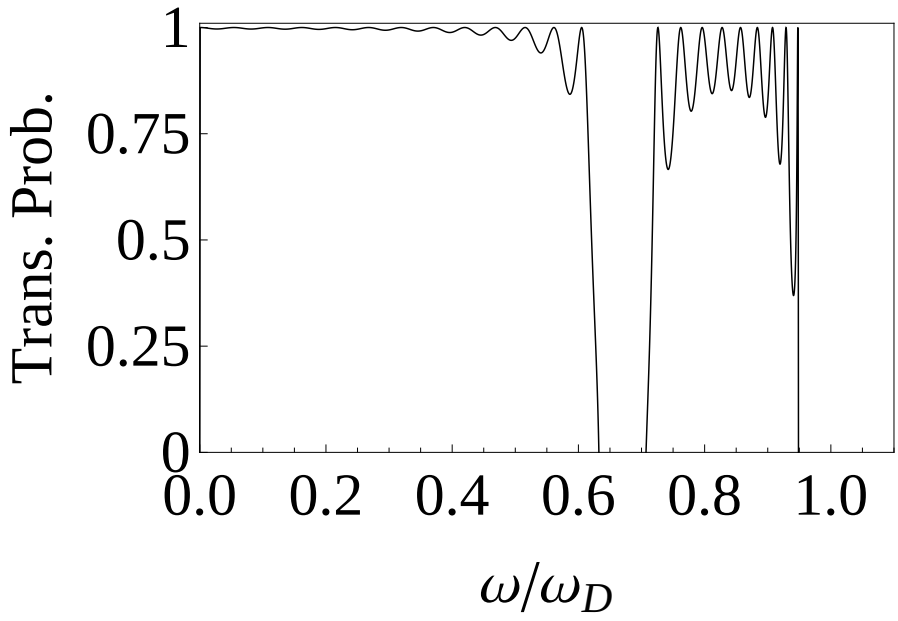

Figure 3.8: Plot of the transmission probability as a function of dimensionless frequency (ω/ω_D). ω_D is the cut off frequency of uniform 1D chain ($\omega_D = 2.0$ when $m = 1.0$and $k = 1.0$). The leads are diatomic chain of $m = 1.0$, $M = 1.25$ and $k = 1.0$. Both acoustic and optical mode s in the leads are transmitted through the acoustic mode in the interior region.

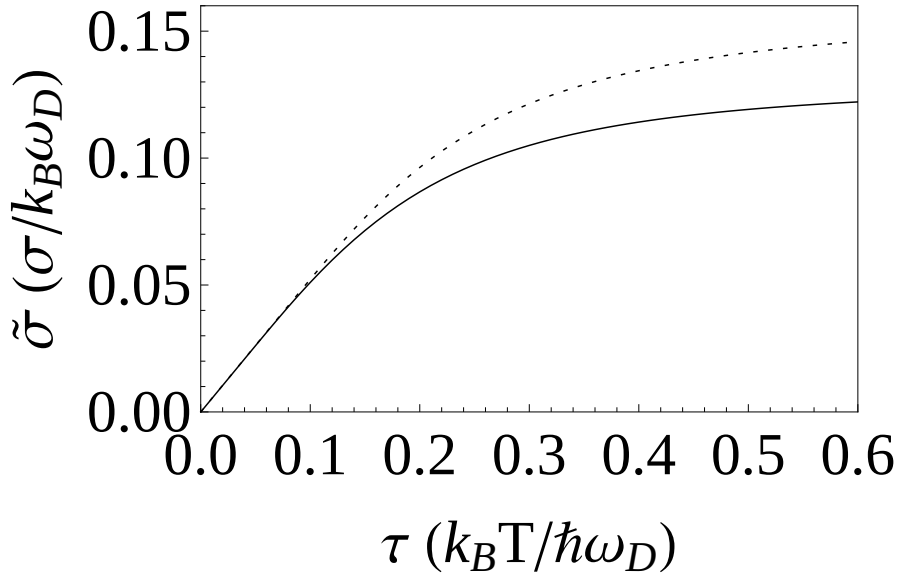

Figure 3.9: Dimensionless thermal conductance as a function of dimensionless temperature. The dotted line is for the uniform mono atomic chain($m = 1.0$ and $k = 1.0$) and the solid line is for the uniform monoatomic chain sandwiched by two diatomic leads of $m = 1.0$, $M = 1.25$ and $k = 1.0$.

3.4 Conclusion

In this chapter, we present the basic development of the RMT to phonon scattering using 1D atomic chains. We first, develop the theory for a 1D system having only one phonon mode in leads. Then, we move to case where we have two phonon modes (optical and acoustic) in the leads. We observe that the important factor to the scattering calculation is the ratio of the polarization amplitudes of the consecutive atoms. We also present results for each of the above cases. We briefly discuss the effect of mass impurities and the coupling constant to the thermal transport in one-dimension.

Chapter 4

R-matrix Theory: A General Approach

Most of the content presented here appear in Numerical Heat Transfer, Part B: Fundamentals 60(4), 2011.

In this chapter, the RMT developed in the previous chapter (Ch.3) to calculate phonon scattering in the harmonic limit is generalized. In the previous chapter, we presented the basic development of the RMT considering only the one dimensional motion of a mono-atomic chain, where we only have one phonon mode at a given frequency. In this chapter, we particularly consider a system that has multiple phonon modes crossing at a given frequency. This is important in studying the three dimensional motion of mono-atomic systems as well as various nanostructures such as graphene nanoribbons and other dielectric nanowires.

In the general picture, leads are considered to be finite width nanowires, in which the atoms are also moving in the three dimensional space. In section 4.1, the scattering solution in the lead is constructed. The details of the different phonon branches are calculated solving the dynamical matrix of a unit cell of the lead. In section 4.2, the interior region solution and the form of the R-matrix is derived. The scattering solutions in above two regions are matched on an unit cell at the boundary to obtain a closed-form solution to the scattering matrix (sec.4.3). Finally, results are presented considering the three-dimensional(3D) motion of atoms of a mono atomic chain. We

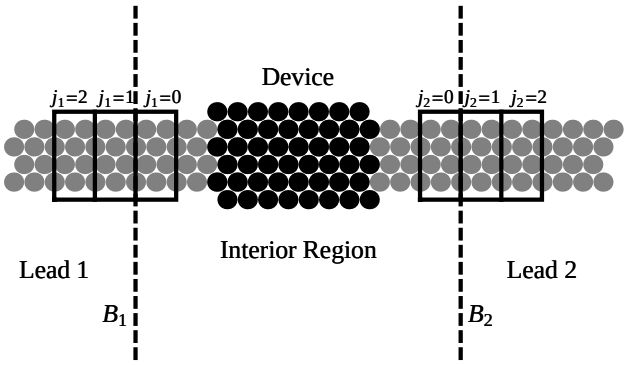

Figure 4.1: Schematic of the model system having two semi-infinite leads connected to a device. The leads are assumed to be periodic and two boundaries, B_1 and B_2, are defined in the periodic region. The region between boundaries is the *interior region* and the region outside is called the *asymptotic region*. The unit cells in the leads are depicted by the boxed regions. The lead lattice points are indexed symmetrically by j_l, where $l = 1(2)$ refers to the lead 1(2).

also discuss the interband transition of phonons, that can be present in the harmonic limit.

4.1 The system and the scattering picture

The essence of R-matrix theory is to divide the system into an interior region(IR) and two or more asymptotic regions. A finite size device is embeded in the IR. This device could be any 3D structure. The asymptotic regions are the semi-infinite nanowires (leads) connected to the IR (Fig.4.1). In the asymptotic regions, we assume the leads are narrow enough then the phonon transport in leads is strictly along the length

direction of the leads. In the lateral direction there are confined phonon modes which are also called the phonon subbands. Thus, we define an extended unit cell, depicted by the boxed regions in the fig.4.1, that has the periodicity in the length direction. Although R-matrix theory can handle any number of leads, for simplicity we consider the case of only two leads. It is straight forward to generalized to a system with many leads. The IR and the leads are seperated by a set of boundaries in the periodic region, which we denote by B_l. The unit cells in the leads are indexed by j_l, where $l = 1(2)$ is the lead 1(2). The lattice point $j_l = 0$ is at the boundary B_l in to the IR and j_l increases positively outward the IR. Our goal is to calculate the transmission probability of a phonon of angular frequency ω from lead 1 to 2, which is the quantity $\Gamma_{1,2}(\omega)$.

Since our leads are periodic there are well-defined phonons in each lead. In general the equations of motion of the system can be written as follows,

$$m_{j_l,b}\ddot{u}^{\alpha}_{j_l,b} = -\sum_{j'_l,b',\beta} \phi^{\alpha\beta}_{j'_l b',j_l b} u^{\beta}_{j'_l,b'} \tag{4.1}$$

where the harmonic limit force constants can be calculated by,

$$\phi^{\alpha\beta}_{j'_l b',j_l b} = \left(\frac{\partial^2 V}{\partial u^{\alpha}_{j_l b} \partial u^{\beta}_{j'_l b'}} \right)_{\forall u_{j_l b}=0} \tag{4.2}$$

where j_l, is the lattice index of lead l, b is the atom index in the basis. The Cartesian degree of freedom is represented by α and β, $m_{j_l,b}$ is the mass of the atom b within the unit cell j_l, $u^{\alpha}_{j_l b}$ is the displacement of the atom b in unit cell j_l in the direction α, and the symbol V refers to the many-coordinate inter-atomic potential. We seek

solutions to equation 4.1 of the following form,

$$u^{\alpha}_{j_l b} = \frac{1}{\sqrt{m_{j_l,b}}} \epsilon_{b,\alpha} e^{-i\omega t + i\mathbf{q}.\mathbf{R}_{j_l,b}} \tag{4.3}$$

By plugging this into eq.4.1, we can obtain the well known dynamical matrix equation [63],

$$\omega^2 \boldsymbol{\epsilon}^{p}_{b,\alpha} = \sum_{b'\beta} \mathcal{M}(q)^{\alpha,\beta}_{bb'} \boldsymbol{\epsilon}^{p}_{b',\beta}, \tag{4.4}$$

where the dynamical matrix $\mathcal{M}$ is,

$$\mathcal{M}(q)^{\alpha,\beta}_{bb'} = \left(\sum_{j_l - j'_l} \phi^{\alpha,\beta}_{j_l b, j'_l b'} \frac{e^{i\mathbf{q}.(\mathbf{R}_{j'_l b'} - \mathbf{R}_{j_l b})}}{\sqrt{m_{j_l,b} m_{j'_l,b'}}} \right). \tag{4.5}$$

The details of the phonons in each lead can be obtained by solving the dynamical equation over a unit cell. (All matrices are denoted by capital script letters, and vectors represented in bold-face.) The coordinate of the atom b in the unit cell j_l is given by $\mathbf{R}_{j_l,b} = \mathbf{R}_{j_l} + \mathbf{R}_b$, where $\mathbf{R}_{j_l}$ is the position of the lattice point j_l and $\mathbf{R}_b$ is the position of the atom b within a unit cell. The $\mathbf{q}$ is the wave vector, and $\boldsymbol{\epsilon}^{p}_{b,\alpha}$ is the polarization amplitude of atom b in direction α in phonon branch p. There are $3N_{uc}$ phonon branches in each lead, where N_{uc} is the number of atoms in the unit cell.

We can construct a scattering solution in the leads with these phonon modes. The scattering solution is comprised of three components: the incoming wave, the reflected wave and the transmitted wave. We consider an incoming phonon of frequency ω, whose energy is $\hbar\omega$, in lead l_0 which belongs to branch p_0. It can reflect into any phonon branch (p) available at ω in lead l_0 and transmit into any phonon branch (p) in lead l, which is different from l_0. We assume all the scattering processes are elastic and anharmonic interactions are neglected. As we defined our leads symmetrically,

the incoming waves are going in the direction of decreasing the lead lattice index j_l and the scattered waves (both reflected and transmitted) are going at the increasing direction of the lattice index. Thus, the incident/scattered components of the scattering solution can be written in terms of plane waves as, $\boldsymbol{\chi}^p\left(-\mathbf{q}^p(\omega)\right)/\boldsymbol{\chi}^p\left(\mathbf{q}^p(\omega)\right)$, where $\boldsymbol{\chi}^p\left(\mathbf{q}^p(\omega)\right)$ is a vector whose entries are the values of $\boldsymbol{\epsilon}_b^p \exp(-i\omega t + i\mathbf{q}^p(\omega).\mathbf{R}_{j_l,b})/\sqrt{m_b}$ of all the atoms in a unit cell. Now the scattering solution $(\mathbf{u}^l_{l_0,p_0}(\omega))$ of the lead l for above described scattering event can be written as,

$$\mathbf{u}^l_{l_0,p_0}(j_l) = \sum_p \left(\boldsymbol{\chi}^p(-\mathbf{q}^p(\omega))\delta_{p,p_0}\delta_{l,l_0} + \boldsymbol{\chi}^p(\mathbf{q}^p(\omega))\mathcal{S}^{l,p}_{l_0,p_0}(\omega)\right), \tag{4.6}$$

where, the first part inside the summation represents an incoming wave in mode p_0 in lead l_0 and the second part is the scattered wave. The scattering amplitude in branch p lead l is given by $\mathcal{S}^{l,p}_{l_0,p_0}(\omega)$, which is a complex number. The scattering amplitudes form a $2N_\omega \times 2N_\omega$ scattering matrix $\mathcal{S}(\omega)$, where the N_ω is the number of phonon branches at frequency (ω). The matrix elements of $\mathcal{S}$, when $l = l_0$ are the reflection coefficients and $l \neq l_0$ are the transmission coefficients.

From the scattering amplitudes, we can calculate the transmission probabilities. The transmission probability is the ratio of the energy fluxes carried by each vibrational wave. The transmission probability from branch p_0 in lead l_0 to branch p in lead $l(\neq l_0)$ can be expressed as, $\Gamma^{lp}_{l_0p_0}(\omega) = \mathcal{S}^{l,p\dagger}_{l_0,p_0}(\omega)\mathcal{S}^{l,p}_{l_0,p_0}(\omega)c^p(\omega)/c^{p_0}(\omega)$, where $c^p(\omega)$ is the phonon velocity of the branch p at frequency ω. The $\dagger$ refers to the complex conjugate. A derivation of the energy normalization is given in section 2.4.

Thus the transmission probability from lead l_0 to $l(\neq l_0)$ is,

$$\Gamma_{ll_0}(\omega) = \sum_{pp_0} \Gamma^{lp}_{l_0p_0}(\omega). \tag{4.7}$$

4.2 R-matrix

The dynamics of the entire system can be described by an infinite set of coupled equations, which are usually written as matrix form,

$$\left(\omega^2\mathcal{I} + \mathcal{K}\right)\mathbf{u} = 0, \tag{4.8}$$

where $\mathcal{I}$ is the identity matrix, $\mathbf{u}$ is the displacement vector and $\mathcal{K}$ is the mass normalized force constant matrix. The matrix elements of $\mathcal{K}$ can be calculated as,

$$\mathcal{K}^{\alpha,\beta}_{j,j'} = \frac{1}{\sqrt{m_j m_{j'}}}\phi^{\alpha,\beta}_{jj'}, \tag{4.9}$$

where j refer to a common index of atoms used to label all the atoms in the system. The matrix $\mathcal{K}$ can be expressed more descriptively using the block matrices: $\mathcal{K}_{IR}$ is defined only in the finite IR, $\mathcal{K}_{L_l}$ is defined in the lead l that is infinite, and K_{IR,L_l} is the coupling between the interior region and the leads.

$$\mathcal{K}\mathbf{u} = \begin{pmatrix} \mathcal{K}_{L_1} & \mathcal{K}_{L_1,IR} & 0 \\ \mathcal{K}_{IR,L_1} & \mathcal{K}_{IR} & \mathcal{K}_{IR,L_2} \\ 0 & \mathcal{K}_{L_2,IR} & \mathcal{K}_{L_2} \end{pmatrix} \begin{pmatrix} \mathbf{u}_{L_1} \\ \mathbf{u}_{IR} \\ \mathbf{u}_{L_2} \end{pmatrix}, \tag{4.10}$$

where $\mathbf{u}_{L_l}$ and $\mathbf{u}_{IR}$ are the displacement vectors of atoms in lead l and the IR.

It is natural to describe the IR by normal modes of vibrations. However, in our scattering problem the IR is connected to semi-infinite leads and thus we can not

solve for the normal modes. The solution is to solve the equations of motion for a different, but related physical system. When solving the continuum Schrodinger equation in a finite region, a "Bloch operator" is included to solve the problem of non-Hermiticity of the kinetic energy operator [60, 61]. The resulting Hamiltonian is called the "Bloch Hamiltonian", which is explicitly Hermitian inside a finite region. In the phonon problem we define a "Bloch operator ($\mathcal{L}_B$)", which includes the couplings between the IR and the leads as follows,

$$\mathcal{L}_{\mathcal{B}} = \begin{pmatrix} 0 & \mathcal{K}_{L_1,IR} & 0 \\ \mathcal{K}_{IR,L_1} & 0 & \mathcal{K}_{IR,L_2} \\ 0 & \mathcal{K}_{L_2,IR} & 0 \end{pmatrix}. \tag{4.11}$$

The term $\mathcal{L}_{\mathcal{B}}\mathbf{u}$ gives the coupling forces between the IR and the leads. It can involve interactions of any finite range, e.g. nearest neighbor, next nearest neighbor, etc. We subtract the term $\mathcal{L}_{\mathcal{B}}\mathbf{u}$ from the both side of the eq.4.8 yielding,

$$\left(\omega^2 I + \mathcal{K} - \mathcal{L}_{\mathcal{B}}\right)\mathbf{u} = -\mathcal{L}_{\mathcal{B}}\mathbf{u}. \tag{4.12}$$

The matrix $(\mathcal{K} - \mathcal{L}_B)$ on the left is called the "Bloch dynamical matrix", in which the coupling between the two regions are removed. The eq.4.12 can be written in block matrices as follows,

$$\omega^2 \begin{pmatrix} \mathbf{u}_{L_1} \\ \mathbf{u}_{IR} \\ \mathbf{u}_{L_2} \end{pmatrix} + \begin{pmatrix} \mathcal{K}_{L_1} & 0 & 0 \\ 0 & \mathcal{K}_{IR} & 0 \\ 0 & 0 & \mathcal{K}_{L_2} \end{pmatrix} \begin{pmatrix} \mathbf{u}_{L_1} \\ \mathbf{u}_{IR} \\ \mathbf{u}_{L_2} \end{pmatrix} = - \begin{pmatrix} 0 & \mathcal{K}_{L_1,IR} & 0 \\ \mathcal{K}_{IR,L_1} & 0 & \mathcal{K}_{IR,L_2} \\ 0 & \mathcal{K}_{L_2,IR} & 0 \end{pmatrix} \begin{pmatrix} \mathbf{u}_{L_1} \\ \mathbf{u}_{IR} \\ \mathbf{u}_{L_2} \end{pmatrix}. \tag{4.13}$$

We can extract the center row of the eq.4.13, which describes the IR,

$$\left(\omega^2 \mathbf{u}_{IR} + \mathcal{K}_{IR}\mathbf{u}_{IR}\right) = -\sum_l {\mathcal{L}_{\mathcal{B}}}^l \mathbf{u}_{L_l}, \tag{4.14}$$

where ${\mathcal{L}_{\mathcal{B}}}^l = \mathcal{K}_{IR,L_l}$. In the "Bloch dynamical matrix" the IR can be solved independently. We find eigenvalues (λ_n) and eigenvectors ($\mathbf{v}^{(n)}$) of $\mathcal{K}_{IR}$ according to,

$$\left(\lambda_n^2 + K_{IR}\right)\mathbf{v}^{(n)} = 0. \tag{4.15}$$

These eigenvectors are orthonormal and form a complete set as the mass normalized force constant matrix is always Hermitian. A general solution in the IR can be expanded using the above eigenvectors as follows,

$$\mathbf{u}_{IR} = \sum_n A_n \mathbf{v}^{(n)}. \tag{4.16}$$

By plugging this in to the left hand side of the equation (4.14) yields,

$$\sum_n \left(\lambda_n^2 - \omega^2\right) A_n \mathbf{v}^{(n)} = \sum_l {\mathcal{L}_{\mathcal{B}}}^l \mathbf{u}_{L_l}. \tag{4.17}$$

By taking the inner product with $\mathcal{V}^{n\dagger}$ we find,

$$A_n = \sum_l \frac{\mathbf{v}^{(n)\dagger} {\mathcal{L}_{\mathcal{B}}}^l \mathbf{u}_{L_l}}{\lambda_n^2 - \omega^2}. \tag{4.18}$$

Finally, the scattering solution in the *IR* can be expressed as,

$$\mathbf{u}_{IR} = \sum_{n,l} \mathbf{v}^{(n)} \frac{\mathbf{v}^{(n)\dagger}\left({\mathcal{L}_{\mathcal{B}}}^l \mathbf{u}_{L_l}\right)}{\lambda_n^2 - \omega^2}. \tag{4.19}$$

According to the eq.4.10 and 4.11, Bloch operator of lead l, ${\mathcal{L}_{\mathcal{B}}}^l$, has infinite number of columns and $3N$ rows, where N is the number of atoms in the IR. However there are non-zero couplings only between a subset of atoms in the IR with a subset of

atoms in the leads, in the vicinity of the boundary B_l. Since the boundary is defined in the periodic region, we assume that the minimum size of the coupling regions to be unit cells at either side of the boundary. This is a reasonable (but not essential) assumption for most practical situations. Therefore we can construct a matrix of dimensions $3N_{uc} \times 3N_{uc}$ that contains the non-zero couplings in ${\mathcal{L}_{\mathcal{B}}}^l$. This effective part of the Bloch operator is denoted by $\widetilde{{\mathcal{L}_{\mathcal{B}}}^l}$. Now we replace $\mathbf{u}_{L_l}$ by $\mathbf{u}^l_{l_0 p_0}(j_l = 1)$, of which the entries are the displacements of the atoms in the unit cell at lattice point $j_l = 1$. Similarly $\left(\mathbf{v}^{(n)}\right)_l$ contain the normal modes amplitudes of the atoms in the unit cell at $j_l = 0$. Now we can replace $\mathbf{v}^{n\dagger}\left({\mathcal{L}_{\mathcal{B}}}^l \mathbf{u}_{L_l}\right)$ by $\left(\mathbf{v}^{(n)\dagger}\right)_l \left(\widetilde{{\mathcal{L}_{\mathcal{B}}}^l}\, \mathbf{u}^l_{l_0 p_0}(j_l = 1)\right)$ in eq.4.19.

In the electron transport problem, the R-matrix relates the value of the wave function to its normal derivative at the boundary of the scattering region and the normal derivative at the boundary serves as the Bloch operator [60, 61]. The phonon version of the R-matrix ($\mathcal{R}$) can be defined as follows,

$$\mathbf{u}^{l''}(j_{l''} = 0) = \sum_{s'',s',l'} \boldsymbol{\xi}^{s''} \mathcal{R}^{s'',s'}_{l'',l'} \boldsymbol{\xi}^{s'\dagger} \widetilde{{\mathcal{L}_{\mathcal{B}}}^{l'}}\, \mathbf{u}^{l'}(j_{l'} = 1), \tag{4.20}$$

$$\mathcal{R}^{s'',s'}_{l'',l'} = \sum_n \frac{\boldsymbol{\xi}^{s''\dagger} (\mathbf{v}^{(n)})_{l''} (\mathbf{v}^{(n)})^\dagger_{l'} \boldsymbol{\xi}^{s'}}{\lambda_n^2 - \omega^2}, \tag{4.21}$$

where $\boldsymbol{\xi}^s$'s are a set of unit vectors that are orthonormal and complete in the $3N_{uc}$

dimensional space. These vectors can be chosen arbitrarily and a possible choice is,

$$\boldsymbol{\xi}^{(1)} = \begin{pmatrix} 1 \\ 0 \\ 0 \\ 0 \\ 0 \\ \vdots \end{pmatrix}, \quad \boldsymbol{\xi}^{(2)} = \begin{pmatrix} 0 \\ 1 \\ 0 \\ 0 \\ 0 \\ \vdots \end{pmatrix}, \quad \cdots, \quad \boldsymbol{\xi}^{(n)} = \begin{pmatrix} 0 \\ \vdots \\ 0 \\ 1 \\ 0 \\ \vdots \end{pmatrix}. \tag{4.22}$$

Eq.4.20 is obtained by matching the lead solution and the interior region solution at the unit cell at $j_l = 0$. In the phonon problem, the R-matrix relates the displacement vector at $j_{l''} = 0$ to that at $j_{l'} = 1$ through the Bloch operator.

4.3 Scattering matrix

The scattering matrix ($\mathcal{S}$) can be obtained by plugging the explicit form of the scattering solution in the lead ($\mathbf{u}^l_{l_0 p_0}$) from eq.4.6 in to the R-matrix equation (4.20). By plugging $\mathbf{u}^{l''}_{l_0 p_0}(j_l = 0)$ and $\mathbf{u}^{l''}_{l_0 p_0}(j_l = 1)$ from eq.4.6 to eq.4.20 and taking the projection of both side on to $\boldsymbol{\epsilon}^{p''}$, we can obtain,

$$\begin{gathered} \textstyle\sum_{p'''} \boldsymbol{\epsilon}^{p''} \boldsymbol{\chi}^{p'''}(-\mathbf{q}^{p'''}; \mathbf{R}_{j_l=0}) \delta_{p''' p_0} \delta_{l'' l_0} + \boldsymbol{\epsilon}^{p''} \boldsymbol{\chi}^{p'''}(\mathbf{q}^{p'''}; \mathbf{R}_{j_l=0}) \mathcal{S}^{l'' p'''}_{l_0 p_0} = \\ \textstyle\sum_{s'' s' l' p'} \boldsymbol{\epsilon}^{p''} \boldsymbol{\xi}^{s''} \mathcal{R}^{s'' s'}_{l'' l'} \left[\left(\boldsymbol{\xi}^{s' \dagger} \mathcal{L}^{l'}_B \boldsymbol{\chi}^{p'}(-\mathbf{q}^{p'}; \mathbf{R}_{j_l=1}) \right) \delta_{p' p_0} \delta_{l' l_0} + \left(\boldsymbol{\xi}^{s' \dagger} \mathcal{L}^{l'}_B \boldsymbol{\chi}^{p'}(\mathbf{q}^{p'}; \mathbf{R}_{j_l=1}) \right) \mathcal{S}^{l' p'}_{l_0 p_0} \right] \end{gathered} \tag{4.23}$$

We define a matrix ($\mathcal{B}$) for the convinent as follows,

$$\mathcal{B}^{l'' p''}_{l' p'} = \sum_{s'' s'} \boldsymbol{\epsilon}^{p''} \boldsymbol{\xi}^{s''} \mathcal{R}^{s'' s'}_{l'' l'} \left(\boldsymbol{\xi}^{s' \dagger} \mathcal{L}^{l'}_B \boldsymbol{\chi}^{p'}(\mathbf{q}^{p'}; \mathbf{R}_{j_l=1}) \right) \tag{4.24}$$

We rewrite eq.4.23 rearranging the parts and inserting $\mathcal{B}$.

$$\begin{aligned}\textstyle\sum_{p'''} \boldsymbol{\epsilon}^{p''} \boldsymbol{\chi}^{p'''}(-\mathbf{q}^{p'''}; \mathbf{R}_{j_l=0}) \delta_{p'''p_0} \delta_{l''l_0} - \sum_{l'p'} \mathcal{B}_{l'p'}^{l''p''}(-\mathbf{q}^{p'}) \delta_{p'p_0} \delta_{l'l_0} = \\ \textstyle\sum_{l'p'} \mathcal{B}_{l'p'}^{l'''p''}(\mathbf{q}^{p'}) \mathcal{S}_{l_0p_0}^{l'p'} - \sum_{p'''} \boldsymbol{\epsilon}^{p'''} \boldsymbol{\chi}^{p''}(\mathbf{R}_{j_l=0}) \mathcal{S}_{l_0p_0}^{l'''p''}.\end{aligned} \tag{4.25}$$

Let's focus on the R.H.S. of the eq.4.25. It can be written as,

$$\begin{aligned}\textstyle\sum_{l'p'} \left(\mathcal{B}_{l'p'}^{l'''p''}(\mathbf{q}^{p'}) \mathcal{S}_{l_0p_0}^{l'p'} - \delta_{l'''l'} \boldsymbol{\epsilon}^{p''} \boldsymbol{\chi}^{p'}(-\mathbf{q}^{p'}; \mathbf{R}_{j_l=0}) \mathcal{S}_{l_0p_0}^{l'p'} \right) \\ = -\left(\mathcal{A}(\mathbf{q}) - \mathcal{B}(\mathbf{q}) \right) \mathcal{S},\end{aligned} \tag{4.26}$$

where $\mathcal{A}_{l'p'}^{l'''p''} = \boldsymbol{\epsilon}^{p''} \boldsymbol{\chi}^{p'}(\mathbf{q}^{p'}; \mathbf{R}_{j_l=0}) \delta_{l'''l'}$. Similarly, we can show the L.H.S. of eq.4.25 is $(\mathcal{A}(-\mathbf{q}) - \mathcal{B}(-\mathbf{q}))$. Thus, we can express the scattering matrix as,

$$\mathcal{S}(\omega) = -\left[\mathcal{A}(\mathbf{q}) - \mathcal{B}(\mathbf{q}) \right]^{-1} . \left[\mathcal{A}(-\mathbf{q}) - \mathcal{B}(-\mathbf{q}) \right], \tag{4.27}$$

Equation (4.27) is our key expression for the scattering matrix. The matrices $\mathcal{A}$ and $\mathcal{B}$ are independent of the number of atoms in the IR. It is the R-matrix that represents the IR in the scattering calculation. In order to construct the matrices $\mathcal{A}$, $\mathcal{B}$ and $\mathcal{R}$, we only need to calculate for the normal modes of the IR in the Bloch dynamical matrix and the lead phonons. The appealing feature is that these details are needed to be calculated only once for a system.

4.4 Results

For instance, we consider the 3D motion of a one dimensional chain of atoms. The force constants are taken to be $k_{xx} = 1.0, k_{yy} = 0.5$ and $k_{zz} = 0.25$. All the masses are set to 1.0. There are three phonon branches in the leads. The phonon dispersion is shown in fig.4.2. The three acoustic phonon modes are one longitudinal acoustic mode

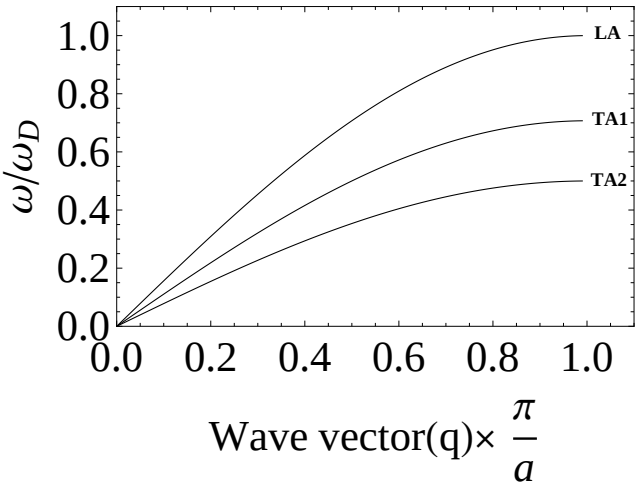

Figure 4.2: Phonon dispersion for the three dimensional motion of the lead. The three acoustic phonon modes are one longitudinal acoustic mode(LA) and two transverse acoustic modes (TA1 and TA2). The two TA modes are non-degenerate because the force constants in each direction are chosen to be different.

(LA) and two transverse acoustic modes (TA1 and TA2). Their polarization can be given as $(1, 0, 0)$, $(0, 1, 0)$ and $(0, 0, 1)$. Figure 4.3 shows the transmission probability as a function of phonon frequency. The transmission probability (Γ) counts the number of phonon modes at each frequency, which is the desired variation of such a perfect system.

Interband transition of phonons

There exists elastic scattering of phonons in the harmonic approximation of the force constants. This scattering produces interband transitions of phonons according to the conservation laws of energy and momentum. Such an effect can be observed in

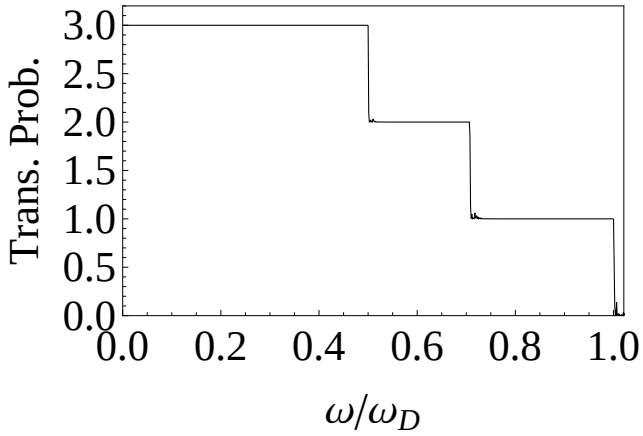

Figure 4.3: Plot of transmission probability vs. dimensionless frequency(ω/ω_D) for 3D motion of a one dimensional chain of atoms. The force constants are taken to be $k_{xx} = 1.0, k_{yy} = 0.5$ and $k_{zz} = 0.25$. All the masses are set to 1.0. The transmission probability is greater than the unity because there are more than one channel contribute to the thermal transport.

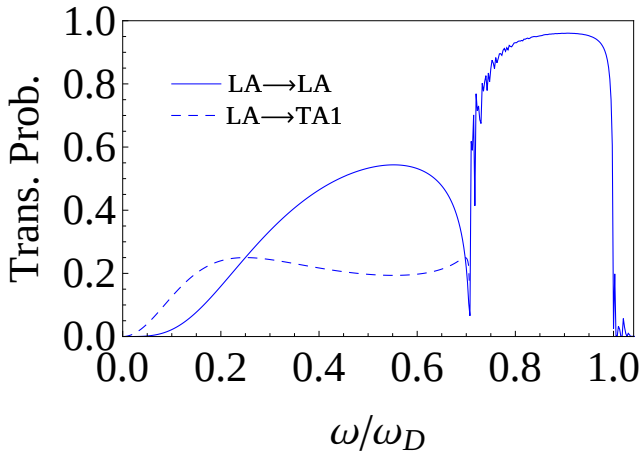

Figure 4.4: Transmission probability of phonons from LA to LA and LA to TA1 in the presence of a on-site cross coupling term on an atom in the interior region.

our model system by introducing a cross coupling term in the interior region. We include an on-site cross coupling term on an atom such that $k_{xy} = k_{yx} = 0.8$. This yields interband transitions from mode LA to TA1 and *vice versa*. Figure 4.4 shows the transmission probability from mode LA to LA and LA to TA1 calculated using the R-matrix theory. The total transmission between leads is shown in the fig4.5.

Such interband transitions are present in real systems and can be controlled by carefully engineering the interior region. In chapter 5, we further discuss these transitions in graphene nanostructures.

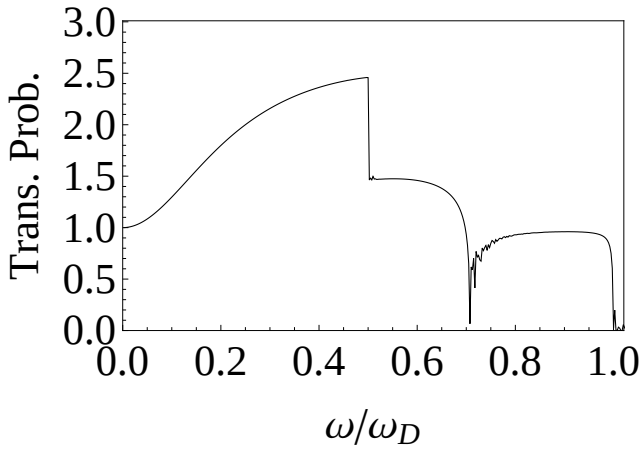

Figure 4.5: Plot of transmission probability vs. dimensionless frequency(ω/ω_D) between leads in the presence of the on-site cross coupling.

4.5 A comparison with non-equilibrium Green's function approach

In this section, a short description of the non-equilibrium green's function (NEGF) approach is presented. Next, we compare the results of the RMT with the conventional NEGF approach. In this context, both approaches produces the same results for the transmission probability.

The NEGF approach also first developed for calculating electron transmission in mesoscopic devices. This technique has also been successfully used in calculating phonon scattering [64, 65, 66, 67].

The central idea of this approach is to solve for the Green's function of the system. The set of governing equations of the infinite system can be written as the matrix form as in the equation 4.8. The frequency domain Green's function of this infinite

dimensional system can be expressed as [64, 65, 66, 67],

$$\left[(\omega + i\eta)^2\mathcal{I} - \mathcal{K}\right]\mathcal{G}(\omega) = \mathcal{I}, \tag{4.28}$$

where the Green's function can be calculated by the matrix inversion as,

$$\mathcal{G}(\omega) = \lim_{\eta\to 0}\left[(\omega + i\eta)^2\mathcal{I} - \mathcal{K}\right]^{-1}. \tag{4.29}$$

The $G(\omega)$ is an infinite dimensional matrix of Green's functions. We can defined the retarded surface green's function of the lead $l(1,2)$ as,

$$g^r_{L_l} = \lim_{\eta\to 0}\left[(\omega + i\eta)^2 - \mathcal{K}_{L_l}\right]^{-1}. \tag{4.30}$$

Now the equation 4.28 can be expanded using the block matrices defined in eq. 4.10.

$$\begin{pmatrix} -\mathcal{K}_{L_1} + (\omega+i\eta)^2 & -\mathcal{K}_{L_1,IR} & 0 \\ -\mathcal{K}_{IR,L_1} & -\mathcal{K}_{IR} + (\omega+i\eta)^2 & -\mathcal{K}_{IR,L_2} \\ 0 & -\mathcal{K}_{L_2,IR} & -\mathcal{K}_{L_2} + (\omega+i\eta)^2 \end{pmatrix} \begin{pmatrix} \mathcal{G}_{L_1,L_1} & \mathcal{G}_{L_1,IR} & \mathcal{G}_{L_1,L_2} \\ \mathcal{G}_{IR,L_1} & \mathcal{G}_{IR} & \mathcal{G}_{IR,L_2} \\ \mathcal{G}_{L_2,L_1} & \mathcal{G}_{L_2,IR} & \mathcal{G}_{L_2,L_2} \end{pmatrix} = \mathcal{I}. \tag{4.31}$$

The matrix product of the central row of the above equation gives the retarded Green's function of the isolated IR as,

$$\mathcal{G}^r_{IR,IR} = \left[(\omega + i\eta)^2 - \mathcal{K}_{IR,IR} - \Sigma^r_{L_1} - \Sigma^r_{L_2}\right]^{-1}, \tag{4.32}$$

where $\Sigma^r_{L_1} = \mathcal{K}_{IR,L_1} g^r_{L1} \mathcal{K}_{L_1,IR}$ and $\Sigma^r_{L_2} = \mathcal{K}_{IR,L_2} g^r_{L_2} \mathcal{K}_{L_2,IR}$ are the self energies due to the coupling of the IR with the lead 1 and 2.

Once we have calculated the the above Green's functions, the transmission probability of a phonon of energy $\hbar\omega$ from lead 1 to 2 can be calculated using the formula [65],

$$\Gamma(\omega) = Tr\left[\mathcal{G}^r_{IR,IR}\mathcal{P}_{L_1}\left(\mathcal{G}^r_{IR,IR}\right)^\dagger \mathcal{P}_{L_2}\right], \tag{4.33}$$

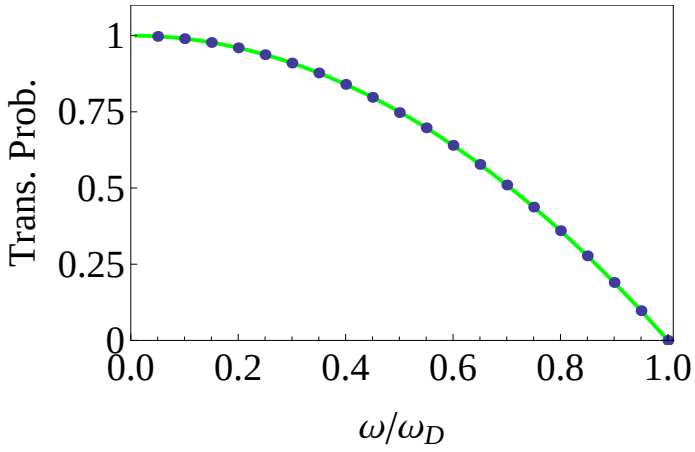

Figure 4.6: Comparison of the transmission probability through a 1D chain of atoms of $m = 1.0$ and $k = 1.0$ with a mass impurity of $m_{Im} = 2.0$ in the center of the IR. The full circles are the points calculated from the NEGF approach and the solid line is from the R-matrix theory.

where $\mathcal{P}_{L_n} = -2Im\Sigma^r_{L_n}$.

We calculate the transmission probability for a 1D chain of atoms of $m = 1.0$ and $k = 1.0$ with of mass impurity of $m_{Im} = 2.0$ in the middle of the IR. Figure 4.6 shows the transmission probability calculated from the NEGF and the R-matrix theory. We can observe that they lay exactly on each other.

Computational cost

One major advantage of RMT over the NEGF is the reduced computational cost. The NEGF approach involves lot of matrix inversion that needs to be done at each frequency point. The size of the matrices that need to be inverted also increases with increasing numbers of atoms in the interior region. Thus the computational cost increases rapidly with number of atoms in the interior region. In RMT, we only

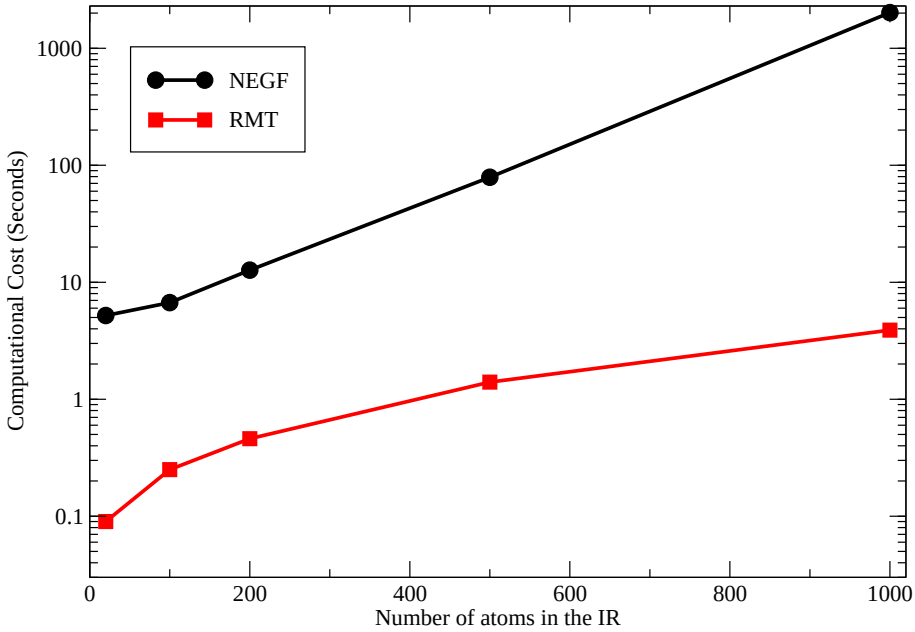

Figure 4.7: Plot of computational cost (in seconds) against the number of atoms in the interior region (IR). This is estimated using a 1D chain of atoms.

need to calculate eigenvalues and the eigenvectors of the IR only one time. In the scattering matrix calculation we only need to carry out a summation over the number of eigenmodes in the IR. Thus the computational cost in RMT is considerably lower and does not increases rapidly with the size of the IR.

Figure 4.7 shows the computational cost as a function of number of atoms in the IR for NEGF and the RMT approaches. We used a 1D chain of atoms in comparing the computational cost. The computational cost of NEGF increases rapidly with the number of atoms in the IR where as that of RMT is considerably lower and shows a slower increment with the number of atoms in the IR.

4.6 Conclusion

We present a generalized formalism of the RMT developed in the previous chapter. To demonstrate the validity and the applicability, we discuss the results obtained for the three dimensional motion of atoms in a mono atomic chain. We also discuss the interband transition of phonons in the presence of an on-site cross coupling term in the interior region. Moreover, we breifly discuss the non-equilibrium green's function (NEGF) for phonon transmission and compare the results from the RMT with the NEGF approach. We observe a nice matching of results from both approaches. We also investigate the computational cost for both approaches and find that the RMT is much computationally efficient. In the next chapter (Ch.4) we discuss the results applying RMT to graphene nanoribbons.

Chapter 5

Application to Graphene

Some of the content presented here appear in Numerical Heat Transfer, Part B: Fundamentals 60(4), 2011.

In this chapter we apply the RMT developed in the previous chapter to graphene. First we give a brief introduction to graphene. In particular, we focus on the thermal transport properties. Then we apply RMT to calculate phonon transmission though a graphene nanoribbon. We demonstrate how RMT is used to analyze the mode-to-mode transmission of phonons across a graphene nanoribbon. We discuss the effect of mass impurity and geometry to the transmission of flexural vibrational modes in graphene nanoribbons.

5.1 Graphene

Graphene is a single layer of carbon atoms arranged in a two dimensional honeycomb lattice (See Fig.5.1). Although the theoretical studies of graphene has been carried out for sixty years, it was only in 2004 that graphene was first mechanically exfoliated from graphite by Novoselov and Geim [68]. The exceptional electronic, mechanical and thermal properties of graphene have drawn tremendous attention from scientists in various disciplines such as high energy physics, condensed matter physics, biological physics, mechanical engineering and electrical engineering. In acknowledgement of their exceptional discovery, Novoselov and Geim were awarded the Nobel prize in

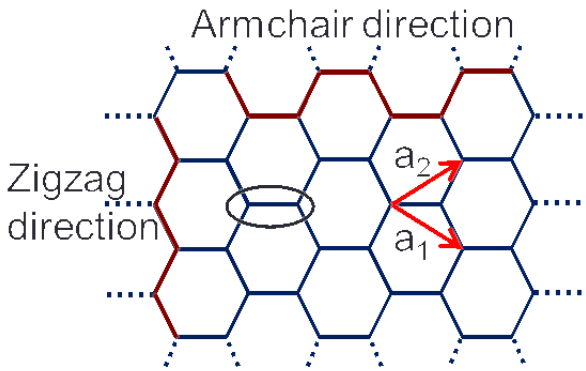

Figure 5.1: Skematic of the real space of graphene. The oval represent the unit cell of two dimensional graphene (2 atoms in the basis). "a_1" and "a_2" are primitive lattice vectors. The thick horizontal line is at the armchair direction and the vertical line is at the zigzag direction.

physics 2010. In this section, we briefly discuss these extraordinary properties of graphene.

5.1.1 Electronic properties

Graphene has semimetalic or zero-gap semiconducting characteristics where the conduction and the valence bands touch at the K and K' points in the Brillouine zone. The theoretical studies of electronic properties of graphene traces back to the work of Wallace in 1947 [69]. He carried out tight binding calculations to study the electronic band structure of a single layer of graphite and revealed the extraordinary linearly dispersive behavior ($E = \pm V_F|k|$,where E is the energy and k is the wave vector) of the low energy excitations near the K and K' point. As such, not like the other ordinary semiconductors and metals, electrons in graphene behave more like relativis-

tic quantum particles. These particles are called massless Dirac fermions, which can be described by the Dirac equation instead the Shrödinger equation. Thus, electrons in graphene provide an excellent environment to probe phenomena in high energy physics in a solid state experiment.

The other most interesting direction of graphene research is ballistic electronic device applications. The fermi velocity(V_F) of electrons in graphene is found to be about 1×10^6 m/s, which is 300 times smaller than the speed of light [70]. The ballistic lengths of electrons in graphene are on the submicrometer scale even at room temperature (300 K) and the electron mobility is as high as $15,000$ cm^2 V^{-1}s^{-1}, and is relatively insensitive to temperature [70]. This suggest the ability to probe quantum effects even at room temperatures in graphene. For instance the quantum Hall effect (QHE) has been observed at 300 K in graphene [70]. Thus graphene has become the most exciting material in the world.

5.1.2 Mechanical properties

Not only does it have exceptional electronic properties, graphene is unique in its mechanical properties. Graphene is one of the strongest materials in the world. The in-plane Young's modulus(Y) of graphene is about 1 TPa assuming the van der Waals thickness (0.335 nm) of graphene, which is the interlayer spacing of graphite [71, 72, 73]. The Young's modulus of a material is the slope of the linear fit to the stress vs. strain curve.

$$\mathcal{F}_x = Y\mathcal{E}_x, \tag{5.1}$$

where stress, $\mathcal{F}_x = F_x/A$, is the force applied per unit area and the strain $\mathcal{E} = (l - l_0)/l_0$, where l is the stretched of compressed length and the l_0 is the initial length. The intrinsic strength of graphene, which is the maximum stress that a pure defect free material can withstand, is about 130 GPa. One fascinating property of graphene is that it is flexible while at the same time it is strong in the 2D plane. Thus graphene has a potential to produce flexible electronics circuitry and devices.

The height fluctuations of graphene sheets, which are commonly known as ripples, are another interesting property. The uneven surface morphology of graphene can affect its electronic properties significantly [74]. There was a doubt about the stability of 2D membranes according to some theoretical predictions [75]. These membranes are believed to be crumpled due to long wavelength thermal fluctuations. However later it was explained that these fluctuations can be suppressed due to the anharmonic coupling between the flexing and in-plane vibrational modes [76]. Thus, 2D membranes can be exist but with large height fluctuations. Recently, a mechanism to control these ripples by manipulating the interactions of graphene with a substrate has been demonstrated experimentally [77, 78]. Thus, it opens a new path to tune the transport properties of graphene by tuning the interactions with a substrate. The anomalously large negative thermal expansion coefficient of graphene, which is about $-7 \times 10^{-6}\mathrm{K}^{-1}$ at 300 K is also an advantage in this process [79].

5.1.3 Thermal transport

Recent experimental measurements revealed that the thermal conductivity (κ) of single layer graphene is in the range of 3000 to 5000 W/mK, which is larger than that of diamond and graphite [23, 24]. The exceptionally high κ of graphene makes it a promising material for thermal management in nanoelectronics and other thermal applications such as realizing thermally conducting polymer composites.

Experimental measurements of the thermal conductivity of graphene is challenging because of its small size (single atomic layer) and large contact thermal resistance. Recently, a research group at University of California-Riverside [23], developed a optical method based on Raman spectroscopy to measure thermal conductivity of suspended single layer graphene. In graphene, the G band is a Raman active vibrational mode of frequency 1583 cm−1, which has strong dependence on the temperature. This sensitivity is used to estimate the temperature of the graphene sample. A tiny spot in a suspended region of the graphene sheet is heated using a laser and by measuring the local temperature rise as a function of laser power, they could extract the thermal conductivity of a single layer graphene. The reported thermal conductivity by this technique is in the range of 4800-5300 W/mK.

In another experiment a reduction of the thermal conductivity is reported when the graphene is in contact with a substrate [80]. They use Au/Cr resistance thermometers for both heating and temperature measurements. The measured thermal conductivity of a single layer graphene supported on a SiO2 substrate is about 600 W/mK. Such a low value of the thermal conductivity is attributed to the strong sup-

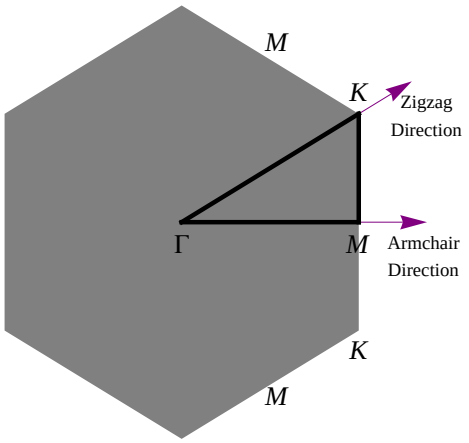

Figure 5.2: Schematic of the first brillioun zone of graphene. ΓK represent the zigzag directions and the ΓM represent the armchair directions.

pression of the flexural modes. Flexural modes are the out of plane vibrational modes which are available in thin membranes. Furthermore, they have also calculated the thermal conductivity using the Boltzmann transport equation and found that the contribution of flexural vibrational modes to the thermal conductivity of graphene is more than 80%.

Graphene can be viewed as a triangular Bravais lattice with a two atom basis. As shown in fig.5.1, the vectors "a_1" and "a_2" represent the primitive lattice vectors and the oval region represent a unit cell. The carbon-carbon bond length (a_0) in graphene is about $a_0 = 1.42\mathring{A}$ and $a_1 = a_2 = \sqrt{3}a_0$. There are two important crystallographic directions in graphene, which are armchair and the zigzag directions (fig.5.1). Since single layer graphene has 6-fold rotational symmetry, there are six of each above directions in graphene.

The first Brillioun zone of graphene is a hexagon as shown in the fig.5.2. In

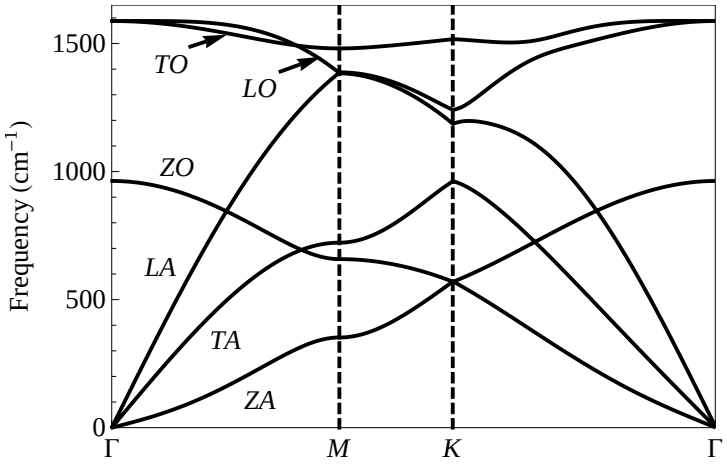

Figure 5.3: Phonon dispersion relation in the first brillioun zone.

momentum space, ΓK represents the zigzag directions and ΓM represent the armchair directions. Figure 5.3 shows the phonon dispersion calculated for a two dimensional graphene sheet. Phonon dispersion is calculated by solving the dynamical matrix equation 4.4. We construct the dynamical matrix with the force constants calculated from a second generation Brenner potential [81], which considers the interactions up to next nearest neighbour atoms. There are six phonon branches in graphene due to the fact that there are 2 carbon atoms in a unit cell and three degree of freedom of each atom. They are three acoustic branches and corresponding 3 optical branches. They are usually named LA-longitudinal acoustic, TA-transverse acoustic, ZA-flexural acoustic and corresponding optical branches as LO, TO and ZO. The exceptionally high thermal conductivity of graphene can be attributed to the large phonon velocities and the wide range of phonon frequencies of graphene. The phonon

velocity in the long wave length limit for LA mode is about $24,000$ m/s and TA mode is about $18,000$ m/s. The range of the phonon frequencies (0-1500 cm^{-1}) of graphene is about three times wider than that of silicon (0-500 cm^{-1}).

5.2 Thermal transport in graphene nanoribbons

Graphene nanoribbons (GNRs) are $10 \sim 100$ nm wide strips of graphene with high aspect ratios. We apply R-matrix theory to calculate the transmission of flexural vibrational modes of a GNR. Figure 5.4 shows a schematic of a zigzag graphene nanoribbon (ZGNR) of six zigzag chains in width. A unit cell is depicted by the boxed region and the lattice constant is given by a. When considering interactions up to the next nearest neighbors, there are non-zero couplings only between the atoms in adjacent unit cells. This supports the assumption we make in defining the effective part of the Bloch operator in sec.4.2. First we construct the $\mathcal{K}$ matrix as in eq.4.9 including a few unit cells in the leads. Then we extract the $\mathcal{K}_{IR}$ and $\mathcal{L}_B^l$ as described in eq.4.10 and 4.11. First, we calculate the phonon dispersion of flexural modes according to the eq.4.4. Figure 5.5a shows the phonon dispersion along the direction of the ribbon length, where $q_{\|}$ is the wave vector projected on to the length direction. There are 12 phonon branches available due to the fact that the unit cell has 12 atoms. These phonon branches represent different laterally confined phonon subbands that are specially available in nanowires. The acoustic branch is also available in large graphene sheets. The lowest lying optical branch, which has a twisting character (mode 2 in fig.5.7), can only exist in nanoribbons. In larger graphene sheets twisting

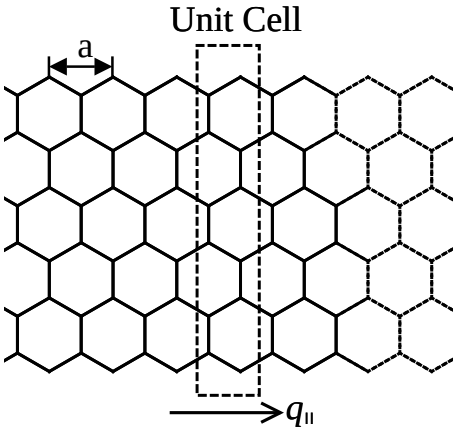

Figure 5.4: Schematic of a zigzag graphene nanoribbon (ZGNR) of six zigzag chains in width. A unit cell is depicted by the boxed region. The lattice constant in the leads is denoted by "a". The horizontal arrow shows the direction of $q_{\parallel}$.

modes are not present since they are energetically too costly. Figure 5.5b shows the calculated transmission probability ($\Gamma(\omega)$) from R-matrix theory. The transmission probability counts the number of phonon branches available at each frequency. Similar behavior of the transmission probability has been reported by non-equilibrium Green's function calculations [65, 66, 67].

We incorporate a larger mass (mass impurity of $m_{Im} = 100 m_{C^{12}}$) replacing one carbon atom in the center of the interior region [82]. We keep about 20 unit cells (240 atoms) in the interior region. Although this is not a realistic situation, it could

be analogous to a strong coupling to a heavy molecule. The calculated transmission probability for this case is shown by the dashed line in fig.5.5b. We observe that the overall transmission of phonons is reduced due to the heavy mass. In fig.5.6 we plot the thermal conductance (σ) as a function of the temperature. The thermal conductance of a ZGNR with the mass impurity (dashed line) is considerably lower than that of uniform ZGNR (solid line).

In R-matrix theory we are working on the real space displacement waves. This allows us to easily sketch the profile of the displacement waves during the scattering. This visualization is important to gain clear insight in to the scattering process and tuning the mode specific transmission of phonons. In fig.5.8, we sketch the displacement wave in the three regions: lead 1, interior region and lead 2, at frequency 50 cm^{-1} when the mass impurity is in the center of the interior region. We use the eq.4.6 for the leads and eq.4.19 for the interior region. The displacement waves in three regions matches nicely at the boundaries. There are two phonon subbands available at this frequency as shown in fig.5.7. The sketch in fig.5.8a is for the waves coming in mode 1, which is the acoustic mode. We observe that the propagation of the acoustic mode is considerably attenuated with the presence of the mass impurity. In the acoustic mode, all the atoms in the unit cell vibrate in-phase. Thus, the mass impurity prevent this in-phase motion. However, we observe that the twisting mode is not affected by the presence of the mass impurity in the middle as implied by the fig.5.8b. This can be attributed to the asymmetric polarization profile of the twisting mode (mode 2 in fig.5.7).

Next, we consider four different symmetric structures, that have different geometries in the middle. In fig.5.9a, two 6-ZGNRs are connected by a single aromatic carbon ring. In fig.5.9b, the two outermost zigzag chains are removed. A few atoms in the center of the interior region are removed while the edges are perfect in fig.5.9c. In fig.5.9d, additional zigzag chains are included in the both side of middle part of the interior region.

The lowest transmission function is observed for the structure "a" (green line in fig.5.10) and it gives the lowest thermal conductance (fig.5.11). Moreover, the phonon transmission of structure "b" is smaller than that of the structure "d", which is more like the inverse of the structure "b". Structure "c" has relatively larger thermal conductance among the structures with atoms removed.

The important aspects of R-matrix theory are the ability to analyse the mode specific transmission and the capability of plotting the scattering wave as we explained in the previous case. We study the mode specific transmission of the structure "a", which is the most promising device geometry of quantum devices. Figure 5.12a shows the phonon dispersion of the lowest lying three phonon modes and their mode profiles are shown in fig.5.12b. Mode P1 is at $\omega = 30cm^{-1}$, P2 is at $\omega = 60cm^{-1}$ and P3 is at $\omega = 120cm^{-1}$. Moreover, the mode P1 and P3 has symmetric mode profiles, whereas the mode P2 has an asymmetric mode profile (twisting mode).

At $\omega = 30$ cm^{-1}, we observe about 50% of the mode P1 transmit through the narrow constriction. Figure 5.13a visualise the propagation of this mode, which is the plotted displacement wave of the three regions. As a consequence of symmetries,

we observe strong cross coupling between the mode P1 and P3 at $\omega = 120$ cm^{-1}. The transmission coefficient from mode P3 to P3 is 0.05, whereas that of P3 to P1 is 0.25. There is no coupling between mode P3 and P2. Moreover, we observe complete reflection of the mode P2 from the narrow constriction. The scattering of this mode at $\omega = 60$ cm^{-1} is depicted in fig 5.13b. This suppression of transmission of mode P2 could be attributed to the mismatch between of the symmetries associated with the mode profile and the geometry of the structure. In further clarifying this argument, we consider an asymmetric structure, where the connecting aromatic ring is moved to a one side of the nanoribbon as shown in fig.5.14a. Interestingly, we observe a significant transmission of the mode P2. The transmission coefficient form mode P2 to P2 is 0.16 and that of mode P2 to P1 is 0.28. As a result we observe an increase in the transmission especially in the range of 40-350 cm^{-1}, where the twisting branch is located and also the thermal conductance (See fig.5.15).

5.3 Conclusion

In this chapter we presented results by applying the R-matrix theory to graphene nanoribbons. In the first part we give a brief introduction of graphene and its electronic, mechanical and thermal properties. We discuss the transmission of flexural modes across different geometries in the interior region. We demonstrate that the transmission of certain phonon modes can be manipulated by the geometry of the interior region. R-matrix theory is an excellent tool in analysing the mode to mode transmission which is useful in tuning the thermal transport in nanoscale systems.

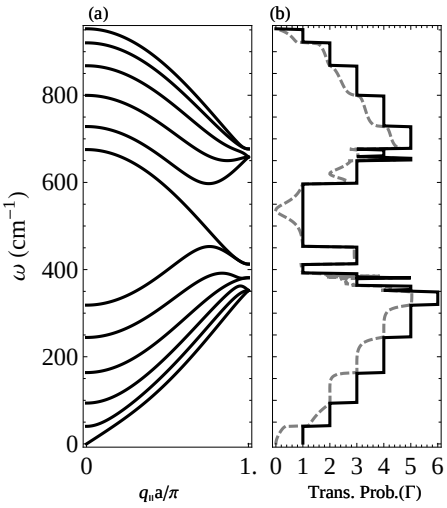

Figure 5.5: Phonon dispersion (a) of flexural vibrational modes of the ZGNR. The transmission probability (Γ) calculated for the perfect ZGNR from R-matrix theory (b). The transmission probability counts the number of phonon branches available at each frequency. The dashed line refers to the case where a larger mass in the middle of the IR. The frequency is measured in the units of cm^{-1}.

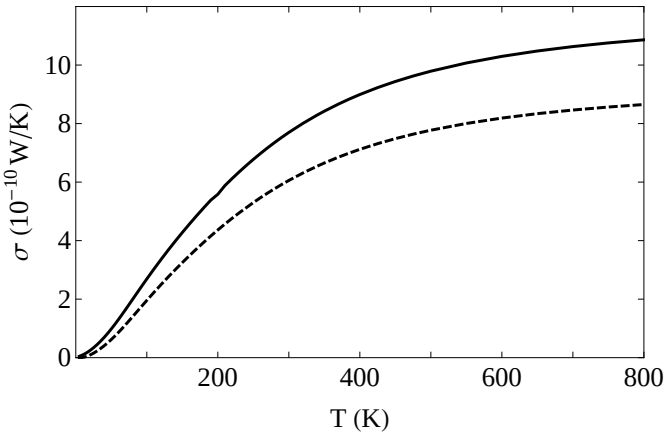

Figure 5.6: Thermal conductance due to the out of plane vibrations of the ZGNR as a function of temperature. The solid line is for the perfect structure and the dashed line is the result due to the larger mass in the center.

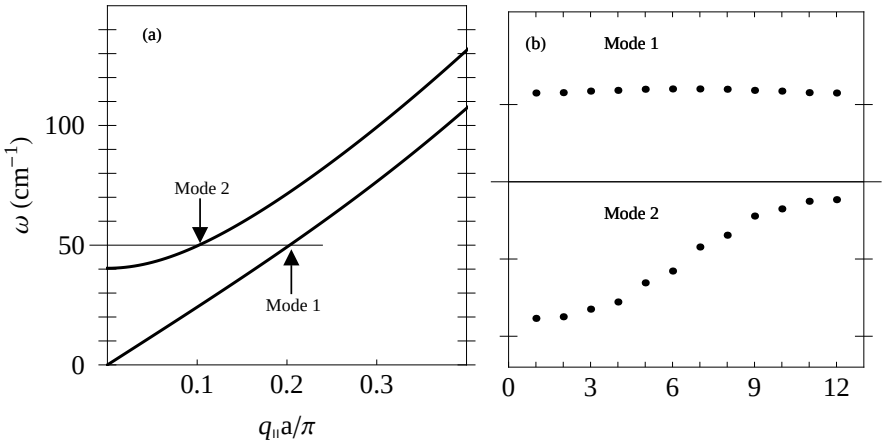

Figure 5.7: Two lowest lying flexural phonon branches of the ZGNR. Fig.(a) shows the phonon dispersion in the low frequency region. Figure (b) shows the polarization profile of atoms in an unit cell calculated at 50 cm^{-1} of the acoustic branch (mode 1) and the twisting branch (mode 2).

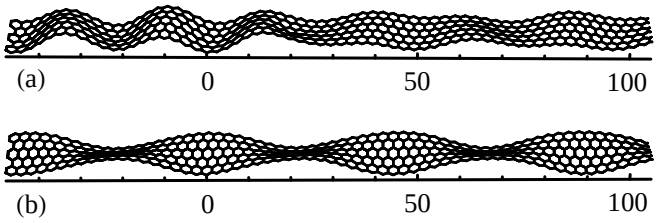

Figure 5.8: Displacement wave in three regions (lead 1, interior region and lead 2) is sketched together when a larger mass is present in the center of the interior region. The left boundary of the interior region (B_1) starts from the origin of the longitudinal coordinate (marked in units of Å) and the right boundary (B_2) is at 20 unit cells away from the B_1 (at 40 Å). The heavy mass is at the 10^{th} unit cell from the B_1 (at 20 Å). The sketch at top (a) is for waves coming in mode 1 at $\omega = 50$ cm^{-1}. The sketch in bottom (b) is for the waves coming in mode 2 at the same frequency.

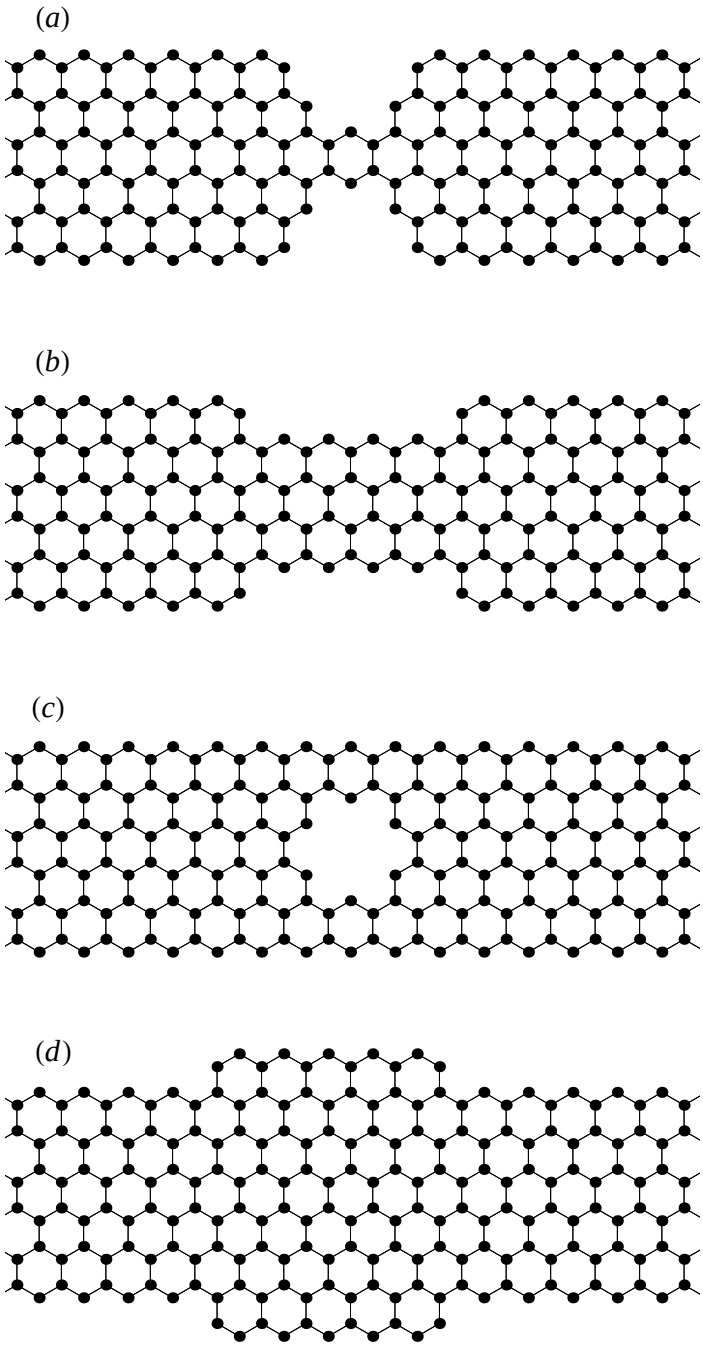

Figure 5.9: Different geometries of the interior region use to study the transmission of flexural vibrational modes.

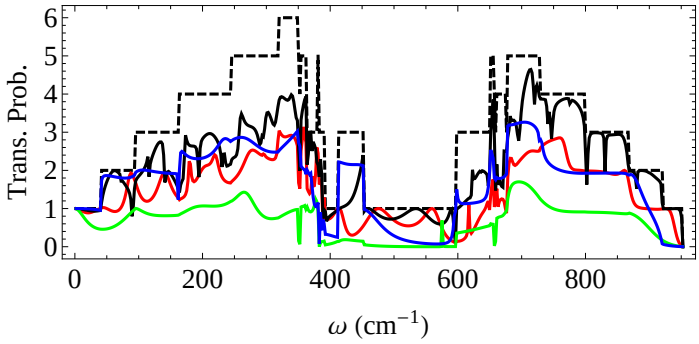

Figure 5.10: Transmission probability for the four structures in fig.5.9. The green line is for the structure "a", red line is for the structure "b", blue line is for the structure "c" and the black line is for the structure "d". The dashed line is for the uniform 6-ZGNR.

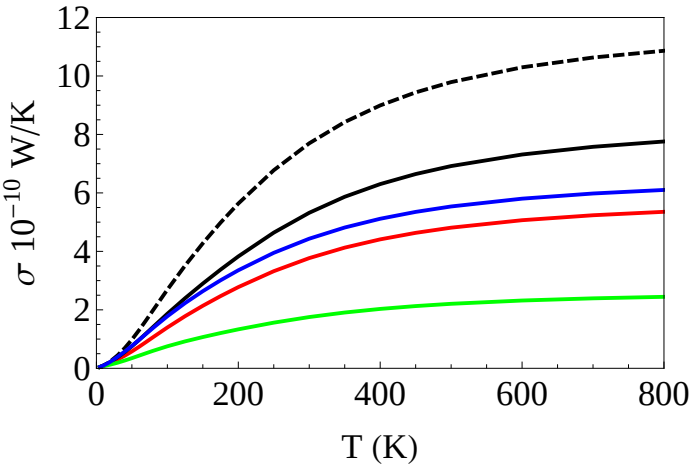

Figure 5.11: Thermal conductance(σ) for the four structures in fig.5.9 as a function of temperature. The green line is for the structure "a", the red line is for the structure "b", the blue line is for the structure "c" and the black line is for the structure "d". The dashed line is for the uniform 6-ZGNR.

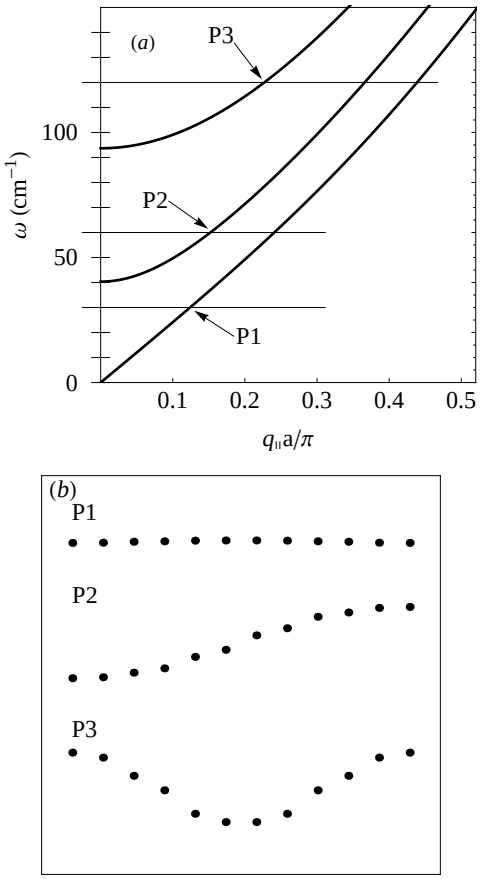

Figure 5.12: Three lowest lying flexural phonon branches of the 6-ZGNR. Fig.(a) shows the phonon dispersion in the low frequency region. Figure (b) shows the polarization profile of atoms in an unit cell calculated at 30 cm^{-1}(mode P1), 60 cm^{-1} (mode P2) and 120 cm^{-1}(mode P3).

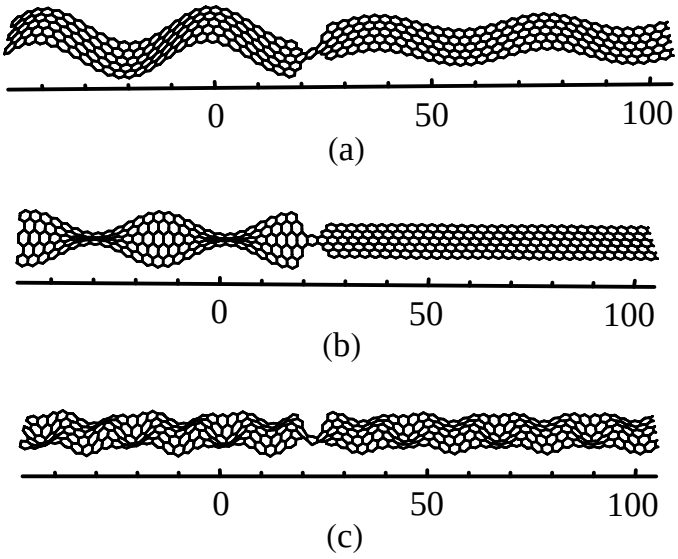

Figure 5.13: Displacement wave in three regions (lead 1, interior region and lead 2) is sketched together for the structure "a". The longitudinal coordinate is marked in units of Å. The sketch (a) is for waves coming in mode P1 at $\omega = 30$ cm^{-1}. The sketch (b) is for the waves coming in mode P2 at $\omega = 60$ cm^{-1}. The sketch (c) is for the waves coming in mode P3 at $\omega = 120$ cm^{-1}.

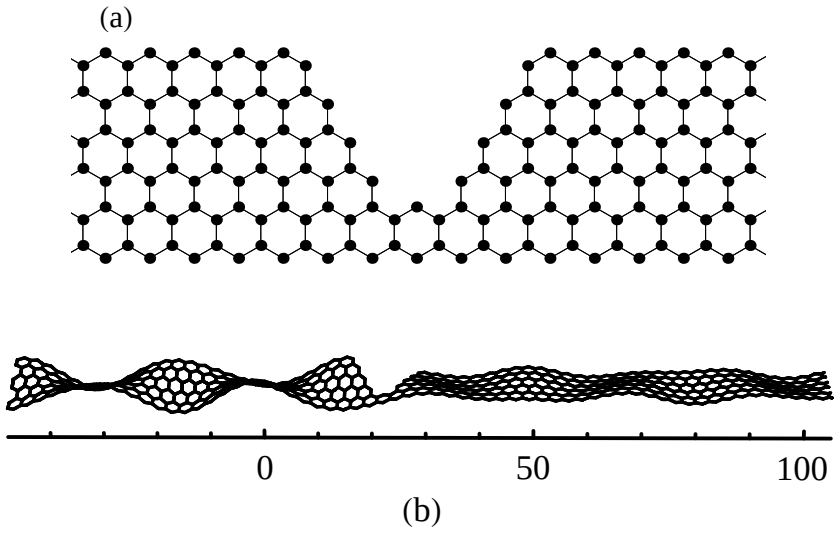

Figure 5.14: (a)Asymmetric structure. (b) Sketch of the scattering of the displacement wave, which is coming in the mode P2 at 60 cm^{-1}.

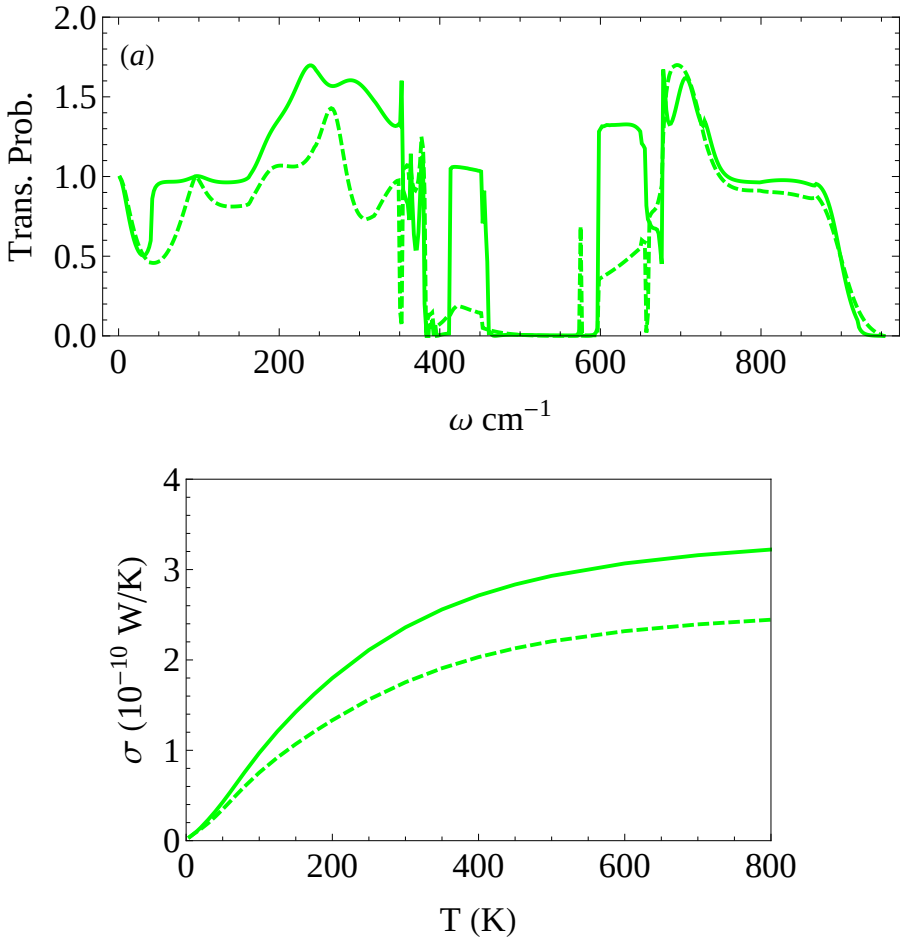

Figure 5.15: (a) Transmission probability for the asymmetric structure (solid green line) and dashed line is for structure "a" (symmetric structure). (b) the thermal conductance as a function of the temperature.

Chapter 6

Thermal Transport in Strained Graphene Nanoribbons

6.1 Introduction

Operation of nanoscale thermal devices mainly relies on the tunability of phonon transport by external means. Thermal devices such as thermal rectifiers[10], thermal transistors[11] and thermal memories[12] are a new class of devices whose operation is driven by the temperature gradients. These devices will have useful applications not only in thermal circuits[13] but also in nanoscale thermal management and thermoelectric applications.

A thermal rectifier, in which the thermal current is larger in one direction than in the opposite, is one of the most fundamental thermal devices to be realized experimentally in nanoscale. Thermal rectification has been demonstrated using molecular dynamics simulations (MD) in asymmetric systems and is discussed as resulting from an interplay between structural asymmetry and lattice anharmonicity [10, 83, 84, 85]. Recently, this phenomenon has been observed experimentally in asymmetrically mass loaded carbon and boron nitride nanotubes [86]. It has also been shown by MD simulations that varying the mass across an atomic chain with the anharmonic interactions can produce a system that rectifies thermal currents [83]. Moreover, thermal rectification has been predicted in triangular and trapezoidal shaped graphene nanoribbons(GNRs)[84, 85]. We introduce a method based on strain engineering as

an experimentally feasible approach to realize thermal rectification in GNRs. The potentially real-time tunability of the thermal rectification is a distinctive advantage of this approach.

Graphene is a promising material for nanoscale applications due to its exceptional electronic [70], thermal [23, 24] and mechanical [71, 72, 73] properties. It has been shown recently that the electronic properties of graphene can be tuned significantly by engineering strain. For instance, strain could produce a pseudo-magnetic field [87, 88, 89] which affects the electronic properties of graphene. Furthermore, strain could induce semiconducting properties on metallic GNRs by opening a gap in the electronic band structure [90]. However, strain induced tuning of thermal transport properties of graphene has been less studied. The effect of uniform uniaxial strains on the thermal conductivity (κ) of graphene has been studied recently by MD simulations and reported the effect is substantial in tuning κ [91, 92, 93].

We carry out MD simulations and phonon dispersion calculations to study the effect of strain on the thermal conductivity of GNRs. We observe that the variation of κ with moderate uniaxial strains (arrows in fig.6.1a) has a strong dependence on the edge chirality. A similar trend has also been reported recently and is attributed to the geometrical anisotropy of graphene [93]. To investigate the behavior, we calculate the phonon dispersions of strained GNRs, which provide a good insight into this anisotropic strain effect. We observe the flattening of phonon modes and the opening of a gap in the phonon dispersion of AGNRs with increasing uniaxial strain, which results in a dramatic reduction of κ. However, the effect on ZGNRs is mild for

moderate tensile strains where the calculated κ shows a weak dependence. We observe thermal rectification on an asymmetrically stressed rectangular AGNR. In our system, asymmetric stress is achieved by exerting a transverse force (F_y) on the top and bottom edge atoms of part (for example, the right half) of the AGNR as illustrated in fig.6.1b. We observe that the thermal current is larger from less stressed region to the more stressed region (left to right) than that in the opposite direction (right to left). The real time tunability of the thermal rectification on F_y is the important finding reported in this chapter.

6.2 Method

Figure 6.1 shows a schematic of the n-ZGNR and n-AGNR structures simulated. The carbon-carbon bond length is 1.42Å in the absence of strain. The index n refers to the number of carbon dimers (a dimer is shown by the oval) across the width [94]. The first and the last columns of atoms are fixed and the adjacent three columns of atoms of the n-ZGNR and four columns of atoms of the n-AGNR are coupled to Nosé -Hoover thermostats [95, 96]. The equations of motions of thermostated atoms are given by equation 6.1.

$$\begin{aligned} \frac{dP_i}{dt} &= F_i - \gamma P_i; \quad \frac{d\gamma}{dt} = \frac{1}{\tau^2}\left(\frac{T(t)}{T_0} - 1\right) \\ F_i &= -\sum_{k,l,j} \frac{\partial V_{kl}}{\partial r_{ij}} \end{aligned} \tag{6.1}$$

where, the subscript i runs over the atoms in either left or right thermostat, P_i is the momentum of the i^{th} atom , F_i is the force acting on the i^{th} atom, V_{kl} is the many-body potential, r_{ij} is the distance between atom i and j, γ and τ are the

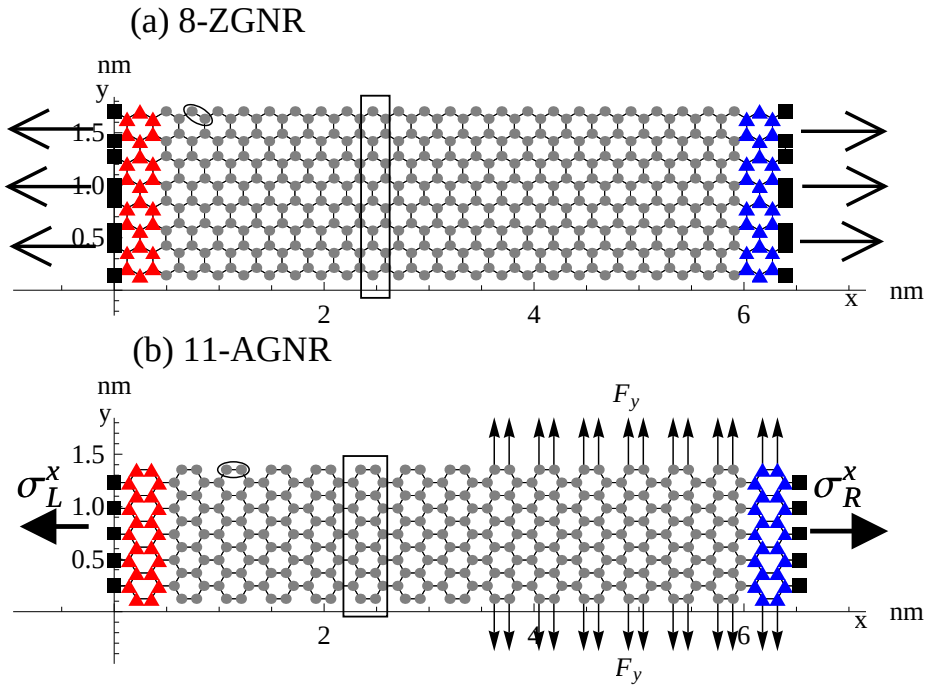

Figure 6.1: Schematic of the 8-ZGNR (a) and 11-AGNR (b). The triangles represent the thermostatted atoms in the left and right heat baths. The full squares are the fixed atoms at both ends. The horizontal arrows in (a) shows the direction of uniaxial tensile strain. In (b) the vertical arrows show the applied constant force F_y on the top and bottom atoms (14 atoms on each side) of the right half of the AGNR. The horizontal arrows in (b) represent the stress developed in length (x) direction (σ^x_R and σ^x_L) near the heat baths. The boxed regions refer to a unit cell of GNRs.

dynamic parameter and the relaxation time of the thermostat, $T(t) = \frac{2}{3Nk_B}\sum_i \frac{P_i^2}{2m}$, is the instantaneous temperature of the thermostat at time t, T_0 is the set temperature of the thermostat, N is the number of atoms in the thermostat, k_B is the Boltzmann constant and m is the mass of the carbon atom. Atoms not in the thermostats move according to standard Newtonian mechanics.

A second generation Brenner potential [81] is employed to describe the carbon-carbon interactions. The equations of motion are integrated using the third-order predictor-corrector method. The time step is 0.5 fs and the total simulation time is 5 ns (10^7 time steps). The temperatures of the left and right heat baths (HBs) are set to T_L and T_R respectively. The temperature difference $(T_L - T_R) = 2\alpha T$, where α determines the temperature bias and the average temperature $T = (T_L + T_R)/2$. The net heat flux (J) was calculated by the power delivered by the heat baths [97]. The heat current injected from either the left(L) or right(R) Nosé-Hoover thermostat (J) is given by $J = \sum_i \frac{(-\gamma P_i)P_i}{m} = -3\gamma N k_B T(t)$. The net heat current at the steady state is $J = (J_L - J_R)/2$. The thermal conductivity (κ) of the system is calculated according to Fourier's law, $J = \kappa w h \frac{(T_L - T_R)}{l}$, where l, w and h are length, width and van der Waals thickness ($h = 0.335$ nm) of the GNR. The length of the GNRs used in this work is $l \approx 6.5$ nm.

The MD code used in this calculation was first developed by Brenner [98] and further modified by Hu et al.[84]. We included some modifications to apply external forces, to strain and to calculate average forces on atoms. Furthermore, we parallalized the code using Open MP directives so that the computational time is greatly

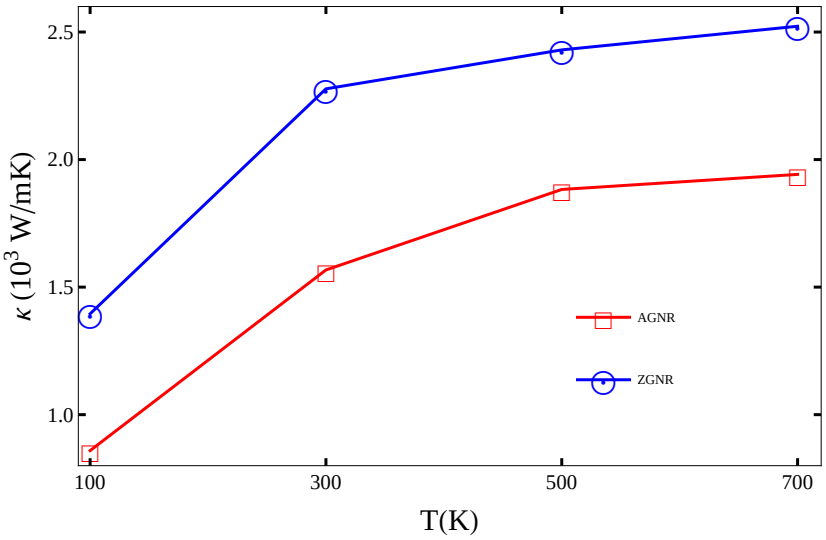

Figure 6.2: Plot of thermal conductivity (κ) of ZGNR (Circle) and AGNR (Square) as a function of temperature.

reduced.

6.3 Graphene nanoribbons under uniaxial strain

First, the thermal conductivities(κ) of both AGNR and ZGNR are calculated in the temperature range 100K -700K (6.2). The calculated unstrained values of κ is in the range of experimentally reported values [23, 24]. The κ of ZGNR is larger than that of AGNR, which is consistent with the previous theoretical findings [84, 99]. At 300K thermal conductivity of AGNR is 1600 W/mK and that of the ZGNR is 2295 W/mK. The κ of both nanoribbons increases as the average temperature increases. Beyond 300K the rate of increase in the thermal conductivity with temperature is dramatically reduced. This could be a result of increased rate of phonon scattering

from the boundaries and other phonons.

Mechanical behavior

We observe that both GNRs buckle along the out of plane direction in our simulation. The AGNR shows a peak height of 0.15 nm at 100 K. As the temperature increases the peak height decreases and at 700 K it reaches 0.005 nm. But the ZGNR has a peak height about 0.03 nm and decreases only weakly with temperature. The experimentally observed peak height is higher than what we observe probably due to the small size of our simulated GNR [76, 77]. By applying tensile/compressive strain flattening/bending of the GNR was observed. The strain is given by $(l-l_0)/l_0$, where l is the stretched or compressed length and l_0 is the initial length of the sample. The positive sign is for tensile strain and the minus sign is for compressive strain. Strain was applied by slowly moving the fixed atoms on one side at a rate of $\pm 1.0 \times 10^{-6}$ nm per time step at the beginning of the simulation. At 300 K compressive strain of 0.03 show about 0.8 nm peak height for both AGNR and ZGNR.

During the simulation the time average of the forces on each atom, $\langle F_j \rangle_t$ for non-thermostatted atoms and $\langle F_i - \gamma P_i \rangle_t$ for thermostatted atoms, is calculated by averaging over the last 10^6 time steps. These time averaged forces are exponentially small except for the atoms at the two edges that are fixed. The externally applied force on the all fixed atoms on one side (holding them in fixed position) is always along the length direction of the GNR. There is an equal and opposite force on the fixed atoms acting on the center part of the nanoribbon. In fact this is the force

developed across the nanoribbon.

Figure 6.3 shows the variation of the stress(σ), force per unit area, with the applied strain on AGNR and ZGNR measured at 300 K. Both nanoribbons shows linear variation of stress with strain. By doing a linear fit we obtain the Young's modulus of AGNR to be 662 GPa and that of ZGNR to be 682 GPa. Similar values have been observed previously [72, 73].

Strain dependence of thermal conductivity

Figure 6.4 shows the variation of κ of ZGNRs and AGNRs of two different widths as a function of strain ranging from -0.03 to 0.12. The horizontal arrows in fig.6.1a show the direction of uniaxial tensile strain on both nanoribbons. The dependence of κ of ZGNRs on tensile strain is relatively weak within the range of studied. The variation of κ for ZGNRs in the range of strain $0 - 0.09$ is less than 10% from the unstrained values. On the other hand, κ of 11-AGNR decreases significantly when increasing the tensile strain. The reduction of κ at a strain of 0.09 is about 45% for 11-AGNR and 55% for 19-AGNR. Thus, κ of AGNR shows excellent sensitivity to the tensile strain making it promising for strain based thermal device applications.

In order to understand the above edge chirality dependence of κ, we calculate the phonon dispersion of unstrained nanoribbons and at strains of 0.015, and 0.062. This is calculated by diagonalizing the dynamical matrix of the system with the force constants evaluated from the Brenner potential. Since the strained structures are optimized at 300 K, the equilibrium positions of atoms are taken to be the average

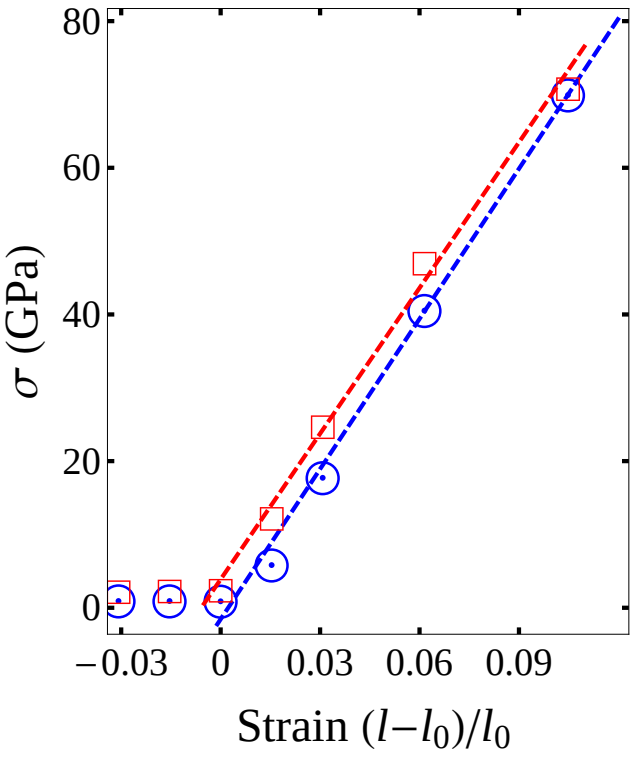

Figure 6.3: Plot of stress (in GPa) as a function of strain for AGNR(Square) and ZGNR (Circle) at room temperature (300 K). The dashed lines are the linear fit to the data of positive strain. From this we extract the Young's modulus of AGNR to be 662 GPa and that of ZGNR to be 682 GPa.

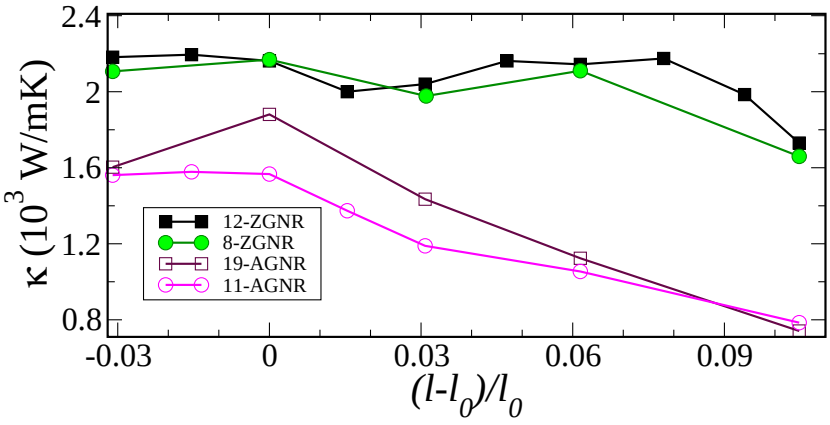

Figure 6.4: Thermal conductivity (κ) as a function of uniaxial strain $(l - l_0)/l_0$ along the transport direction(x) calculated at 300 K.

fluctuation positions of atoms at 300 K. Figure 6.5 shows the phonon dispersions of 12-ZGNR and 11-AGNR along the transport direction(x). These two GNRs have almost the same number of modes in the phonon dispersion because there are almost the same number of atoms in a unit cell (24 and 22). The unit cells of both GNRs are depicted by the boxed region in fig.1. In GNRs of comparable widths, the AGNR has a larger number of modes. However, we observe that the κ of ZGNRs is larger than that of AGNRs. The major difference in the unstrained dispersion curves (fig.6.5a and b) is that the phonon group velocities of ZGNR are much higher than that of AGNR. A similar behavior of the phonon dispersion has been observed in a recent study using first principle calculations [99]. This could be the reason for the observed larger κ in ZGNRs. When increasing the uniaxial tesile strain, we do not observe a significant alteration of dispersion curves of the 12-ZGNR in the low frequency region (fig.6.5 a,c,e). However, in 11-AGNR we observe considerable effects when

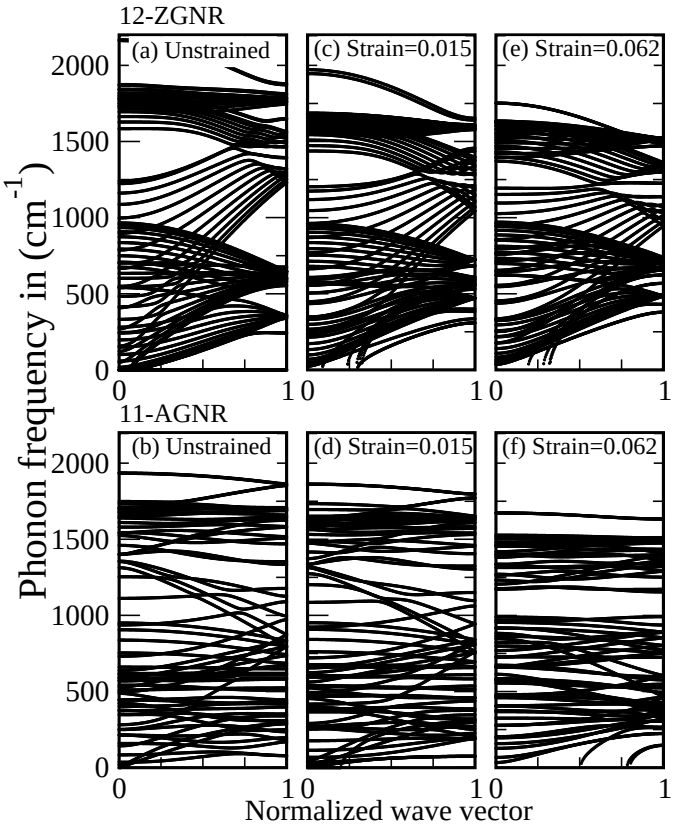

Figure 6.5: Phonon dispersion of 12-ZGNR and 11-AGNR under uniaxial tensile strains. The horizontal axis is the normalized wave vector projected on to the transport direction(x).

increasing strain (fig.6.5 b,d,f). The modes flatten reducing their group velocities. The unique effect is the opening of a gap in the phonon dispersion. At a strain of 0.062, we observe a gap in the frequency range: $1000 - 1200$ cm^{-1} (fig.6.5f). Thus, the above sensitivity of the phonons in AGNRs to the strain could be the reasons for the dramatic reduction of κ with increasing strain.

6.4 Thermal rectification under asymmetric strain

In many of the theoretical studies on thermal transport, the stress along the nanoribbon is considered to be uniform and uniaxial. There is no difference in thermal currents when switching the sign of the temperature bias (α), since the system is symmetric. We consider a situation that the stress at the left and right edges of the nanoribbon are σ_L and σ_R such that $\sigma_L \neq \sigma_R$. In the intermediate region it is assumed to vary smoothly. This kind of stress profile could possibly be realized experimentally using the differential thermal expansion of graphene grown on structured substrates [89, 77, 78] or through externally applied strain [100, 101]. We achieve such an asymmetric stress profile in our simulation by transversely stressing a half of the GNR. For example, we apply a constant force F_y on the atoms of the top and bottom edges of the right half of the 11- AGNR as depicted in fig.6.1b. The tensile stress developed across the y direction of the right half is denoted by σ_R^y. This lateral stress produces a tensile strain along the y direction and, hence a compressive strain along the x-direction due to the Poisson contraction. Since the atoms in the left and right edges are fixed, this compressive strain also results in tensile stress in the x-direction. The stress in the x-direction near the left and right HB is denoted by σ_L^x and σ_R^x. This is calculated from the time average of the forces on the fixed atoms at the left and right edges(excluding the corner atoms). Figure 6.6a shows the variation of σ_L^x and σ_R^x on F_y calculated at $T = 300$ K. The σ_L^x and σ_R^x are tensile, and σ_L^x is smaller than the σ_R^x while both are found to be increasing with F_y.

In fig.6.6b, the thermal current from left to right ($+\alpha$) and right to left ($-\alpha$) are

plotted against the applied force F_y, when $|\alpha| = 0.3$ and $T = 300$ K. The thermal current from left to right ($J_{L\to R}$) shows very small decrement, where as the $J_{R\to L}$ decreases significantly when F_y is increased. Thus, the $J_{L\to R}$ is considerably larger than $J_{R\to L}$ whenever $F_y > 0$, marking the existence of thermal rectification in this system.

The tensile stress and strain can affect the thermal transport by distorting the lattice to both alter the characteristic vibrational frequencies and the degree of anharmonicity.[102] Anharmonicity is essential: *no amount of geometric or parameter asymmetry can produce thermal rectification.* Without anharmonicity, the system can be analyzed via normal modes, and time reversal symmetry will require that transmission amplitudes from left to right are the same as right to left. We attribute the observed thermal rectification to the strain induced asymmetry of the vibrational frequencies and the lattice anharmonicity. Such an asymmetry of the vibrational properties leads to a local variation of κ. It can be shown that the thermal conductivity must be a function of both position and temperature to rectify the thermal current.[103]

We can invoke the framework of non-equilibrium thermodynamics to describe this effect. The change of the entropy per unit volume of a solid due to the applied stress (τ_α) can be expressed[104], $ds = \frac{du}{T} - \frac{1}{T}\sum_\alpha \tau_\alpha d\eta_\alpha$, where du is the change of internal energy density, η_α is the strain and $\alpha \in [xx, yy, xy]$. From this we can deduce the rate of production of entropy[105],

$$\dot{s} = \partial_i \left(\frac{1}{T}\right) J_i^{(u)} + \frac{1}{T}\partial_i \left(\tau_\alpha\right) J_i^{(\eta_\alpha)} \tag{6.2}$$

where $J_i^{(u)}$ and $J^{(\eta_\alpha)}$ are the i-th components of the energy and the strain currents, and repeated indices are summed over. In general the currents are a function of the intensive parameters (T and τ) as well as the affinities[105] ($\nabla\frac{1}{T}$ and $\nabla\tau$). Thus the heat current, $\vec{J}^{(Q)}$, can be expanded in its most general form:

$$J_i^{(Q)} = L_{i,j}^{(Q)}\,\partial_j\frac{1}{T} + \frac{L_{i,j}^{(\eta_\alpha)}}{T}\,\partial_j\tau_\alpha + L_{i,j,k}^{(QQ)}\,\partial_j\frac{1}{T}\partial_k\frac{1}{T} + \frac{L_{i,j,k}^{(Q\eta_\alpha)}}{T}\partial_j\frac{1}{T}\partial_k\tau_\alpha + \frac{L_{i,j,k}^{(\eta_\alpha\eta_\beta)}}{T^2}\partial_j\tau_\alpha\partial_k\tau_\beta \tag{6.3}$$

In solids, barring plastic deformation, there is no heat current in steady state solely due to $\nabla\tau_i$. Thus, the coefficients $L^{(\eta_\alpha)} = L^{(\eta_\alpha\eta_\beta)} = 0$. Moreover, in symmetric systems there is no thermal rectification, which implies $L^{(QQ)} = 0$. If we further assume only gradients in the x-direction and stress in the y-direction the above equation can be reduced to,

$$J_x^{(Q)} = L_{x,x}^{(Q)}\partial_x\frac{1}{T} + \frac{L_{x,x,x}^{(Q\eta_{yy})}}{T}\partial_x\frac{1}{T}\partial_x\tau_{yy}, \tag{6.4}$$

which leads to different thermal currents when switching the sign of the stress gradient ($\nabla\tau$). For the case of $F_y = 4.8$ nN, the calculated kinetic coefficients are $L_{x,x}^{(Q)} = 1.7\times10^8$ WK/m and $L_{x,x,x}^{(Q\eta_{yy})} = 0.34$ WK^2/GPa.

The distinctive property of this approach is the tunability of the thermal rectification by an asymmetrically applied force, F_y. We show in fig.6.6c the thermal rectification factor (TR) as a function of F_y calculated at $T = 300$ K. The TR is defined as, $TR = 2\frac{(J_{L\to R}-J_{R\to L})}{(J_{L\to R}+J_{R\to L})}\times100\%$. We observe an increment of the TR when increasing the F_y. The increment of TR with F_y is more prominent at higher biases ($\alpha = 0.3$). As shown in the fig.6.6d, the $J_{L\to R}$ increases almost linearly with the bias

(α), whereas $J_{R\to L}$ increases nonlinearly giving rise to a larger TR. This behavior suggests the contribution of higher order terms (beyond the second order) to eq.6.3. The nonlinear transport is an essential property in realizing thermal rectification as in an electronic diode. In our system the nonlinear transport is prominent at larger F_y's (> 0.8 nN), where we observe a clear bias dependence of TR. The maximum TR we observed is about 73% which occurred at $\alpha = 0.3$ and $F_y = 5.6$ nN.

The right side of the AGNR is subjected to a biaxial stress whereas the left side only has an uniaxial stress. It is evident that the asymmetry of the on axis stresses (σ_R^x and σ_L^x) is important in determining the TR. We achieve a significant TR whenever the ratio $\sigma_R^x/\sigma_L^x \gtrsim 2.0$ (see fig.6.6e). When we move the laterally stressed window towards the center, the TR reduced considerably in our simulation. This is a reasonable observation, because the asymmetry of the system is reduced. For instance, when we move the laterally stressed window eight columns towards the center (keeping the number of atoms that F_y is applied constant) the TR decrease to 5% at $\alpha = 0.3$ and $F_y = 4.8$ nN. In this situation, the ratio of stresses reduces to 1.5 which is close to the ratio at $F_y = 0.8$ nN where the observed TR is about 6%. By increasing the length of the AGNR and hence the number of atoms that F_y is applied, we could increase the above ratio and observe a larger TR.

Graphene commonly possesses edge disorder which significantly degrades its thermal properties. In fig.6.6c the open circles shows the variation of TR in the presence of edge disorder. Since the simulated AGNRs are very small, we introduce only about a 4%(percentage of number of edge atoms removed) edge disorder. We observe mod-

erate reduction of TR, down to a value $\sim 30\%$. The effect of edge disorder can be reduced by increasing the width of the nanoribbon. However, the presence of vacancy defects significantly reduces the TR. The open triangles in fig.6.6c is for 0.6% vacancy defects distributed evenly in the nanoribbon.

Experimentally, the lateral force on the right half of the AGNR can be applied by coupling to a substrate. Our simulation fixed the atoms to which the forces were applied. This situation also produces larger thermal rectification(over 100%) at higher biases and the direction of the maximum thermal current is same as before. This effect can be understood by the simple argument in ref.[103]. Consequently the observable net thermal rectification could be even higher due to the asymmetric coupling between the GNR and the substrate.

Electronic transport of heat will occur in parallel to the phonon conduction, but is not so large that it dwarfs the phonon channel considered here. In addition, AGNRs shows semiconducting characteristics and their energy gap can be tuned with the strain[90]. Thus, the electronic contribution to the thermal transport should not be crucial.

Electron-phonon interactions could lead to processes that undermine the thermal rectification. We believe that their contribution to the thermal rectification is also minimal since the nanoribbon is semiconducting. In addition, the long electronic coherence length in graphene indicates that electron-phonon interactions should not be significant. In experiments, these effects can be further minimized by electronically gating the sample.

Finally, we discuss the stability of the C-C bonds in graphene under the lateral forces. We do not observe any rupture of bonds within the applied range of F_y ($0-5.6$ nN). Using an atomic force microscope, the force required to break a C-Si bond has been measured to be approximately 2.0 nN [106]. The covalent bonds in graphene are believed to be much stronger. In our simulation the estimated maximum force in the C-C bond direction is about 6.4 nN, which corresponds to a lateral stress of $\sigma_R^y = 90$ Gpa. In a recent experiment, it has been found that the intrinsic strength of a single layer graphene is about 130 GPa assuming the van der Waals thickness of graphene [71]. When the F_y is increased to 7.2 nN, we observe rupturing of some bonds near the fixed atoms in the right side of the AGNR. At this point, the maximum force in the C-C bond direction is about 8.0 nN. Thus, the forces required to realize thermal rectification by our method, are realistic and in an experimentally feasible range.

6.5 Conclusion

In conclusion, we study the thermal transport properties of strained GNRs using MD simulations. We observe that the thermal conductivity of AGNRs decreases significantly by applying an uniform uniaxial tensile strain while that of ZGNR has a weak dependence on moderate tensile strains. These results show a good agreement with the calculated phonon dispersions of strained GNRs. In AGNRs, we observe the flattening of phonon modes and the opening of a gap in the phonon dispersion which leads to the dramatic reduction of κ with tensile strains. On the other hand, the phonon dispersion of ZGNRs shows only small alterations which results in a weak

dependence of κ with moderate tensile strains. Thus, AGNRs are promising for strain induced thermal device applications. Furthermore, we demonstrate that the thermal rectification can be realized by engineering the stress on a rectangular AGNR. We have found that the heat transport is favorable from the less stressed region to the more stressed region. The major advantage of this approach is that the thermal rectification can be tuned from no rectification state to over 70% in real-time by applying a mechanical force.

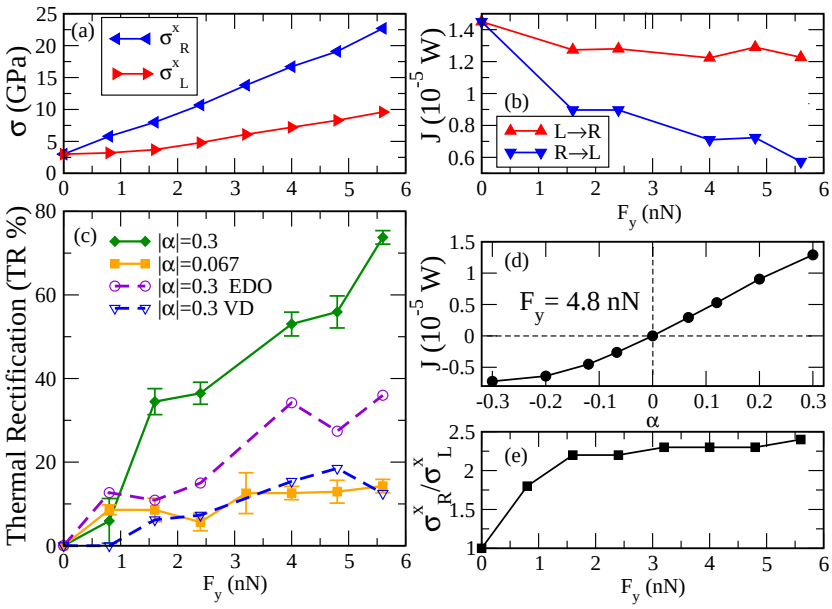

Figure 6.6: (a) Variation of stress (σ_R^x and σ_L^x) on the 11-AGNR, (b) thermal current from left to right and right to left at $T = 300$ K and $|\alpha| = 0.3$, and (c) thermal rectification factor(TR) at $T = 300$ K as a function of F_y. The open circles are in the presence of edge disorder(EDO) and the open triangles are in the presence of vacancy defects(VD). (d) Variation of thermal current with the temperature bias (α) at $F_y = 4.8$ nN. (e)The ratio σ_R^x/σ_L^x as a function of F_y. The units of F_y is nano Newton (nN).

Chapter 7

Conclusions and Future Work

In this thesis, I developed two theoretical tools to study coherent thermal transport on the nanoscale. I believe these tools will be useful in studying real world problems as I discuss by simple examples.

In chapter 2, I discussed an approach to include the interface coupling in the continuum model, where we use continuous functions to handle the interface. We use this approach to optimize the interface thermal transport between hard and soft materials. We include an interface variation of materials to maximize the thermal transport and the optimal variation of mass density and elasticity is obtained numerically in the continuum limit. CNT and graphene sheets can be functionalized with molecules that lead to significantly change the transport properties. The developed continuum calculation can be used to study the coherent thermal transport from functionalized molecules to the CNT or graphene sheets. In this context, it is important to identify the possible side chains that can be attached to graphene sheets. This is still an open question.

In chapters 3 and 4, I developed R-matrix theory to calculate phonon scattering on the atomic scale. In this approach, we can include all the details in the atomic scale within the harmonic approximation to calculate phonon transmission. This approach is a computationally efficient approach as compared with the non-equilibrium green's function approach(NEGF). The harmonic limit calculation misses of the non-linear

effects of the interaction potential. However, the harmonic approximation is sufficient to study the effect of boundaries, interfaces and impurities which are the dominant scattering mechanisms on the nanoscale. The major drawback of the R-matrix formalism is the inability to include non-linear interactions. In principle the non-linear interactions and electron-phonon interactions can be included in the Green's function calculations. In this case the NEGF approach can be used despite of its high computational cost. The R-matrix approach is a mode to mode transmission calculation technique. In chapter 5 I demonstrated how the R-matrix approach is used to analysis the mode specific transmission of graphene nanoribbons.

The computational efficiency of RMT has proven its potential in studying atomic scale thermal transport. Thus, the RMT enabled studying thermal transport in relatively larger systems than the other available techniques can reach. The RMT can be used in calculating thermal transport in structured systems and interfaces. It is important to study the interface thermal transport between CNT/graphene and silicon. Theses carbon nano-materials have the potential to efficiently remove the heat from the heating elements. An interface transition layer (molecules that link the CNT/graphene to silicon surface) can be incorporated to maximize the interfacial thermal transport. It is important to identify a suitable material to treat the CNT-silicon (or graphene-silicon) interface. Furthermore, RMT can be used to study the thermal transport in CNT/polymer or graphene/polymer composites materials. In this context, it is important to study the thermal transport between dispersed CNT or graphene flakes through molecular side chains.

In chapter 6, I used molecular dynamics simulation (MD) to study the thermal transport in strained graphene nanoribbons. MD has the advantage of easily incorporating the full inter-atomic potential. Thus, MD is an essential and widely using tool to study the thermal transport in nanoscale.

Using molecular dynamics(MD) simulations and phonon dispersion calculations, I found that the thermal conductivity of zigzag graphene nanoribbons (GNRs) shows a weak dependence on moderate tensile strains, while that of armchair GNRs decreases significantly, a feature that could be promising for strain induced thermal device applications. I observe significant thermal rectification (over 70%) in a rectangular armchair GNR by applying a transverse force asymmetrically. The heat flux is larger from the less stressed region to the more stressed region. Furthermore, I develop a theoretical framework based on the non-equilibrium thermodynamics to discuss when thermal rectification under a stress gradient can occur.

Furthermore, it is important to study the consequences of disorder and the defects that lead to reduce the thermal rectification factor. I studied the effect of edge disorder and the vacancy defects on thermal rectification. It is found that edge disorder only partially reduces the thermal rectification while effect of the vacancy defects is significant. According to the Wiedemann Franz law, the electronic contribution to thermal transport in graphene is about 30% at room temperature in unstrained graphene. However it is not large enough to dwarf the phonon channel considered here. In strained systems electrons scatter due to the deformation of the lattice and increase the resistivity considerably reducing the electronic contribution to the

transport. This will also influence the transport of phonons. Thus, as a future work, it is important to study the electron phonon interaction of these strained systems.

References

[1] J. I. Sohn, C. Nam, and S. Lee, Applied Surface Science **197**, 568 (2002).

[2] D. Li, Y. Wu, P. Kim, L. Shi, P. Yang, and A. Majumdar, Appl. Phys. Lett. **83**, 2934 (2003).

[3] W. Fon, K.C.Schwab, J. Worlock, and M.L.Roukes, Phys. Rev. B **66**, 045302 (2002).

[4] S. Barman and G. Srivastava, Phys. Rev. B **73**, 205308 (2006).

[5] C. Guthy, C. Nam, and J. E. Fischer, J. Appl. Phys. **103**, 064319 (2008).

[6] G. Pernot, M. Stoffel, I. Savic, F.Pezzoli, P. Chen, and et al., nature materials **9**, 491 (2010).

[7] A. Balandin and K. L. Wang, J. Appl. Phys. **84**, 6149 (1998).

[8] H. Sevincil and G. Cuniberti, Phys. Rev. B **81**, 113401 (2010).

[9] W. S. Bao, S. Y. Liu, and X. L. Lei, J. Phys.: Condens. Matter **22**, 315502 (2010).

[10] M. Terraneo and *et al.*, Phys.Rev.Lett. **88**, 094302 (2002).

[11] B. Li and *et al.*, Appl.Phys.Lett. **88**, 143501 (2006).

[12] L. Wang and *et al.*, Phys.Rev.Lett. **101**, 267203 (2008).

[13] L. Wang and B. Li, Physics World **21**, 27 (2008).

[14] L. Lin and D. Chung, Journal of Electronic Materials **23**, 6 (1994).

[15] M. Biercuk, M. Llahuno, M. Radosavljevic, J. Hyun, and A.T.Jonson, Appl.Phys.Lett. **80**, 2767 (2002).

[16] K.C.Yung and H. Liem, j.appl.Polymer science **106**, 3587 (2007).

[17] D. G. Cahill, W. K. Ford, K. E. Goodson, G. D. Mahan, A. Majumdar, H. J. Maris, R. Merlin, and S. R. Phillpot, J. Appl. Phys. **93**, 793 (2003).

[18] `http://en.wikipedia.org/wiki/Joseph_Fourier`.

[19] `http://en.wikipedia.org/wiki/Polyethylene_terephthalate`.

[20] `http://en.wikipedia.org/wiki/Thermal_conductivity`.

[21] S. Berber, Y.-K. Kwon, and D. Tomnek, Phys.Rev.Lettl **84**, 4613 (2000).

[22] J. Hone, Dekker Encyclopedia of Nanoscience and Nanotechnology 603 (2004).

[23] A. A. Balandin, S. Ghosh, W. Bao, I. Calizo, D. Teweldebrhan, F. Miao, and C. N. Lau, Nano.Lett. **8**, 902 (2008).

[24] W. Cai, A. L. Moore, Y. Zhu, X. Li, S. Chen, L. Shi, and R. S. Ruoff, Nano. Lett. **10**, 1645 (2010).

[25] C. Kittel, *Introduction to Solid State Physics*, 8 ed. (John Wiley Sons, New York, 2005).

[26] T. M. Tritt, *ThermalConductivity: theory, properties and applications* (Plenum Publishers, New York, 2004).

[27] M. Kardar, *Statistical Physics of Particles* (Cambridge University Press, Cambridge, 2007).

[28] J.M.Ziman, *principles of the theory of solids*, 2nd ed. (Cambridge University Press, Cambridge, 1972).

[29] J. Vandersande and C. Wood, Contemp. Phys. **27**, 117 (1986).

[30] Y.Han, Phys. Rev. B **54**, 8977 (1996).

[31] A. B. Fowler, A. Hartstein, and R. A. Webb, Phys. Rev. Lett. **48**, 196 (1982).

[32] F. M. Peeters, Phys. Rev. Lett. **61**, 589 (1988).

[33] B. J. van Wees, H. van Houten, C. W. J. Beenakker, J. G. Williamson, L. P. Kouwenhoven, D. van der Marel, and C. T. Foxon, Phys. Rev. Lett. **60**, 848 (1988).

[34] U. Meirav, M. A. Kastner, and S. J. Wind, Phys. Rev. Lett. **65**, 771 (1990).

[35] J. Seyler and M. Wybourne, Phys. Rev. Lett. **69**, 1427 (1992).

[36] R. Landauer, IBM J. Res. Dev. **1**, 223 (1957).

[37] D.A.Wharam, T.J.Thornton, R. Newbury, M. Pepper, H.Ahmed, and et al., J. Phys. C: Solid State Phys. **21**, 209 (1988).

[38] L. G. C. Rego and G. Kirczenow, Phys. Rev. Lett. **81**, 232 (1988).

[39] P.L.Kapitza, Zh.Eksp. Teor.Fiz. **11**, 1 (1941).

[40] P.L.Kapitza, Sov.J.Phys. JETP **4**, 121 (1941).

[41] E. Swartz and R. Pohl, Rev. Mod. Phys. **61**, 605 (1989).

[42] S.Shenogin, L. Xue, R. Ozisik, P. Keblinski, and D. Cahill, J. App. Phys. **95**, 8136 (2004).

[43] B.G.Demczyk, Y.M.Wang, J. Cumings, M. Hetman, W. Han, A. Zetti, and R. Ritchie, Materials science and engineering A **334**, 173 (2002).

[44] L. Kin-tak, Chemical physics letters **370**, 399 (2003).

[45] T.C.Clancy and S. Thomas, Polymer **47**, 5990 (2006).

[46] Y. Kosevich, Phys.rev.B **52**, 2 (1995).

[47] M. P. Blencowe, Phys. Rev.B **59**, 4992 (1999).

[48] D.E.Angelescu, M. Cross, and M. Roukes, Superlattices and Microstructures **23**, 3 (1998).

[49] M.P.Blencowe, Phys.Rep. **395**, 159 (2004).

[50] S. J, J. Wang, and J. Lu, Eur. Phys. J. B **62**, 381 (2008).

[51] K.F.Graff, *Wave Motion in Elastic Solids* (Ohio State University Press, Columbus, 1975), p. 17.

[52] D. Zwillinger, *Handbook of differential equations*, 3 ed. (Academic press, USA, 1989), p. 17.

[53] G. Eason, Bulletin of the seismological society of America **57**, 1267 (1967).

[54] C. Bender and S.A.Orszag, *Advanced mathematical methods for scientists and engineers I* (Springer, New York, 1999).

[55] E.P.Wigner and I. Eisenbud, Phys. Rev. **72**, 12 (1947).

[56] P. G. Burke, A. Hibbert, and W. D. Robb, J. Phys. B **4**, 153 (1971).

[57] B. I. Schneider and P. J. Hay, Phys. Rev. B **13**, 2049 (1976).

[58] L. Smrcka, Superlattices Microstruct. **8**, 221 (1990).

[59] U. Wulf, J. Kucera, P. N. Racec, and E. Sigmund, Phys. Rev. B **58**, 16209 (1998).

[60] T. Jayasekera, K. Mullen, and M. A. Morrison, Phys. Rev. B **74**, 235308 (2006).

[61] K. Varga, Phys. Rev. B **80**, 085102 (2009).

[62] M. Buttiker, Phys. Rev. Lett. **57**, 1761 (1986).

[63] N. Ashcroft and N. Mermin, *Solid State Physics* (Thomson Asia Pte Ltd., Singapore, 2003), p. 439.

[64] N. Mingo and L. Yang, Phys. Rev. B **68**, 245406 (2003).

[65] W. Zhang, T. S. Fisher, and N. Mingo, Numer. Heat Transfer,Part B **51**, 333 (2007).

[66] J. S. Wang, J. Wang, and N. Zeng, Phys. Rev. B **74**, 33408 (2006).

[67] P. Hopkins, P. Norris, M. Tsegaye, and A. Ghosh, Jour. App. Phys. **106**, 63503 (2009).

[68] K. S. Novoselov, A. K. Geim, S. V. Morozov, D. Jiang, Y. Zhang, S. V. Dubonos, I. V. Grigorieva, and A. A. Firsov, Science **306**, 666 (2004).

[69] P.R.Wallace, Phys.Rev. **71**, 622 (1947).

[70] K. S. Novoselov and A. K. Geim, Nature Materials **6**, 183 (2007).

[71] C. Lee, X. Wei1, J. W. Kysar, and J. Hone, Science **321**, 385 (2008).

[72] C. D. Reddy, S. Rajendran, and K. M. Liew, Nanotechnology **17**, 864 (2006).

[73] M. Arroyo and T. Belytschko, Phys.Rev. B **69**, 115415 (2004).

[74] A. H. C. Neto, F. Guinea, N. M. R. Peres, K. S. Novoselov, and A. K. Geim, Rev. Mod. Phys. **81**, 109 (2009).

[75] J.C.Mayer, A.K.Geim, M.I.Karsnelson, K.S.Novoselov, T.J.Booth, and S.Roth, Nature **446**, 60 (2007).

[76] A. Fasolino, J. Los, and M.I.Katsnelson, Nature materials **6**, 12 (2007).

[77] W. Bao, F. Miao, Z. Chen, H. Zhang, W. Jang, C. Dames, and C. N. Lau, Nature Nanotechnology **4**, 562 (2009).

[78] C. C. Chen, W. Z. Bao, J. Theiss, C. Dames, C. N. Lau, and S. B. Cronin, Nano Lett. **9**, 4172 (2009).

[79] N. Mounet and N. Marzari, Phys.Rev. B **71**, 205214 (2005).

[80] J. H. Seol, I. Jo, A. L. Moore, L. Lindsay, Z. H. Aitken, M. T. Pettes, X. Li, Z. Yao, R. Huang, D. Broido, N. Mingo, R. S. Ruoff, and L. Shi, Science **9**, 328 (2010).

[81] D. W. Brenner, Phys.Rev. B **42**, 9458 (1990).

[82] K.G.S.H.Gunawardana and K. Mullen, Numerical Heat Transfer,Part B: Fundamentals **60**, 1 (2011).

[83] N. Yang, N. Li, L. Wang, , and B. Li, Phy.Rev.B **76**, 020301 (2007).

[84] J. Hu, X. Ruan, and Y. P. Chen, Nano Lett. **9**, 2730 (2009).

[85] N. Yang, G. Zhang, and B. Li, Appl.Phys.Lett. **95**, 033107 (2009).

[86] C. W. Chang, D. Okawa, A. Majumdar, and A.Zettl, Science **314**, 1121 (2006).

[87] F. Guinea, A. K. Geim, M. I. Katsnelson, and K. S. Novoselov, Phys. Rev. B **81**, 035408 (2010).

[88] T. Low and F. Guinea, Nano Lett. **10**, 3551 (2010).

[89] N. Levy, S. A. Burke, K. L. Meaker, M. Panlasigui, A. Zettl, F. Guinea, A. H. C. Neto, and M. F. Crommie, Science **329**, 5991 (2010).

[90] G. Gui, J. Li, and J. Zhong, Phys. Rev. B **78**, 075435 (2008).

[91] Z. Guo, D. Zhang, and X. G. Gong, Appl. Phys. Lett. **95**, 163103 (2009).

[92] X. Li, K. Maute, M. Dunn, and R. Yang, Phy. Rev. B **81**, 245318 (2010).

[93] N. Wei, H. Q. Wang, and J. C. Zheng, Nanotechnology **22**, 105705 (2011).

[94] R. Gillen, M. Mohr, J. Maultzsch, and C. Thomsen, Phys.Status Solidi B **246**, 2577 (2009).

[95] S. J. Nosé, Chem.Phys. **81**, 511 (1984).

[96] W. G. Hoover, Phys.Rev. A **31**, 1695 (1985).

[97] G. Wu and B. Li, Phys.Rev. B **76**, 085424 (2007).

[98] `http://www.eng.fsu.edu/~dommelen/research/nano/brenner/`.

[99] Z. W. Tan, J. S. Wang, and C. K. Gan, Nano Lett. **11**, 214 (2011).

[100] T. M. G. Mohiuddin, A. Lombardo, R. R. Nair, A. Bonetti, G. Savini, R. Jalil, N. Bonini, D. M. Basko, C. Galiotis, N. Marzari, K. S. Novoselov, A. K. Geim, and A. C. Ferrari, Phys.Rev. B **79**, 205433 (2009).

[101] M. Huang, H. Yan, C. Chen, D. Song, T. F. Heinz, and J. Hone, J. Proc. Natl. Acad. Sci. U.S.A. **106**, 7504 (2009).

[102] R. C. Picu, T. Borca-Tasciuc, and M. C. Pavel, J. Appl. Phys. **93**, 3535 (2003).

[103] D. Go and M. Sen, J. Heat Transfer **132**, 124502 (2010).

[104] D. Wallace, *Thermodynamics of Crystals* (John Wiley Sons, New York, 1972), p. 17.

[105] H.B.Callen, *Thermodynamics and an introduction to thermostatistics*, 2nd ed. (John Wiley Sons, New York, 1985), p. 307.

[106] M. Grandbois, M. Beyer, M. Rief, H. Clausen-Schaumann, and H. E. Gaub, science **283**, 1727 (1999).